2013

GROUND-BASED AND SATELLITE REMOTE SENSING OF PAROXYSMAL ERUPTIONS AT ETNA VOLCANO, 2011-2012.

Estelle Bonny
Michigan Technological University

GROUND-BASED AND SATELLITE REMOTE SENSING OF PAROXYSMAL ERUPTIONS AT ETNA VOLCANO, 2011-2012.

By

Estelle Bonny

A THESIS

Submitted in partial fulfillment of the requirements for the degree of

MASTER OF SCIENCE

In Geology

MICHIGAN TECHNOLOGICAL UNIVERSITY

2013

This thesis has been approved in partial fulfillment of the requirements for the Degree of MASTER OF SCIENCE in Geology

Department of Geological/Mining Engineering and Sciences

Thesis Advisor: *Simon A Carn*

Committee Member: *Franck Donnadieu*

Committee Member: *Louisa J Kramer*

Department Chair: *Dr. John Gierke*

Table of Contents

List of figures

List of tables

Acknowledgements

First I would like to thank my supervisors during this research project: Simon Carn at MTU in Houghton, Michigan, and Franck Donnadieu and Lucia Gurioli at LMV in Clermont-Ferrand. I also want to thank Louisa Kramer for her helpful comments for the writing of this thesis. This year in the United States of America at MTU, and this project, were facilitated by the INVOGE program. Thank you Benjamin Van Wyk de Vries for making it possible. I am really thankful to be part of this International Master that gave me the opportunity to experience the research from the French and American way.

ESF-MemoVolc is acknowledged for funding a two week visit at the INGV-Catania in Sicily between 24 April and 6 May 2012. Mauro Coltelli and Simona Scollo (INGV-Catania) are thanked for providing access to INGV datasets and helpful discussions. To Rosanna Corsaro, Daniele Andronico, Michele Prestifilippo and everyone I met at Istituto Nazionale de Geofisia e Vulcanologia: “grazie a tutti”. Mount Etna volcano offered me to experience, for the first time, an eruption and lava fountains, where I also discovered the beautiful city of Catania and really good food.

Those last 2 years were really rewarding and taught me many things, and not only academically. Therefore, I want to thank my friends from the M1 and especially Lucie P, Béné, Julie, Virginie, ptite Ju for their support. And many more great people from many different countries that I met in Houghton/Hancock, such as Valeria, Lucie K, Lorenzo, Sarah, Christine, Kelly, Yeliz, Diego, Riccardo, Verity, Mayra, Vienna (the best roommate!), Lauren, Patty, Fede and many others. Finally, I can’t forget all my family: Papa, Maman, mes soeurs Marion et Julia et toutes leurs petites familles, et bien sûr je garde la meilleure pour la fin, ma jumelle VIOLAINE ☺

Finally, thanks Houghton for the best Winter and worst Spring!

Abstract

Mt Etna's activity has increased during the last decade with a tendency towards more explosive eruptions that produce paroxysmal lava fountains. From January 2011 to April 2012, 25 lava fountaining episodes took place at Etna's New South-East Crater (NSEC). Improved understanding of the mechanism driving these explosive basaltic eruptions is needed to reduce volcanic hazards. This type of activity produces high sulfur dioxide (SO_2) emissions, associated with lava flows and ash fall-out, but to date the SO_2 emissions associated with Etna's lava fountains have been poorly constrained. The Ultraviolet (UV) Ozone Monitoring Instrument (OMI) on NASA's Aura satellite and the Atmospheric Infrared Sounder (AIRS) on Aqua were used to measure the SO_2 loadings. Ground-based data from the Observatoire de Physique du Globe de Clermont-Ferrand (OPGC) L-band Doppler radar, VOLDORAD 2B, used in collaboration with the Italian National Institute of Geophysics and Volcanology in Catania (INGV-CT), also detected the associated ash plumes, giving precise timing and duration for the lava fountains. This study resulted in the first detailed analysis of the OMI and AIRS SO_2 data for Etna's lava fountains during the 2011-2012 eruptive cycle. The HYSPLIT trajectory model is used to constrain the altitude of the observed SO_2 clouds, and results show that the SO_2 emission usually coincided with the lava fountain peak intensity as detected by VOLDORAD. The UV OMI and IR AIRS SO_2 retrievals permit quantification of the SO_2 loss rate in the volcanic SO_2 clouds, many of which were tracked for several days after emission. A first attempt to quantitatively validate AIRS SO_2 retrievals with OMI data revealed a good correlation for high altitude SO_2 clouds. Using estimates of the emitted SO_2 at the time of each paroxysm, we observe a correlation with the inter-paroxysm repose time. We therefore suggest that our data set supports the collapsing foam (CF) model [1] as driving mechanism for the paroxysmal events at the NSEC. Using VOLDORAD-based estimates of the erupted magma mass, we observe a large excess of SO_2 in the eruption clouds. Satellite measurements indicate that SO_2 emissions from Etnean lava fountains can reach the lower stratosphere and hence could pose a hazard to aviation.

1. Introduction

Basaltic volcanoes display a range of eruption styles, from relatively benign to highly explosive. Strombolian activity is characterized by short-lived, discrete explosions, whereas lava fountains involve more sustained jets of lava to heights of up to 1-2 km above the vent. Lava fountains can be sustained over several hours and expel molten clots of lava in a continuous shower (Vergniolle and Jaupart 1986; Vergniolle and Mangan 2000). They produce lava flows and gas emission (mainly water vapor [H_2O], carbon dioxide [CO_2] and sulfur dioxide [SO_2]) at the surface associated with ash plumes and fall-out deposits. According to Carn et al. (2008), SO_2 measurements are of great interest because they can act as a proxy for ash that is a hazard to aviation. Mt. Etna (Sicily, Italy; Fig. 2.1) is Europe's largest and most active volcano, and displays the full range of basaltic volcanic activity from quiescent, passive degassing to explosive lava fountains (or 'paroxysms'). With Etna it is not unusual for Catania airport to close during one of those paroxysms because of the emitted ash plume affecting aircraft. Furthermore, this kind of explosive basaltic eruption, increasingly common at Etna in recent years, can produce upper tropospheric plume altitudes (Bluth and Carn, 2008) and is therefore important for aviation hazard assessment. Despite this, gas and ash emissions from Etna paroxysms have not been studied in great detail to date.

SO_2 is a short-lived gas (Yan et al., 2012) that converts into sulfuric acid (sulfate) aerosols after a few days. Sulfate aerosol can have significant impacts on climate, the environment and health, providing motivation for measurement of volcanic SO2 emissions. SO_2 is the easiest volcanic gas to measure via remote sensing techniques since it is usually absent in the ambient atmosphere, in contrast to H_2O and CO_2. SO_2 is primarily released by anthropogenic activities (Cullis and Hirschler, 1980; Yan et al., 2012) such as fossil fuel burning and metal smelting. However, volcanic SO_2 has a much greater effect on climate due to its higher injection altitude, which prolongs its lifetime

and that of derived sulfate aerosol. When injected into the upper troposphere and lower stratosphere (UTLS) sulfate aerosol reflects incoming solar radiation (e.g. Laki eruption 1783; Sigurdsson, 1982), and can cause cooling of the earth for months or years. It is also important to monitor volcanic SO_2 emissions because its temporal changes can be precursors to volcanic eruptions and show variations in eruptive conditions (Young et al., 1998).

On the 12th of January 2011, Etna's new Southeast crater (NSEC) entered a new eruptive cycle and began a series of 25 paroxysms (lasting until April 24, 2012). Events typically started with Strombolian activity, evolving to lava fountains that fed dense ash and lapilli plumes. At the time of writing, Etna's New South-East Crater (NSEC) activity has started again after a quiescence of about 9 months and has already resulted in 13 further paroxysms. Although the volcanic activity is similar to the previous cycle (strombolian activity associated with lava fountains and lava flows), the current sequence features concurrent activity at the Bocca Nuova and/or the Voragine craters (Fig. 2.2). Therefore, in this study we focus on the previous eruptive cycle from January 2011 to April 2012.

In this project, I focus on satellite data from the Ozone Monitoring Instrument (OMI), which was able to measure SO_2 emissions for each Etna paroxysm. The aim was to quantify the mass of gas produced by Etna during those 25 events and to use the data to better constrain the driving mechanism of lava fountaining. To achieve this, the time of the eruption and plume altitude are the main parameters required to constrain the SO_2 mass as accurately as possible. The time of eruption was retrieved from ground-based Doppler radar data and the plume height from the online HYSPLIT trajectory model that can calculate archive trajectories of air parcels. Doppler radar has been found to be a very effective tool for measuring ejecta velocities, at high acquisition rates and close to the emission source, for both Strombolian and lava fountaining activity (Dubosclard et al. 2004; Gouhier and Donnadieu, 2011). The VOLDORAD (VOLcanological DOppler RADar) 2B was installed in a collaborative effort between the Observatoire de Physique du Globe de Clermont-Ferrand (OPGC) and the Institudo Nazionale di Geofisica e

Vulcanologia - Catania (INGV-Catania) and allows us to precisely constrain the onset of each paroxysm.

Although OMI provides high sensitivity to volcanic SO_2 emissions, it currently suffers from an anomaly that precludes complete coverage of some volcanic clouds. To compensate for this, we use independent Atmospheric Infrared Sounder (AIRS) SO_2 measurements (Prata and Bernardo, 2007). Moreover, the combined use of two instruments in NASA's polar-orbiting A-Train satellites constellation, OMI and AIRS, give us critical information on volcanic cloud altitude (Carn et al., 2009) and permit comparison and validation of near-coincident satellite measurements (see Appendix 8.3, 8.4 and 8.5). The measurement of SO_2 released to the atmosphere by volcanic eruptions is important in term of risk management. Therefore, the main goal of this project was to track the SO_2 clouds produced by the NSEC paroxysms at Etna and calculate the mass liberated in the atmosphere. In this thesis, we present the results of both OMI and AIRS measurements and use those data to argue that the collapsing foam (CF) model (Parfitt, 2004) is the dominant driving mechanism of lava fountains at Etna, as also suggested by previous work on more limited datasets (e.g., Allard et al., 2005).

2. Geological settings

Mount Etna volcano is located in Sicily, Italy. Its summit is currently 3330 m above sea level, and on its South-East flank is Sicily's second largest city, Catania. This stratovolcano, which is the largest (1250 km²) and tallest volcano in Europe, has a very complex volcanic evolution and geological location. Etna is an intermediate and intraplate volcano. The subduction of the Ionian plate under the European plate creates the volcanism of the Aeolian Islands. The formation and location of Etna in this context is not well understood. According to Schiano et al. (2001), the source region of Etnean magmas is changing and is experiencing a growing influence of Ionian subduction. Another possible explanation, according to Gvirtzman and Nur (1999), is an asthenospheric window with uprising mantle under the African plate.

There are currently five craters at the summit of Etna: (1) the Northeast Crater was created in 1911 and is the highest point of the volcano; (2) the Voragine and (3) the Bocca Nuova are together in the Central craters and were formed respectively in 1945 and 1968; (4) the Southeast crater was created in 1971 but its activity stopped in 2007. (5) A new pit crater formed on its East flank in November 2009, called the New Southeast crater (NSEC), hosting the present activity. This part of the summit is rapidly changing due to intense and frequent eruptive activity (Figure 2.1).

Etna is known to have had many eruptions of effusive and Strombolian types from the summit craters which pose relatively minor hazards in comparison to large, lateral effusive eruptions (e.g. 1669, 1991-93, cf. Smithsonian Institution Global volcanism program; Corsaro et al., 1996; Bousquet and Lanzafame, 2001) that represent a much greater threat to the surrounding populations and infrastructure. Explosive eruptions generating ash plumes, even of moderate intensity, cause disruption to air traffic in the vicinity of the volcano.

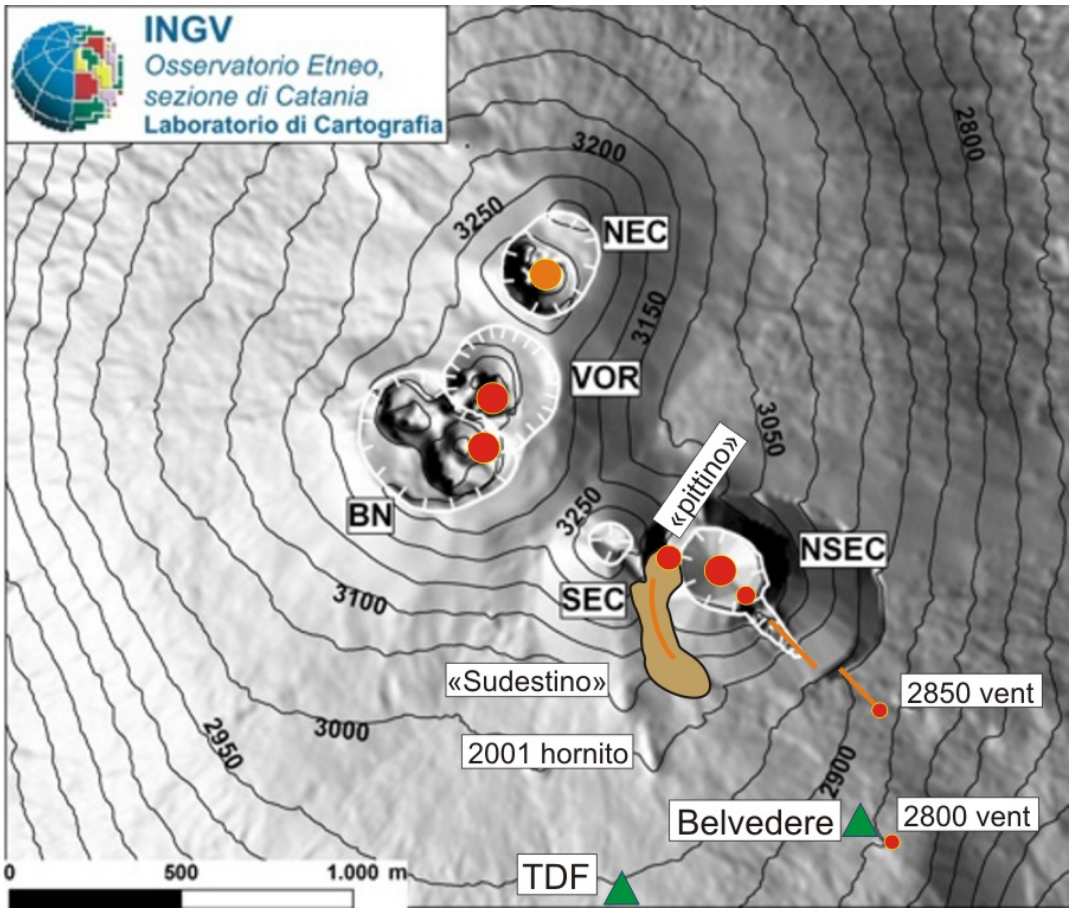

Figure 2.1: Map prepared by the Laboratorio di Cartografia of the INGV-OE of Etna's summit craters, showing the position of the eruptive vents active from February 20 to March 2, 2013. NEC=Northeast Crater; VOR=Voragine; BN=Bocca Nuova, SEC=Southeast Crater (not active since 2007); NSEC=New Southeast Crater; "Sudestino"=an eruptive vent that built a low cone at the southern base of the SEC cone in the spring of 2000; 2001 hornito=first eruptive vents to open during the 2001 flank eruption; 2850 vent and 2800 vent=eruptive vents that opened near the Belvedere monitoring station on 20-21 February 2013; TDF=Torre del Filosofo. Note that the vent of the NEC (shown in orange color) is open and contains degassing magma at depth since many years, but without any surface activity. Light brown area is the zone of the "saddle" between the two cones of the SEC, which collapsed during the 28 February 2013 paroxysm. Orange lines are eruptive fissures in the "saddle" and on the southeastern flank of the NSEC cone, which have been repeatedly active since the early morning paroxysm on 20 February 2013. © INGV - Istitituto Nazionale di Geofisica e Vulcanologia - All rights reserved.

Etna has also produced Plinian eruptions in the past, as in 122 B.C when a violent explosive eruption took place which generated a sustained ash plume and caused fatalities (VEI 5 according to Smithsonian Institution; Coltelli et al., 1998). Moreover, the Valle del Bove is a depression of high interest because it is interpreted as the result of several caldera collapses occurring at the various secondary eruptive centers at the end of their

activity (80 ka - 64 ka BP; Klerkx, 1970; McGuire, 1982; Guest et al., 1984). Enhanced by erosion, this valley allowed volcanologists to study in the field the evolution of an ancient volcano (Trifogglieto; Calvari et al., 1994a).

Until 2000, typical activity of Etna was mainly effusive but since then its activity has changed in style and become accompanied by more explosive behavior. An increase in the frequency of effusive activity has also been noticed (Behncke et al., 2006, Andronico and Corsaro, 2011). The style of activity has implications for volcanic hazards since, while both lava flows and explosive activity pose hazards, the potential impacts and mitigation strategies differ. In terms of explosive activity, explosive events associated with the 2001 and 2002-2003 eruptions produced ash plumes that caused disruption of air traffic and closure of Catania's international airport (Calvari et al., 2011). Episodes of lava fountaining, which are also referred to as paroxysms, are often observed at the summit craters. They are also associated with fountain-fed lava flows and the generation of ash plumes, during their climax. A new cycle started in January 2011 and lasted for about 1.5 years, including a total of 25 paroxysms (e.g. Ganci et al., 2012), which are the focus of this study. Renewed fountaining activity at the NSEC began in February 2013, about 10 months after the previous paroxysm in April 2012. As of June 2013, 13 new paroxysms have taken place at the NSEC and 38 paroxysms since the beginning of lava fountaining in this new pit crater in January 2012. However, it is important to note that the activity has not been confined to the NSEC but has also occurred in the BN, the NEC and the Voragine. Such simultaneous volcanic activity in the NSEC and BN has not been seen in about 12 years. The activity at the BN restarted in July 2012 after 1 year of inactivity and is showing vigorous intracrater Strombolian explosions. For the Voragine, it started after 13 years of quiescence in February 2013.

INGV is in charge of continuously monitoring Etna and provides information in real-time to the Civil Protection. The instrumental network at Etna comprises traditional geophysical and remote sensing methods including arrays of broadband seismometers, infrasound sensors, thermal and visible cameras, and satellite data. Since July 2009,

OPGC also deployed a ground-based Doppler radar at La Montagnola (VOLDORAD 2B, Donnadieu et al., 2009; http://wwwobs.univ-bpclermont.fr/SO/televolc/voldorad/) to help with monitoring the explosive activity of the summit craters in all weather conditions. The radar data are jointly exploited through a collaborative agreement between OPGC and INGV and were acquired by VOLDORAD 2B.

Finally, Etna is an excellent case study for SO_2 degassing since it is known as one of the strongest sources of volcanic SO_2 on the planet (Allard, 1997). This huge amount of gas can be released by continuous passive degassing but also during explosive eruptions that form volcanic clouds that can drift in the atmosphere for several days and travel long distances from Etna. The SO_2 emissions associated with Etnean lava fountains are not very well constrained but ground-based SO2 measurements are currently made in real time by the INGV using UV spectrometers (mini-DOAS) to detect the SO_2 cloud. This network is called FLAME (FLux Automatic MEasurements) and was installed in 2004 on Etna flanks to measure SO_2 fluxes at high frequency (every ~6 minutes; Burton et al., 2004; Salerno et al., 2009b). However, this type of measurements is operating only during daylight hours and often misses the paroxysms if they occur at night. Another problem arises from the presence of ash plumes since this method requires a clear-sky background and the SO_2 plume can be quite wide. It can prevent SO_2 retrievals and therefore satellite remote sensing measurements are important to better constrain the SO_2 emissions.

3. Methodology

3.1 OMI

The Ozone Monitoring Instrument on NASA's EOS/Aura satellite was launched in July 2004. This UV/Visible Spectrometer can measure total column amounts of ozone and other trace gases such as SO_2, nitrogen dioxide (NO_2) BrO, and HCHO (S.Carn OMI data guide, 2012). OMI is of great interest since it retrieves SO_2 from space with a high spatial and spectral resolution (Krotkov et al. 2006), relative to previous UV satellite instruments, with daily global coverage until 2008 (see below). Previous instruments have been used to measure SO_2 in the atmosphere, such as the Total Ozone Mapping Spectrometer (TOMS), but OMI's detection limit for SO_2 is about 2 orders of magnitude smaller than TOMS (Krueger et al. 1995).

The hyperspectral UV/Visible spectrometer has a 2600 km swath and detects backscattered solar radiation with a two-dimensional charge coupled device (CDD). In our project, we used data from the 310-365 nm UV-2 band with 0.42 nm spectral resolution (cf. Table 3.1 and figure 3.1). OMI is a pushbroom sensor that collected data for the swath in 2 seconds intervals, giving a 13 km along track resolution. The CCD pixels in one dimension are binned to create 60 cross-track positions corresponding to 24 km cross track resolution at nadir.

Level 2 (L2) OMI data (representing retrieved trace gas products) are publicly available and can be downloaded from the NASA GES DISC (Mirador) website http://mirador.gsfc.nasa.gov/cgi-bin/mirador/collectionlist.pl?keyword=omso2. We are primarily interested in the OMSO2 swath data (OMI/Aura Sulphur Dioxide (SO_2) Total Column 1-orbit L2 Swath 13x24 km). This gives us individual orbits that usually number 14-15 per day achieve global coverage. However, since May 2008, OMI measurements have been impacted by a row anomaly (a blockage in the sensor's field-of-view, which

varies dynamically over time) which results in a data gap affecting parts of the swath (OMSO2 Readme file; http://www.knmi.nl/omi/research/product/rowanomaly-background.php)

Table 3. 1 : Aura and OMI principal parameters (OMI data guide, 2012).

Orbit	Polar, sun-synchronous, in the 'A-Train'
Orbit altitude	705 km
Ascending node	13:42 local time
Viewing angle	114°
Swath width	2600km
Pixel size	13 x 24 km at nadir
Wavelength ranges	270-310 nm (UV1)
	310-365 nm (UV2)
	365-504 nm (Visible)
Spectral resolution	0.42 nm (UV2)

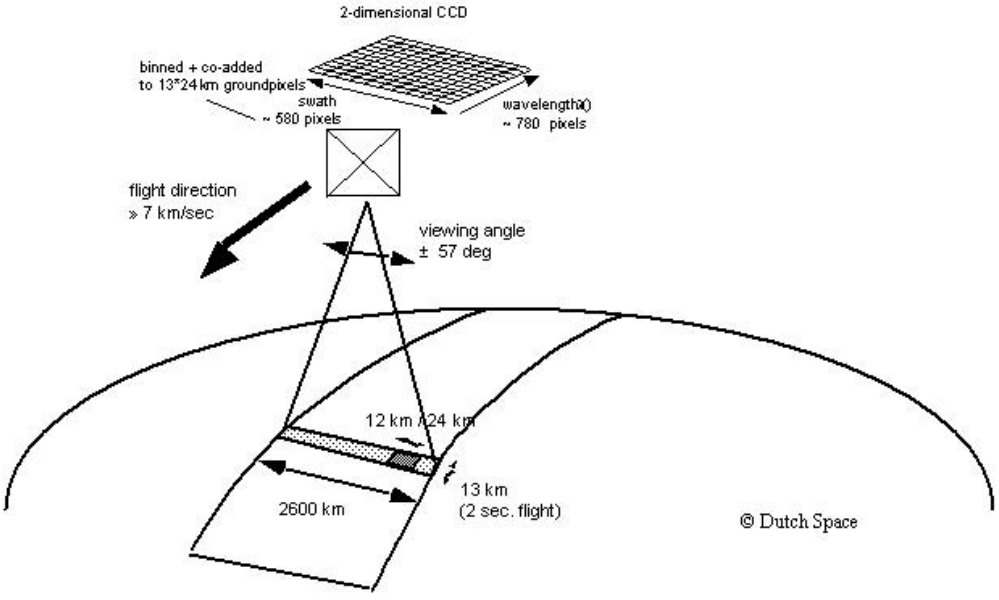

Figure 3.1: Sketch of the Aura Ozone Monitoring Instrument (Levelt et al., 2006; See Appendix 8.9 for documentation of permission to republish this material).

OMI allows volcanologist to study and track the SO_2 emission from volcanic eruptions almost anywhere in the world as well as passive degassing of volcanoes thanks to its high sensitivity (Krotkov et al. 2006). It is also sensitive enough to measure anthropogenic pollution produced by fossil fuel burning power plants and smelters (China; Krotkov et al., 2008).

The OMIplot software (Carn, 2011b) written in Interactive Data Language (IDL), permits OMI data processing and visualization of OMI data products including the column density of SO_2 in Dobson Units (1 DU = 2.69×10^{16} molecules/cm^2) for 4 different altitudes: the Planetary Boundary Layer (PBL) corresponding to a Center of Mass Altitude (CMA) of 0.9 km, the Lower Troposphere (TRL) corresponding to a CMA of 2.5 km, the Middle troposphere (TRM) corresponding to a CMA of 7.5 km, and the Upper troposphere and Lower Stratosphere (STL) corresponding to 17 km. The altitude assumption is required since the retrieved SO_2 column is altitude-dependent, but since the injection height of volcanic SO_2 varies significantly the actual SO_2 altitude is not known (and cannot be realistically inferred) at the time of the OMI measurements.

OMIplot was used to analyze the L2 OMI SO_2 data files from NASA and create images of the SO_2 cloud transport. To date, two different algorithms have been used to produce operational SO_2 column data from OMI: the Band Residual Difference (BRD, Krotkov et al., 2006), and the Linear Fit algorithm (LF, Yang et al. 2007). OMIplot primarily uses the LF algorithm to produce the TRL, TRM and STL columns, which are the layers of most interest for the study of Etna's SO_2 volcanic emissions. Furthermore, the LF algorithm is more suitable for analysis of volcanic SO_2 emissions because it takes into account the non-linearity of SO_2 retrievals above ~20 DU (OMSO2 Readme file). Initially, the BRD technique was used for OMI SO_2 retrievals but the LF algorithm improved the measurements, especially for cases with high SO_2 column amounts like large volcanic eruptions (Yang et al., 2007; Krotkov et al, 2010). After Krotkov et al (2010), the LF algorithm calculates the radiance residuals as the difference between the measured and computed N values:

$N = -100 \times \log_{10}(I/F)$, where I is Earth radiance and F is solar irradiance.

To consider multiple Rayleigh scattering, ozone absorption, ring effect and surface reflectivity, this algorithm uses a vector forward radiative transfer model (Krotkov et al., 2010).

The aim of this project was to quantify the SO_2 mass produced by each paroxysm from the NSEC of Etna, using the Normalized Cloud-mass (NC) technique. From S.Carn (OMI guide, 2012), the procedure selects a region of interest encompassing the volcanic cloud and calculates the SO_2 mass ($SO2_{cloud}$) for a certain area (A_{cloud}), followed by a background region free of SO_2 with the same dimension and similar meteorological cloud features. The SO_2 mass of the background ($SO2_{back}$; corresponding to background retrieval noise) and its area (A_{back}) are used to deduce the SO_2 cloud mass using the following equation (see Appendix 8.2):

$$SO_2\ cloud\ mass = SO2_{cloud} - \left(\frac{A_{back}}{A_{cloud}} \times SO2_{back}\right)$$

3.2 HYSPLIT trajectory modeling

Since OMIplot calculates a mass of SO_2 at a certain prescribed altitude we need to correct for the actual altitude of the volcanic cloud. To estimate the latter, we used the online HYSPLIT trajectory model (http://ready.arl.noaa.gov/HYSPLIT_traj.php) that can reconstruct forward and backward air parcel trajectories for specified altitudes using model wind fields. From our OMI images of the volcanic clouds, we extracted the coordinates of the cloud location for the highest SO_2 columns at the leading edge (assuming that this was more accurate). HYSPLIT was then used to calculate back trajectories of the volcanic cloud at various altitudes from these coordinates and the date and time of the OMI overpass. The altitude of the trajectory that best matched Etna's location was assumed to represent the SO_2 cloud altitude. Sometimes, the INGV-Catania reports, which describe the volcanic activity for each paroxysm, also gave information on

the plume height at the vent. However, plume altitude can change during transport downwind from the vent.

An example of this back trajectory technique is shown in Figure 3.2 and 3.3 for the case of the 9th paroxysm (August 5, 2011) corresponding to the 4th day of SO_2 plume dispersion. This analysis was conducted for each paroxysm and each day of OMI images since the plume altitude is often variable during its dispersion in the atmosphere (see Appendix 8.1)

Using the HYSPLIT-derived plume height for each paroxysm, we then linearized the SO_2 mass for the estimated altitude using the two OMI CMAs bracketing this altitude (e.g. if the estimated plume height was 10 km, we used the SO_2 mass calculated at 7.5 (TRM) and 17 km (STL)). We thus derived the corrected SO_2 mass for each OMI SO_2 image.

This type of calculation is influenced by errors. In this case, the main source of error is the plume height since the LF algorithm gives different SO_2 column retrievals for different altitudes. We estimated the SO_2 mass error to be about ±20%. The altitude-related error is largest for SO_2 altitudes below ~5 km. But other factors such as ash interference and opacity of the initial plume can also affects our measurements for OMI overpass close to the onset of the eruption and lead to some underestimation of the SO_2 mass calculation. This is only valid when the plume is close to the vent since the ash seems to fall out quite rapidly during the paroxysms once the plume has drifted away from Etna.

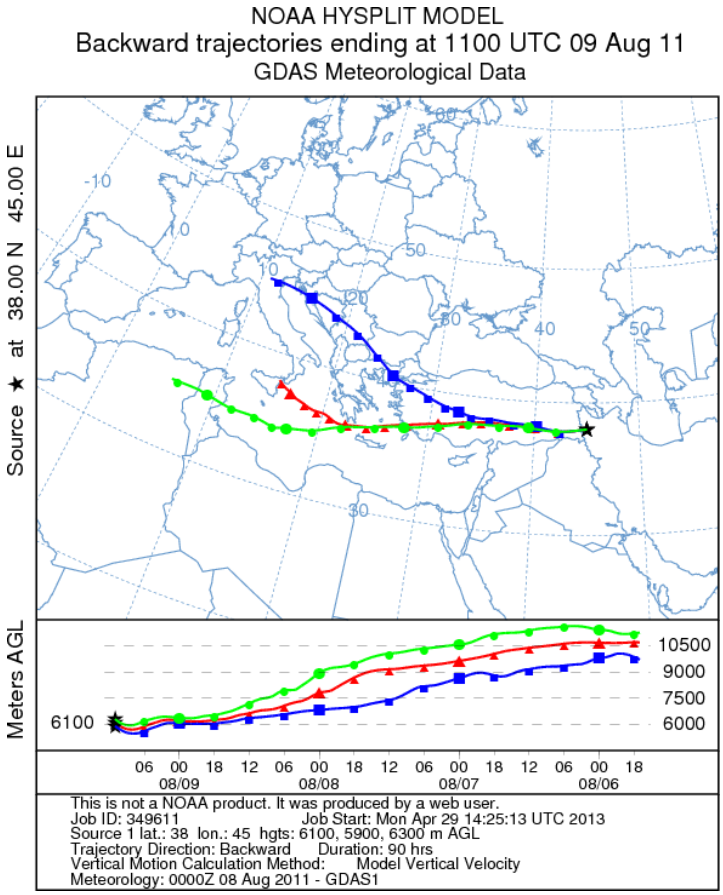

Figure 3.2: HYSPLIT trajectory model for the case of the 9th paroxysm on August 5, 2011. The red line passing above Etna (6100 m) is the selected plume height for August 9 at 11:00 UTC.

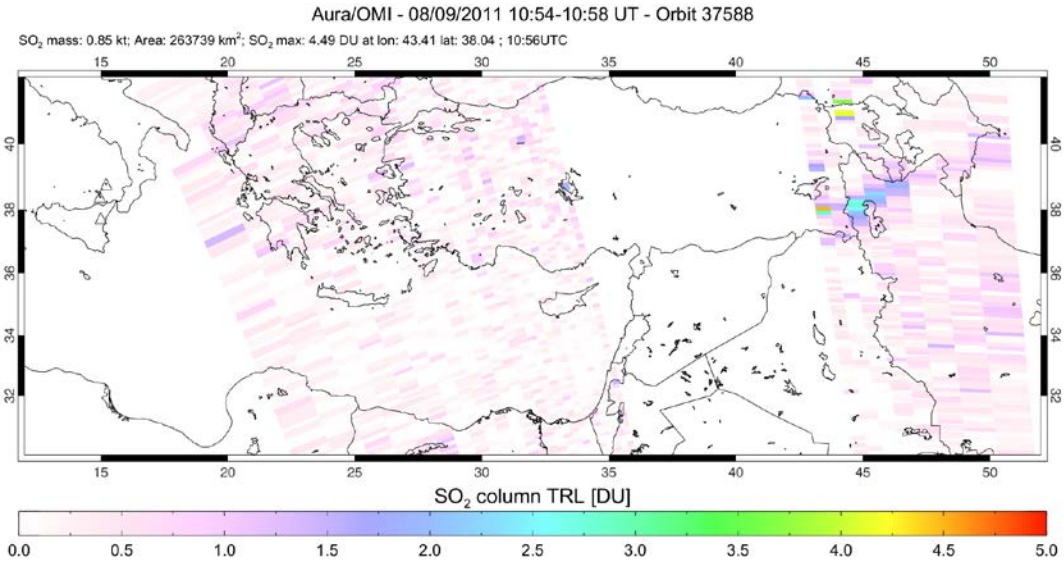

Figure 3.3: OMI SO_2 image showing the location of the SO_2 plume on August 9, 2011 at 10:54 UT used for the HYPLIT back trajectory estimation.

3.3 AIRS

To compensate for data gaps due to the OMI row anomaly, where all or part of the SO_2 cloud may be missed, we use IR (AIRS data). This instrument flies on Aqua in a sun-synchronous polar orbit with a local equator crossing time of 13:30 (Prata and Bernardo, 2007). Like Aura, Aqua is part of the A-Train satellite fleet, flying ~15 minutes ahead of Aura. Thus AIRS and OMI make measurements within ~15 minutes of each other (actually ~8 minutes in recent years due to a new A-Train configuration). AIRS is an echelle grating spectrometer that covers the strong SO_2 absorption band at 1362 cm^{-1} (v3-band), permitting measurements of SO_2 column abundance (Prata and Bernardo, 2007). The instrument scans with the following parameters: swath of 49° from nadir, 1.1° field of view, and 15x15 km^2 pixel dimensions at nadir.

The advantage of AIRS is it provides 2 images per day, one during the day and one at night, unlike OMI that requires UV (sunlight) to make measurements. However, the sensitivity of AIRS to SO_2 is lower than OMI with an accuracy of about 6 D.U (Prata and Bernardo, 2007) and it therefore has greater errors. Nevertheless, AIRS data were used to track SO_2 clouds on days affected by the OMI row anomaly, and also to increase the number of observations for all paroxysms (see Appendix 8.3, 8.4 and 8.5).

AIRS data are also publicly available online from NASA and the specific data product used here is the AIRS/Aqua Level 1B (L1B) Infrared Radiances (http://mirador.gsfc.nasa.gov/cgi-bin/mirador/homepageAlt.pl?keyword=AIRIBRAD). These data are geolocated and calibrated radiances and the processed images have 2378 channels (high spectral resolution) comprised of 90 pixels by 135 lines (Manning, 2002; Prata and Bernardo, 2007). All our L1B AIRS data were processed using the Prata and Bernardo (2007) retrieval algorithm using a r^2 correlation threshold of 0.5 that can detect weak volcanic activity with a minimum of 100 tons of SO2. This method of retrieval created by Prata and Bernardo (2007) also considers the effect of water vapor across the

wavelength band.

Another goal of this project was to compare the OMI and AIRS SO_2 retrievals for Etna's eruption clouds to see how well they agree. However, some prior studies by Prata and Bernardo (2007) and Carn et al (2005) show that for SO_2 above 8 km altitude the two techniques are in good agreement and below 8 km, AIRS values are 2 to 3 times lower than OMI.

3.4 SO_2 decay rate

The last stage of the analysis is to find the initial SO_2 mass for the onset of the eruption. For that, both OMI and AIRS measurements were corrected for each paroxysm by assuming exponential SO_2 loss to infer the amount of SO_2 emitted at the beginning of the paroxysm (Krotkov et al., 2010). SO_2 is a short-lived gas in the lower troposphere with an annual average lifetime of 1-3 days (Chin et al., 2000; Barrie et al., 2001) but it has a much longer lifetime when released by large volcanic eruptions since it can reach the stratosphere (Prata and Bernardo, 2007). Unfortunately, use of an exponential fit was precluded for some paroxysms due to insufficient data points; we therefore had to do some extrapolations for those cases. Different methods were used such as: the average exponential decay rate, or the plume height decay rate. The first technique was based on the average of all the paroxysms that had at least 2 data points and we used this value to extrapolate for the other cases (with only one data point available); this was made for the two instruments OMI and AIRS but mainly used for AIRS measurements. For the second technique, we identify the paroxysm with the closest plume altitude and detection time and use the corresponding SO_2 decay rate to estimate the initial SO_2 mass (since AIRS doesn't give an accurate altitude, this was used only for the OMI measurements). This last method was preferred for the estimation of the initial SO_2 mass for OMI data because we supposed that the SO_2 decay rate is related on the cloud altitude (theoretically the higher the altitude is, the lower decay rate we should get and the longer residence time of the SO_2 in the atmosphere).

3.5 OMI-AIRS validation

The near-coincident measurements by OMI and AIRS in the A-Train permit inter-comparison and validation of the UV and IR SO_2 retrievals. Although comparisons of total SO_2 mass in a volcanic cloud are useful (e.g., Prata and Bernardo, 2007), in this work we use an IDL routine to compare the OMI and AIRS SO_2 data on a pixel-by-pixel basis in a number of Etna's eruption clouds. For each SO_2 cloud with matching AIRS and OMI data (the daytime AIRS overpass corresponding to the OMI overpass), we were able to examine the correlation between the 2 methods. In our approach, for each OMI pixel the code finds the AIRS pixel with the closest SO_2 column amount at a range of distances from the OMI pixel center (distances of 0.1º, 0.2º, 0.3º, 0.4º and 0.5º are used). For each distance, a plot of AIRS SO_2 vs. OMI SO_2 is produced, and if there is a good correlation a linear regression correlation coefficient is added to the plot. Usually the correlation will improve as the distance from the OMI pixel increases because the possibility of finding the same SO_2 column amount increases. It is also due to the 15 minutes delay between the OMI and AIRS retrievals, since the cloud can be moving quite fast during this interval. The plot symbols are color-coded and represents the OMI cross-track pixel position i.e., it varies from 1-60 with 30 being nadir and 1 and 60 being extreme off-nadir positions. We generally expect a poor correlation between OMI and AIRS SO_2 columns for the off-nadir pixels as the OMI pixel size becomes very large and quite different from the AIRS pixel size and shape. Near nadir, the OMI and AIRS pixel sizes are more similar. It is possible to change the number of data points that are used in the linear regression by using a lower threshold of OMI SO_2 column amount. Different thresholds were tested such as 1 DU, 5 DU and 10 DU, to see how the correlation was affected.

3.6 Doppler Radar

Doppler radar principles and retrieved parameters

The radar installed on Mount Etna is a VOLcanological DOppler RADar (VOLDORAD 2B) located at La Montagnola ~3 km South-East of the NSEC. This ground-based pulse radar records continuously using the L-Band (wavelength = 23.5 cm) and is able to monitor all types of explosive activity (Donnadieu et al., 2009). It was created by the OPGC and set-up on Etna in collaboration with the INGV-Catania during June 2009 to monitor the eruptive activity of the summit craters.

Table 3.2: Characteristics of the VOLDORAD 2B radar created by OPGC and continuously recording Mt Etna's activity since 2009.

Caracteristics	Symbole	Voldorad 2B
Transmitted frequency (MHz)	ft	1274
Peak power (W)	Pt	60
Wavelength (cm)	ƛ	23.5
Antenna beam elevation (deg)	θ	15.5
Antenna beam width (deg)	α	9
Antenna beam azimut (deg)		350
Pulse repetition period (µs)	tr	100
Pulse duration (µs)	T	1
gate width (m)	L	150
thermal camera elevation angle (deg)	15	
thermal camera fov (deg)	18,8° (v) - 25° (h)	

The advantages of VOLDORAD are (Donnadieu et al., 2005): i) it can detect emissions of particles even in harsh weather conditions, ii) it can monitor volcanic activity remotely (from a distance of 0.3 – 11 km), and (iii) it can provide quantitative parameters in real-time. The radar has an elevation angle of 15.5° and a beam angle of 9° (Table 3.2). Each pulse lasts 1 µs and the pulse is emitted every 100 µs which makes the radar gate 150 m deep ($(c \times d_{pulse})/2 = 150\,m$, where c is the speed of light and d_{pulse} is the pulse duration). VOLDORAD 2B is able to detect particles crossing the antenna beam in up to 11 range gates ranging from 3135 m to 4635 m (these being slant distances from the radar) with G1 and G2 (at 3135 and 3285 m) being closer to the NSEC, as shown by the highest power recorded in these gates during all eruptions of NSEC.

During short duration deployments of the radar (Donnadieu et al., 2003, 2005, 2011; Donnadieu, 2012; Dubosclard et al., 2004; Gouhier and Donnadieu, 2008, 2010, 2011; Mora et al., 2009; Valade and Donnadieu, 2011; Valade et al., 2012), temporal series of the raw signal (.srt data) were recorded. Because the monitoring is continuous at Mt Etna, the data format had to be modified to save storage memory. The spectra (.spe data, power spectral density as a function of the radial velocity range) are directly calculated and only the power values of each velocity class (64) are recorded, thus limiting the memory space requirements to 1 Gb/day. Therefore, with the radar spectrum we can use Fortran software called CALPV (Calcul de Puissance et Vitesse) to extract the power and radial velocity parameters for each time step and each gate. We then obtain processed temporal series of Power and Velocity to compare all eruptions (cf. reports of the OPGC on VOLDORAD website) and infer their dynamics.

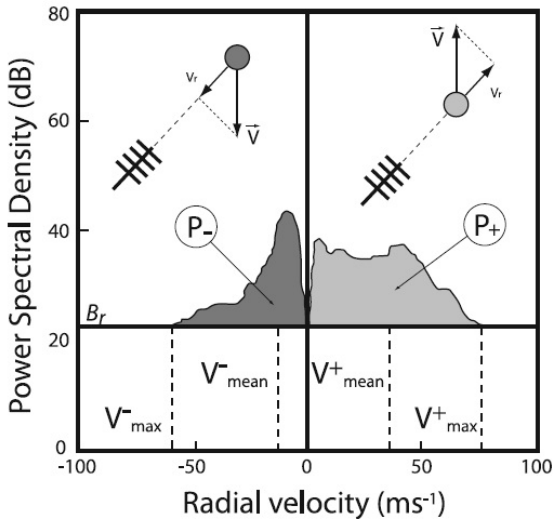

Figure 3.4: typical Doppler spectrum (Gouhier and Donnadieu, 2008). See Appendix 8.8 for documentation of permission to republish this material.

From Dubosclard et al. (2004), a target moving in one of the range gates produces a frequency Doppler shift Δf between the transmitted and received frequency equal to:

$\Delta f = -2ft \times (Vr/c)$ where c is the speed of light, ft the transmitted frequency and Vr the radial velocity of the target, i.e. the velocity component along the antenna beam

direction. Radial velocities are determined from the Doppler shift (Gouhier and Donnadieu, 2010). Therefore, particles moving away from the antenna (having a positive radial velocity) will induce a negative Doppler shift and vice versa. Furthermore, the negative velocity field (V-max≤Vr≤0) corresponds to particles with a component of motion toward the antenna and the positive velocity field (0≤Vr≤V+max) to particles with a component of motion away from the antenna (Dubosclard et al., 2004). In the particular configuration given in Figure 3.4, and for ballistic bombs and blocks in particular, ascending particles above the crater will have mainly positive radial velocities (away from the antenna) and descending particles will have mainly negative radial velocities (towards the antenna). This is more complex in the case of plumes where ash and lapilli are entrained in eddies while rising because of convection and turbulence, and also strongly influenced by the wind advection.

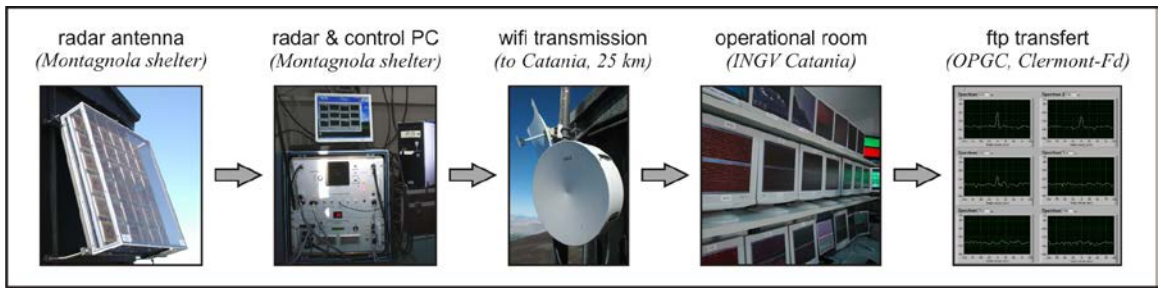

Figure 3.5: Operational diagram illustrating the successive steps of radar data acquisition and transfer. The radar antenna (without its radome here), located on Etna's southern flank (La Montagnola), transmits an electromagnetic wave and receives the echoes backscattered by the particles in the beam. The radar then amplifies, filters, and digitizes the received signal, which appears in real-time as Doppler spectra on the control PC in the shelter. Data are stored on a server in the shelter. From there the data is transmitted by WIFI to INGV's operational room in Catania (Sicily). At last, they are transferred to the OPGC (Clermont-Ferrand, France) by FTP, and displayed every 2 min on its website (http://wwwobs.univbpclermont.fr/SO/televolc/voldorad/TRetna.php). Modified from Valade 2012.

INGV-Catania receives the radar signal in their operations room which is permanently occupied (in continuous 8 hours shifts). A real time monitoring alert message is automatically sent by email at the beginning and the end of the eruptive signal (Figure 3.5).

Modeling

To estimate eruptive parameters such as the mass, particle concentration and mass flux from the paroxysms of Etna's NSEC, we decided to use a model based on a monodisperse (single particle size) particle-size distribution (PSD). Previous work on the grain size and density can be used to retrieve particle loading parameters with a faster but less accurate monodisperse model than polydisperse (Gouhier and Donnadieu, 2008). We can use either the Rayleigh or Mie (1908) electromagnetic scattering model to provide synthetic data of power backscattered by particles (Pr). A good approximation for small particles is the Rayleigh scattering theory, the validity limit of which depends on the radar wavelength (Sauvageot, 1992). Here, we can use this approximation for particles of diameter smaller than λ/4 which corresponds to about 5.9 cm called the validity limit (D_L) (Figure 3.6; Gouhier and Donnadieu, 2006).

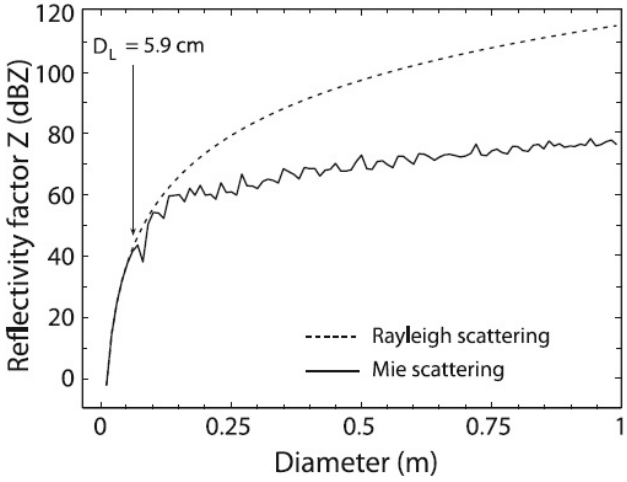

Figure 3.6: Synthetic reflectivity factor (Z, expressed in dBZ) as a function of particle diameter. Note the large overestimation of Z for large diameters when computed using the Rayleigh approximation [Gouhier and Donnadieu, 2006].

If we assume that we can use the value of grain-size from samples of the 12th paroxysm of the NSEC (29 August 2011) for every episode, with a mean particle size between 11.2 and 16 mm (Bonny, 2012), the Rayleigh theory is a good approximation for the proximal part of the ash and lapilli plume fed from the lava fountains. However, to model the lava fountain (with larger particles) we need to use Mie theory with a diameter about 0.1 m.

The aim is to find a synthetic power equal to that observed during the given paroxysm and to extract the eruptive parameters. In this model, the synthetic power is defined as $Pr = Cr \times (\eta / r^4)$ where Cr is the radar constant, η is the radar reflectivity and r the slant distance between the radar and the target. The reflectivity factor Z is defined by Sauvageot (1992) as a function of the radar reflectivity (η), the radar wavelength λ, and the particle complex dielectric factor K ($Z = \int N(D)\, D6\, dD$; see Gouhier and Donnadieu, 2008 for more information about the model). There are two important requirements to use this model (Gouhier and Donnadieu, 2008): i) the power used as input to the inversion model is defined carefully and ii) the reflected power is integrated throughout the entire duration of the explosion as the uprising plume passes vertically across the range gates concerned.

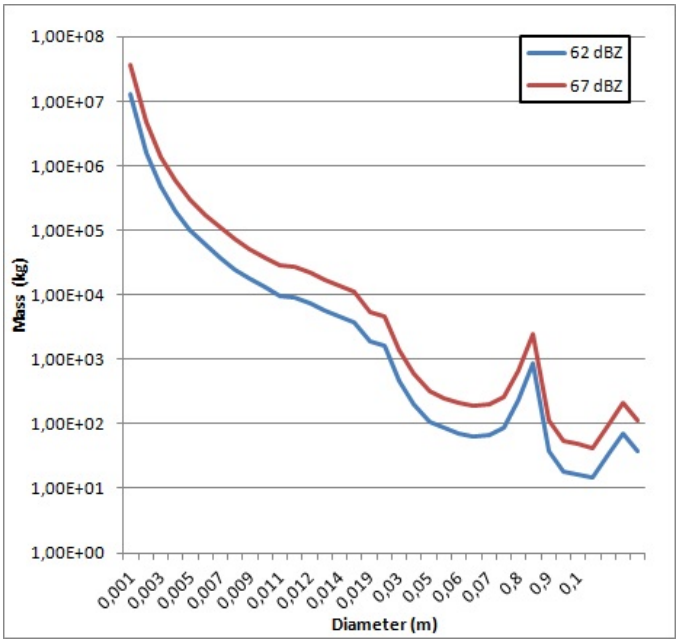

Figure 3.7: Mass against particle diameter for a given reflectivity factor Z. The red line of 67 dBZ corresponds to the maximum power of lava fountain and the blue line to the convecting plume.

In figure 3.7, we can see that the estimation of the mass increases rapidly when we have small particles. Above a size of 0.02 m Mie theory is applied because a small difference is found with the Rayleigh theory. This graph shows that the mass of small particles required to generate a given reflectivity can be up to several orders of magnitude higher

than the mass of larger particles giving the same reflectivity (Gouhier and Donnadieu, 2008). Small particles play an important role in the estimation of the mass because they contribute most to the total estimated mass. For instance, a reflectivity of 67 dBZ requires $3.74.10^7$ kg of 0.001 m particles compared to $3.74.10^4$ kg of 0.01 m particles a difference of 3 orders of magnitude. It is therefore important to know in our modeling because we have particles of about 1 cm. Moreover, the two curves follow the same trend: the red curve, corresponding to the lava fountains with high reflectivity, is above the blue curve of the convective plume with a constant offset between the two.

4. Results

4.1 HYSPLIT

Based on the OMI images, given a reference point, and the HYSPLIT trajectory model (http://ready.arl.noaa.gov/HYSPLIT_traj.php), we estimate the plume height for each day of each paroxysm (41 points). The HYSPLIT back trajectories also provide an estimation of the onset of the paroxysm, given by the time at which the trajectory intersects Etna, which we compare with our Doppler radar data. Since the time is estimated 'visually' from the HYSPLIT trajectories, there is some error involved (we assume ± 2-3 hours). Figure 4.1 shows a good agreement between the two methods, with the majority of the data having time differences less than 5 hours. We conclude that SO_2 emissions detected from space by OMI generally coincide with the peak lava fountain intensity detected by VOLDORAD 2B on the ground. Scatter in Fig. 4.1 is likely due to our use of a single reference point in each SO_2 cloud, and could perhaps be reduced by calculating multiple back-trajectories for each volcanic plume. However, ground-based and satellite-based measurements appear to be in agreement about the onset of the eruption at Etna's NSEC.

The HYSPLIT method is less accurate than the radar since it has a precision of only 2-3 hours, and there is some uncertainty in the model wind fields. The points that deviate from the VOLDORAD eruption timings by more than 5 hours could be explained by trajectory predictions that do not come directly from Etna, or as indicated by thermal camera videos of some paroxysms from INGV, some gas release may occur before radar detection of the lava fountain.

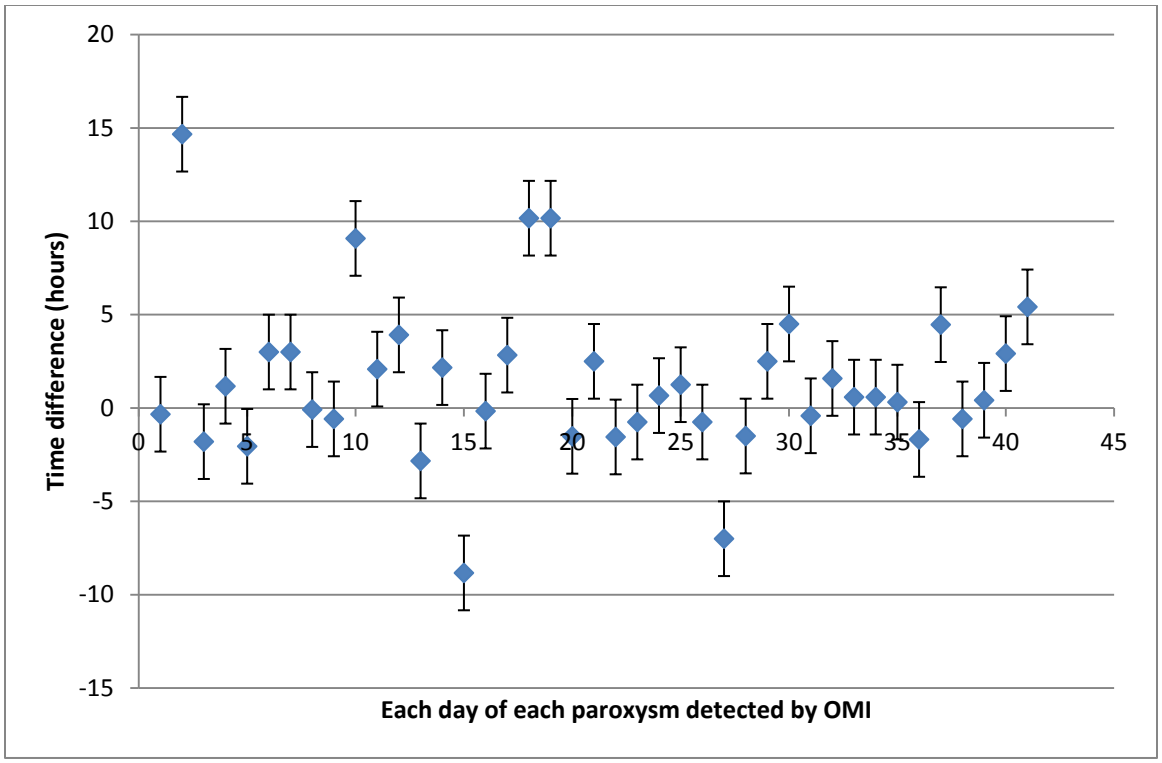

Figure 4.1: Graph showing the difference between the HYSPLIT estimation of the onset of the eruption and the radar for each measurement point starting with the 1st paroxysm on January 12, 2011. The negative time difference corresponds to early HYSPLIT prediction and positive difference to late prediction. Error bars of ± 2 hours.

4.2 SO_2 mass retrieval (OMI and AIRS)

OMI and AIRS SO_2 measurements allowed us to track the SO_2 clouds from Etna's NSEC for up to 4 days after emission (in the case of the 22 and 25th paroxysms). As examples, we show here 5 paroxysms where the OMI and AIRS coverage was able to follow the SO_2 cloud for the longest time and without data gaps, which corresponds to the 9th, 12th, 21st, 22nd and 25th paroxysms or respectively 5 August 2011, 29 August 2011, 4 March 2012, 18 March 2012 and 24 April 2012.

For the 2 first cases (9th and 12th paroxysms), the synergistic use of both OMI and AIRS data is useful because AIRS is able to give insight into the beginning of the eruption. For

instance, for the 9th paroxysm, in Figure 4.2a and 4.2b, AIRS is able to track the cloud the day after the eruption, whereas OMI was affected by the row anomaly. Likewise in Figure 4.3a and b, AIRS provides information on the cloud location for the 1st day of the eruption. In both cases, the cloud was better seen using OMI images from the TRL layer which correspond to a CMA of 2.5 km.

Furthermore, the SO_2 mass decay rate for the combined dataset gives a better correlation coefficient than the separate case (see Figure 4.4). For instance, if we only take into account the OMI values, as for paroxysm number 9, the corrected SO_2 mass at the onset of the paroxysm is 6430 tons with a R^2=0.78 with a decay rate of -0.018 but for OMI and AIRS together the corrected mass is 4400 tons with a R^2=0.81 and a decay rate of -0.013.

For the 12th paroxysm, the corrected SO_2 mass for both OMI and AIRS is 4230 tons with R^2=0.88 with a decay rate of -0.028, which we consider to be more accurate than the SO_2 mass derived from OMI data alone (with only 2 data points). Finally, it is not possible in these cases to compare the 2 methods of SO_2 retrievals since we don't have the AIRS overpass corresponding to the OMI overpass but the data are complementary.

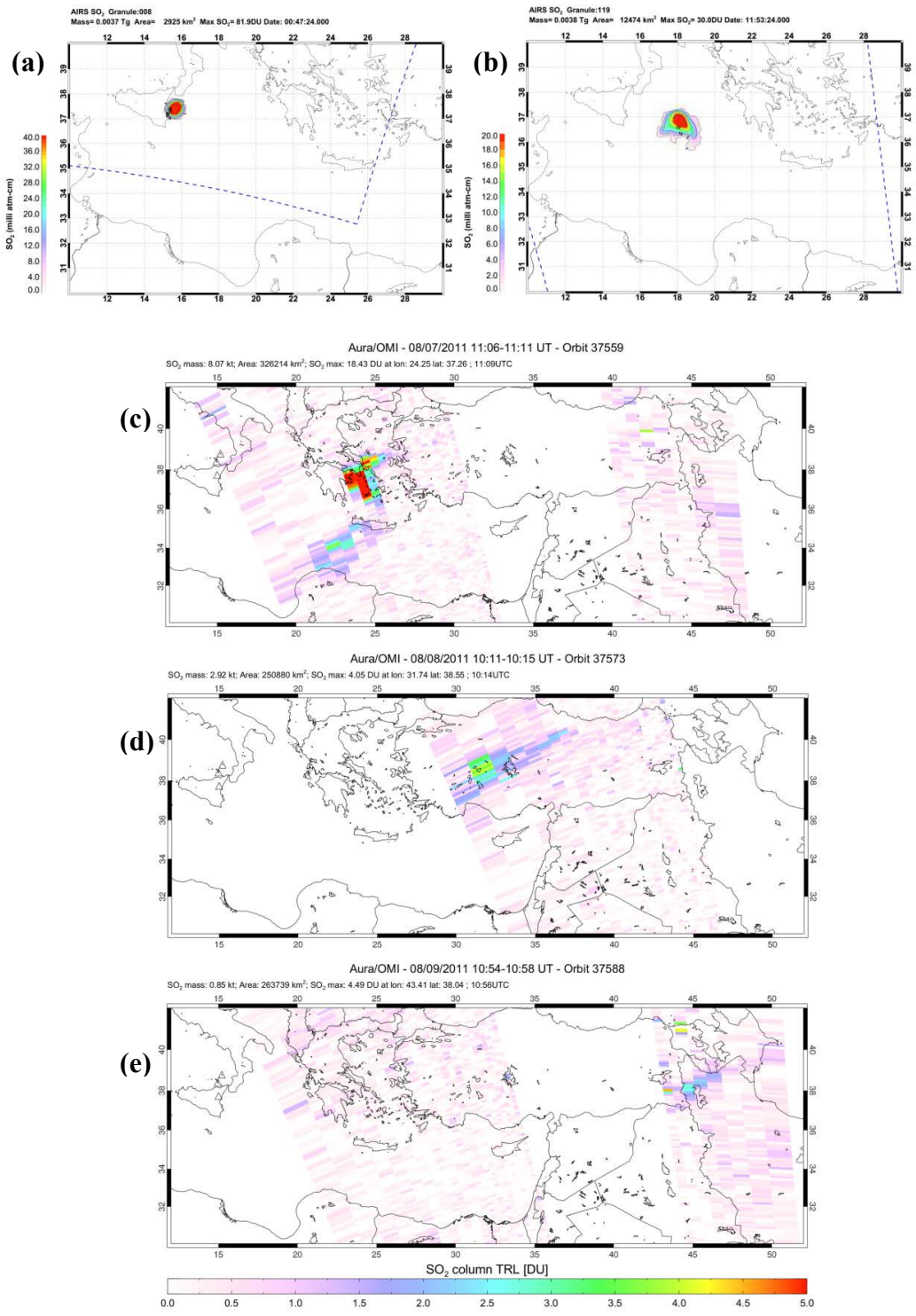

Figure 4.2: SO2 plume track from the 9th paroxysm. (a) AIRS overpass at 00:47 UT on August 6, 2011. Color scale shows retrieved SO2 vertical column amount in milli atm cm (equivalent to Dobson Units); (b) AIRS overpass at 11:53 UT on August 6; (c), (d) and (e) OMI overpasses from the next days. A black triangle indicates location of Etna; Note the different scale for OMI and AIRS images.

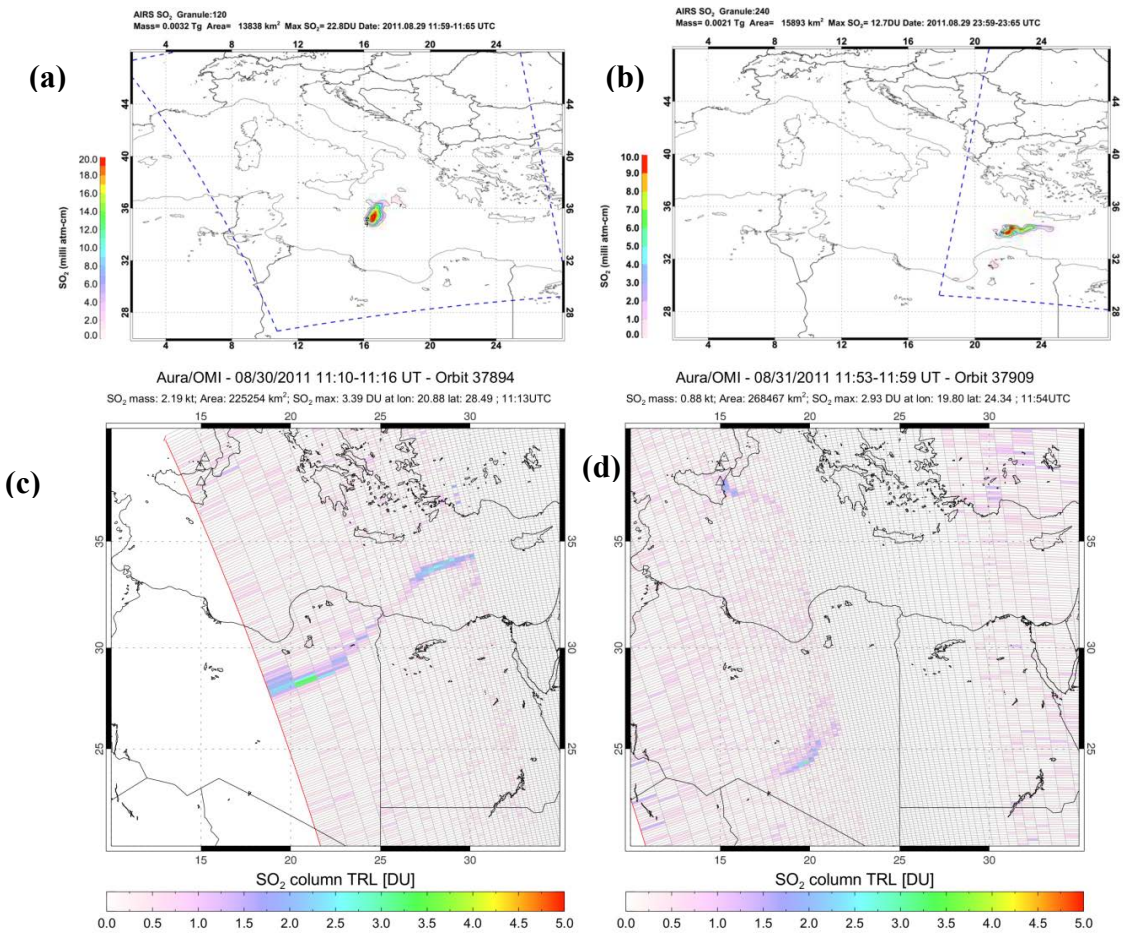

Figure 4.3: SO2 plume track from the 12th paroxysm on August 29, 2011. (a) AIRS overpass at 12:00 UT on August 29, 2011; (b) AIRS overpass at 00:00 on August 30, 2011; (c) and (d) OMI overpasses from the next 2 days. Note the different scale for OMI and AIRS images.

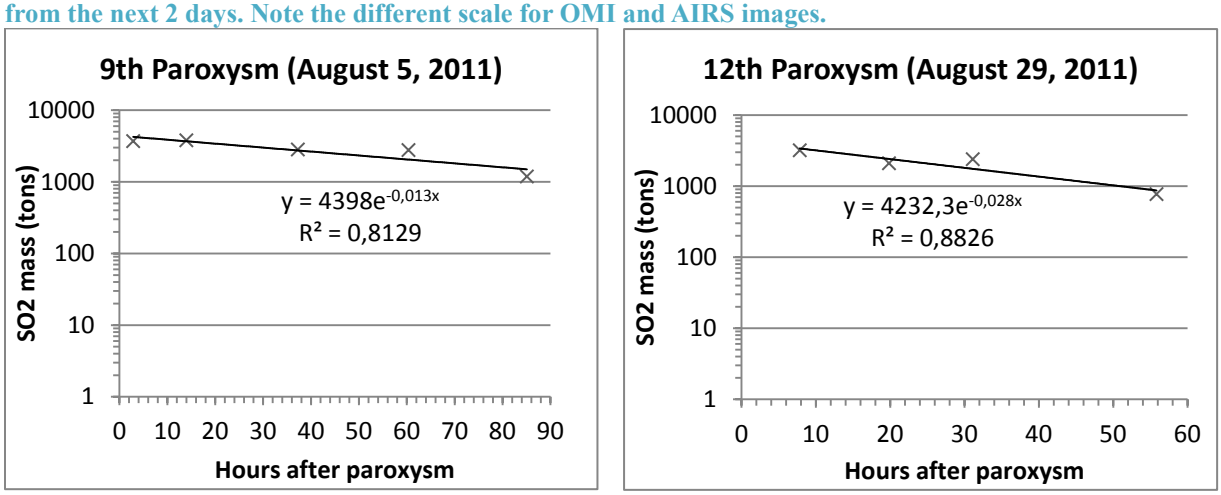

Figure 4.4: Graphs of the SO_2 decay from the combined data of OMI and AIRS.

21st Paroxysm (4 March 2012): The SO_2 cloud generated during this paroxysm was tracked further from Etna than any other in our study. The plume was observed over China approximately 2.5 days after the eruption (figure 4.5). The OMI images show the TRM SO_2 columns (7.5 km) and show the importance of monitoring volcanic SO_2 to prevent aviation hazards since this cloud was located at an altitude of 7-9.8 km during its propagation.

It is possible for this case to constrain the SO_2 cloud altitude better with the aid of AIRS data. In Table 4.1 the data show that AIRS consistently measures a lower mass of gas although it is comparable to OMI. This agrees with the idea that the cloud has reached the UTLS (above 5 km), and confirms the altitude estimation derived from HYSPLIT (http://ready.arl.noaa.gov/HYSPLIT_traj.php).

Based on the exponential SO_2 decay rate calculated from OMI observations, the mass emitted by Etna at the onset of the paroxysm was 9860 tons with R^2=0.84 (figure 4.6). It is however quite different from the equivalent AIRS estimate since the last 2 images give lower amounts of SO_2, the corrected mass being 5170 tons with R^2=0.05. Therefore, the link between this cloud and the paroxysm from the 6th of March, which is found very far from Etna, is questionable. Even though, HYSPLIT trajectories seem consistent with an origin from Etna and not an East African volcano, an increase of SO_2 gas after a few days in the atmosphere is unexpected.

In this case, we could get a near-coincident image of the volcanic cloud from AIRS and OMI, therefore the location of the plume can be compared. We find that in AIRS data, even if they are collected before OMI, the SO_2 cloud extent is smaller because AIRS has a higher limit of detection (another example can be seen in Appendix 8.6). However, the plume can be seen at the same location (figure 4.7). For instance, on March 6 at about 9:00 UTC, AIRS detected only 2600 tons of SO_2 whereas OMI measured 3960 tons.

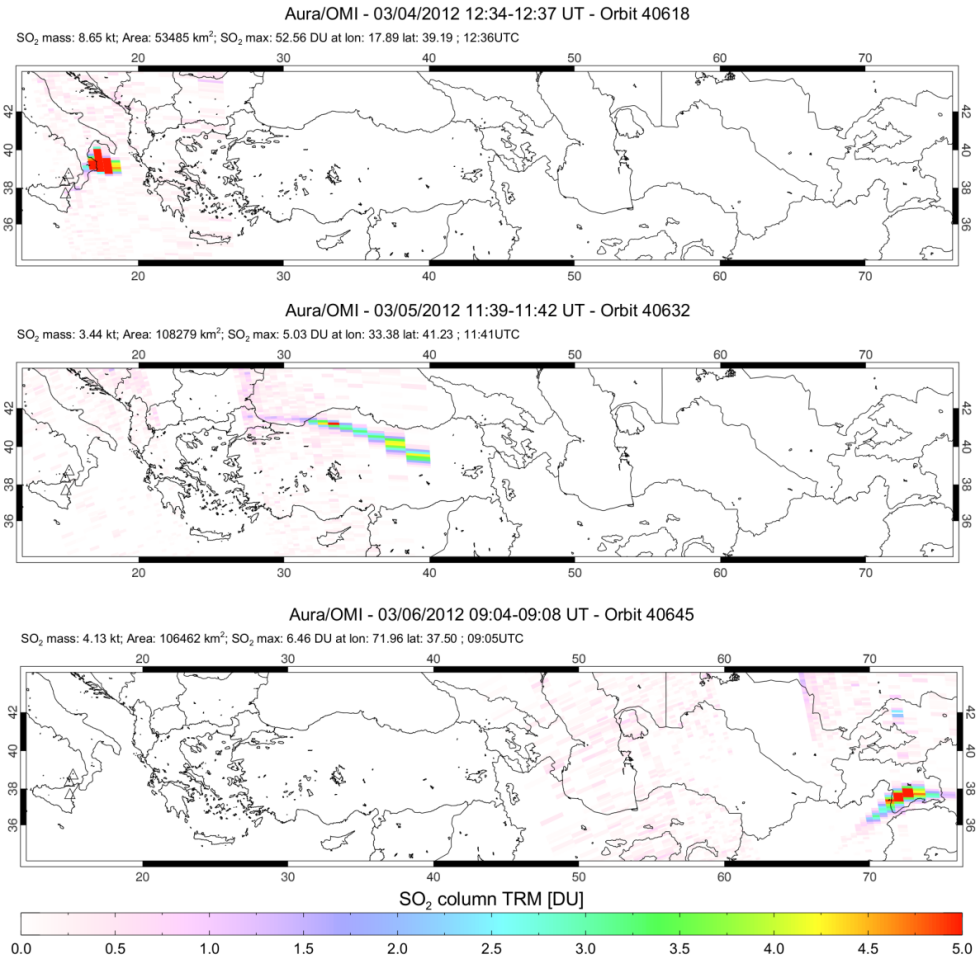

Figure 4.5: OMI images from the 21st paroxysm of the NSEC from the 4th of March, 2012.

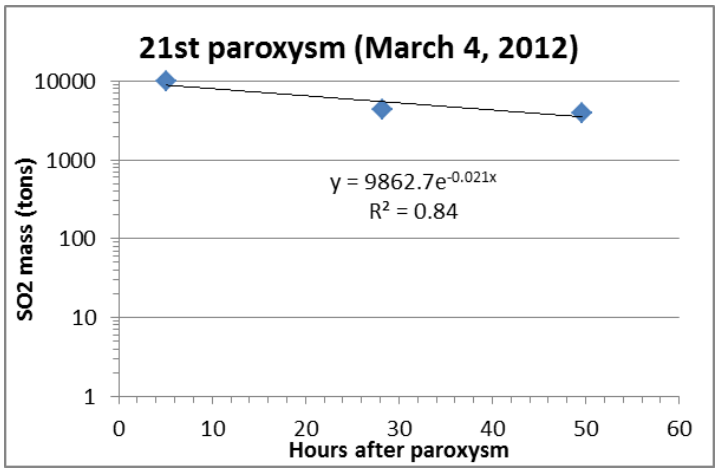

Figure 4.6: Graph of OMI SO_2 mass data from the 21st paroxysm. The exponential decay regression line with the equation is shown as well as the correlation coefficient.

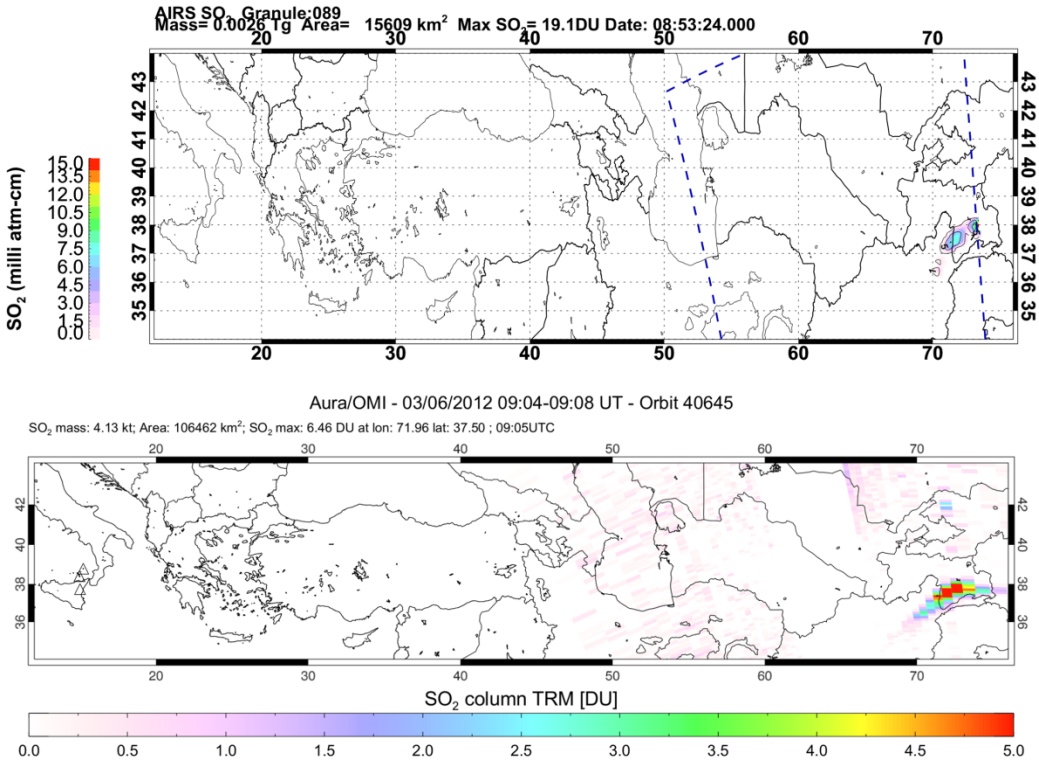

Figure 4.7: Comparison between AIRS and OMI images from March 6, 2012 (2 days after the onset of the eruption). Note the different SO_2 scale (milli atm-cm is the same as DU).

22nd Paroxysm (March 18, 2012): The SO_2 cloud from this paroxysm reached the highest altitude of any detected during this cycle; reaching an altitude of 11.2 km (UTLS). This is a good example since we have the most data points (10 in total with OMI and AIRS) that track the plume for 3 full days. In Figure 4.8, we can see the OMI images showing the dispersal of the cloud towards the South East, and it was last detected at the border between Afghanistan and Turkmenistan at 7.5 km altitude.

In Figure 4.9, 2 images of the 19th of March 2012, from OMI and AIRS allow us to see that the OMI row anomaly does not actually hide a part of the volcanic cloud since we have the coincident AIRS image. This also tells us that the SO_2 has reached the UTLS and detection by AIRS therefore confirms our plume height estimation. The AIRS image shows the same location of the SO_2 cloud about 15 min before the corresponding OMI overpass, although the SO_2 columns measured by OMI appear lower. This is verified by

the SO_2 mass retrieval where we can see that the AIRS SO_2 loading calculation is higher than the OMI SO_2 mass (except for the last day on March 21, 2012), 8800 tons measured by AIRS against 4790 tons by OMI. This difference with the previous paroxysm (#21) might be due the higher altitude of the volcanic cloud that makes it easier to detect by AIRS.

The SO_2 mass decreases with time and distance away from Etna (as expected) and the corrected SO_2 mass at the beginning of the volcanic activity estimated by OMI is 7210 tons with R^2=0.97 (Figure 4.10). The AIRS measurements gave also a good correlation coefficient of 0.92 but estimate a higher amount of SO_2 (14220 tons). The combined methods however, give a lower correlation number, therefore the OMI retrieval seems to be the most accurate. The higher estimate based on AIRS data is likely due to the lower sensitivity of AIRS to SO_2 relative to OMI, causing a more rapid 'decay' in the measured SO_2 mass and a possible overestimate of the paroxysmal SO_2 emission.

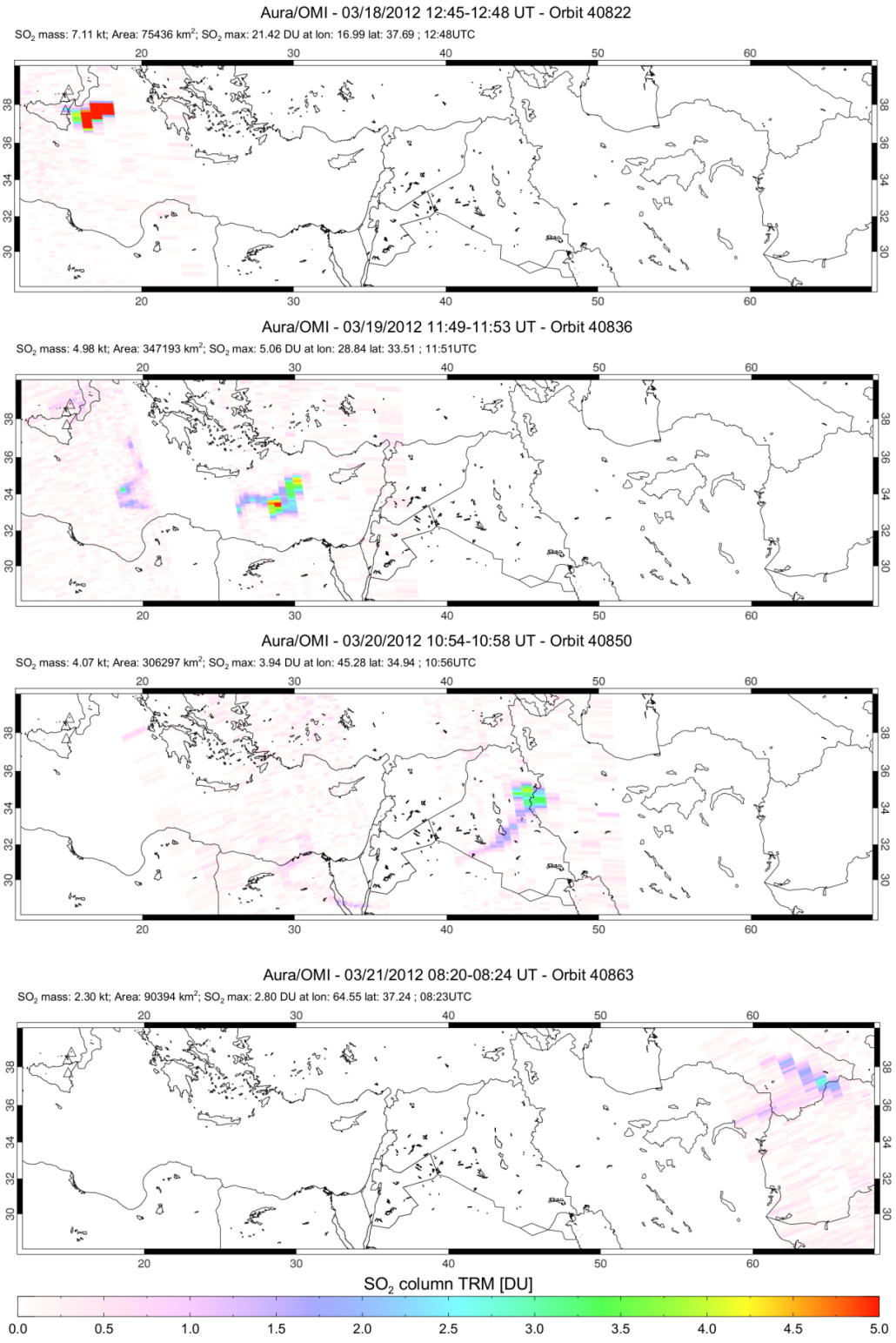

Figure 4.8: OMI images from the 22nd paroxysm of the NSEC.

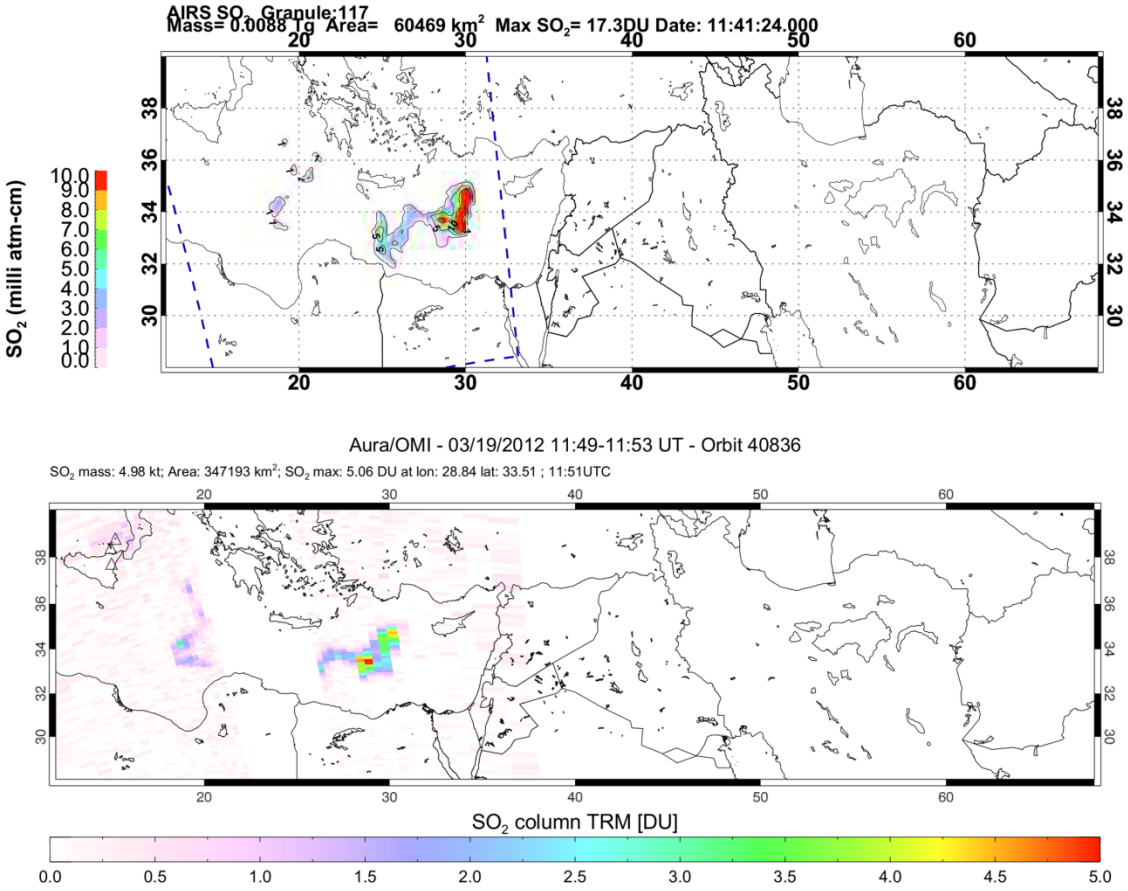

Figure 4.9: Comparison between AIRS and OMI images from March 19, 2012 (1 day and a few hours after the onset of the eruption). Note the different SO2 scale in the 2 images.

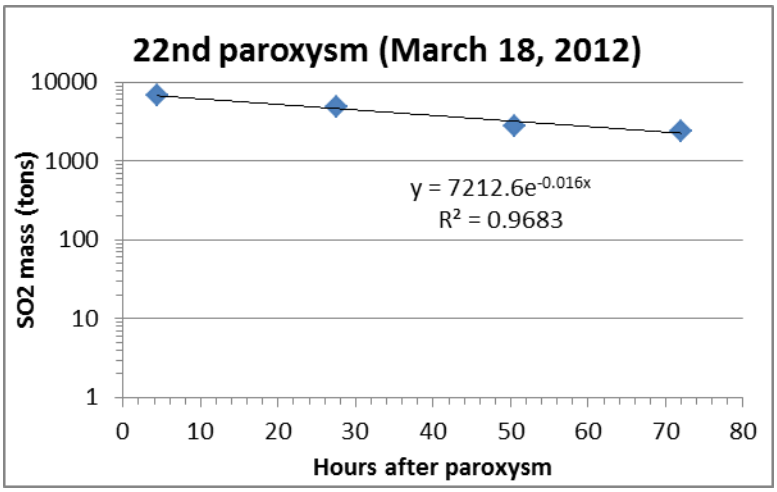

Figure 4.10: Graph of OMI SO_2 mass against time for the 22nd paroxysm. The exponential decay regression line with the equation is shown as well as the correlation coefficient.

25th paroxysm (April 24, 2012): This paroxysm started early in the evening of April 24. Lava fountains generated a volcanic cloud that rose up to 11 km altitude and drifted South East of Etna. About 3.5 days after the onset of the eruption, low SO_2 column amounts (2 DU) are visible in OMI data at the border of Iran and Turkmenistan. In Figures 4.11 and 4.12, we can see for the 2 first images taken by OMI and AIRS about 15 min apart, the SO_2 cloud is in about the same location but AIRS measures higher SO_2 columns and shows lower plume dispersion (similar to the example of the 21st paroxysm). The higher SO_2 columns measured by AIRS are surprising because they should be lower, if the sensitivity is lower. This may arise from a problem with the AIRS SO_2 algorithm that produces some anomalous AIRS pixels (where the retrieval failed) perhaps due to cloud interference. For the corresponding images, the SO_2 mass from AIRS is approximately double that measured by OMI, although the plume is estimated to be at 7.3 km and then 11 km altitude respectively. Furthermore, it is possible to estimate the plume linear velocity based on the observed distance travelled by the SO_2 in sequential images. A good estimation of the cloud dispersion is 13 m/s.

The SO_2 burden retrieval for this paroxysm from OMI has a robust correlation coefficient (R^2=0.99) and yields a corrected mass at the onset of the eruption of 12050 tons, as shown in figure 4.13. For AIRS, the corrected mass is 28110 tons with a R^2=0.90 which is quite good but lower than using OMI. The observed differences between OMI and AIRS provided motivation for more detailed pixel-by-pixel comparisons between the retrievals, as discussed in the next section.

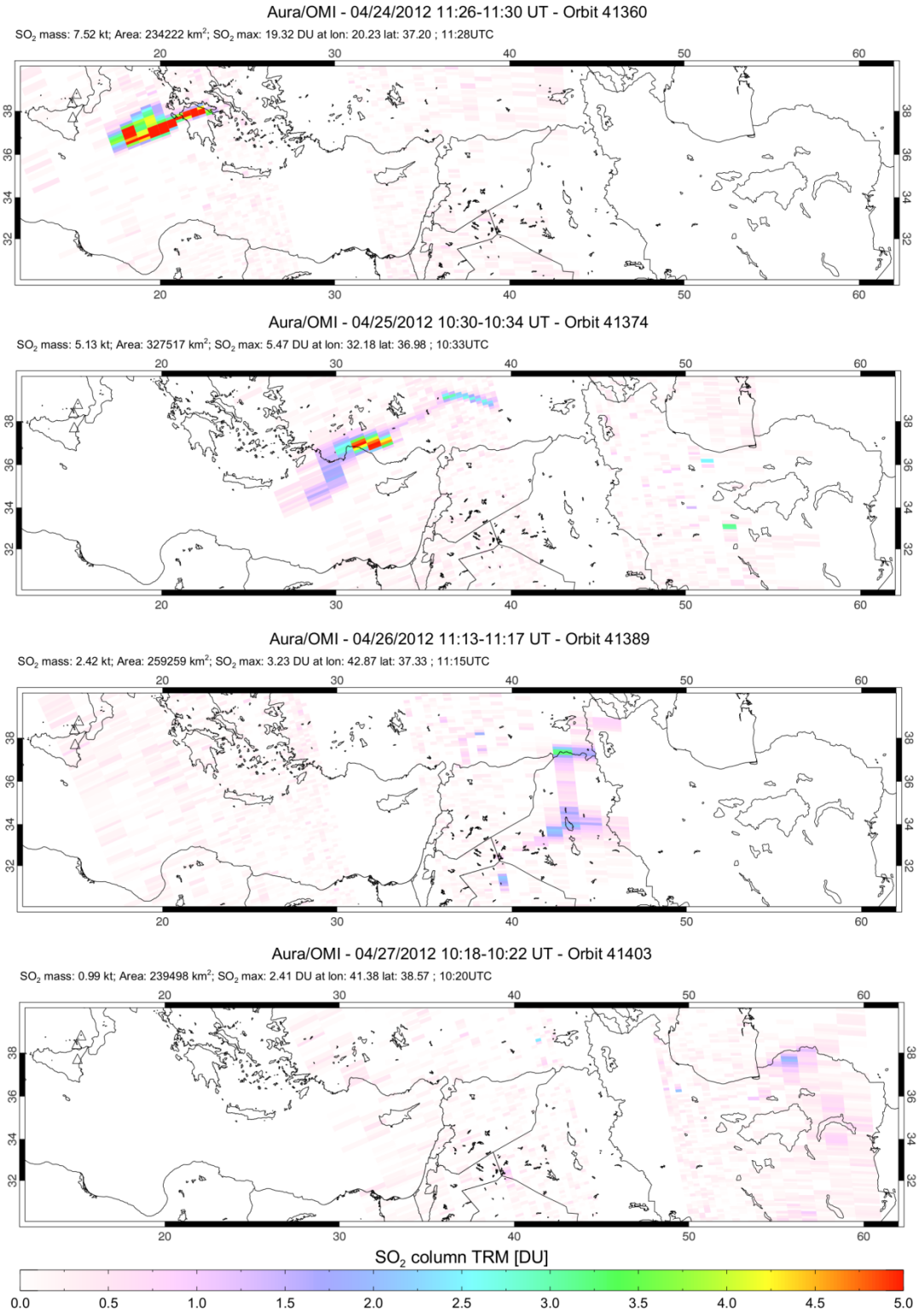

Figure 4.11: OMI images of the SO_2 cloud from the 25th paroxysm of the NSEC.

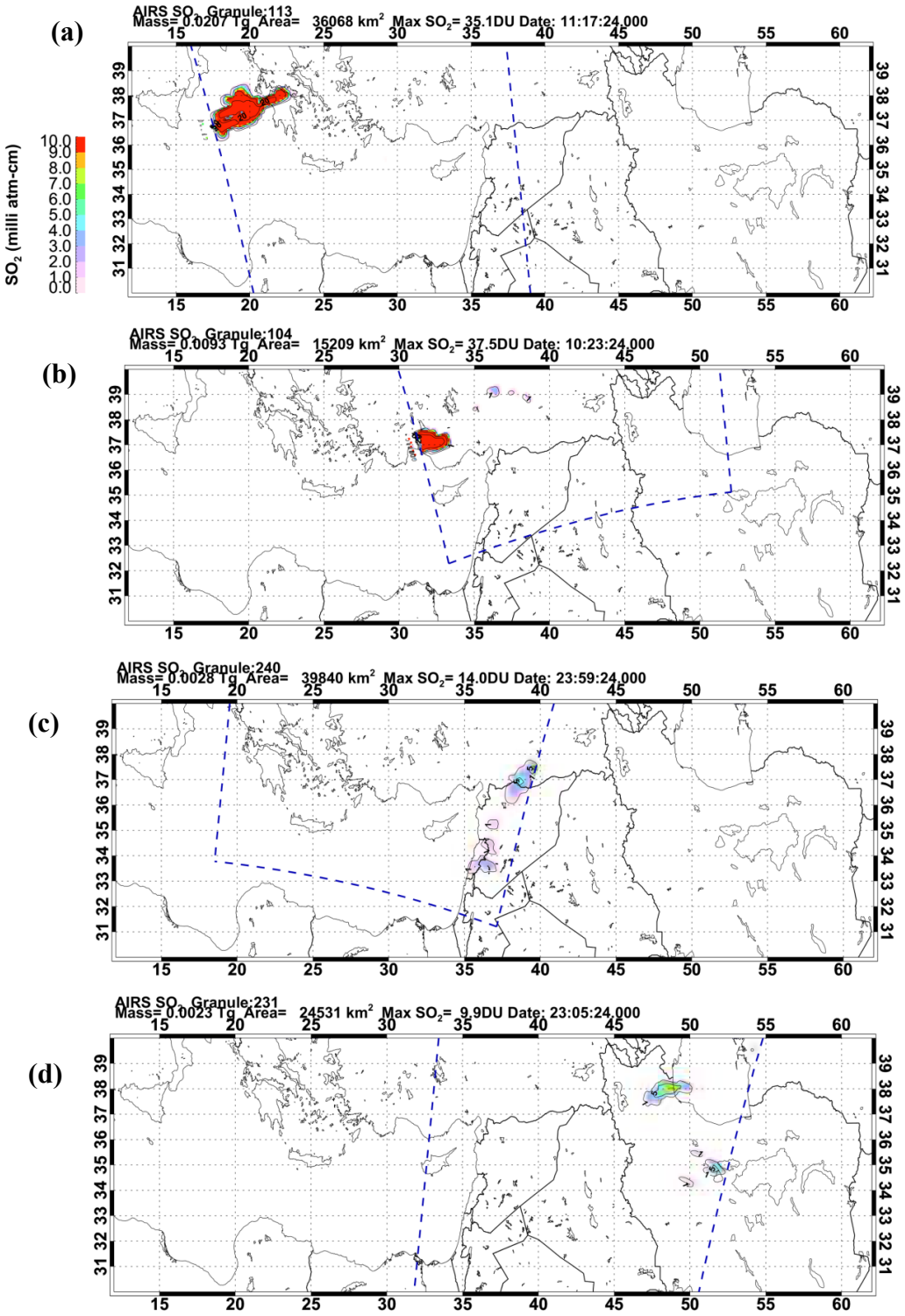

Figure 4.12: AIRS measurements of the SO2 plume from the 25th paroxysm. (a) overpass at 11:17 UT on April 24, 2012; (b) overpass at 10:23 UT on April 25; (c) overpass at 23:59 UT on April 25; (d) overpass at 23:05UT on April 26; with (a) and (b) corresponding to the OMI overpass.

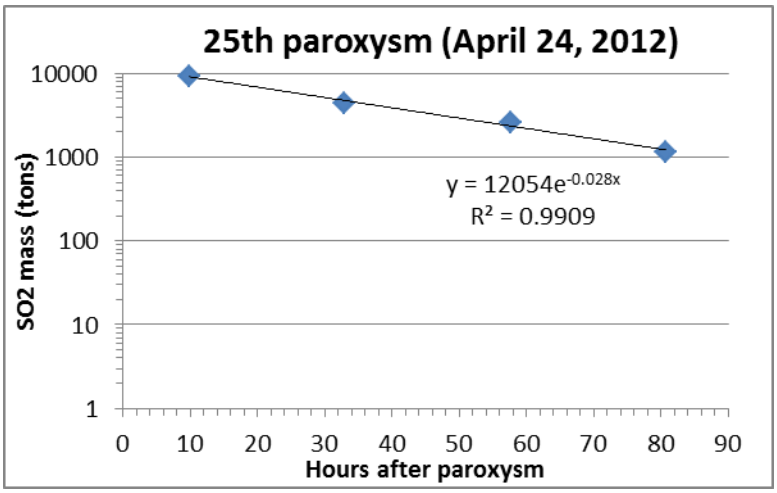

Figure 4.13: Graph of OMI SO_2 mass data from the 25th paroxysm. The exponential decay regression line with the equation is shown as well as the correlation coefficient.

A summary of all the SO_2 loadings calculated for each paroxysm from OMI and AIRS is shown in Table 4.1. Only one event, on October 8, 2011, could not be processed from either of the 2 instruments to estimate the SO_2 mass because it experienced the cloudiest conditions and the HYSPLIT model does not show a trajectory that fit Etna (no AIRS data and OMI was affected by the row anomaly). The plume altitudes are indicated only for the OMI observations and were determined using HYSPLIT. It is important to constrain the altitude of the volcanic cloud since it is a proxy for eruption intensity; the following equation established by Wilson et al. (1978) is showing this relationship:

$H = 0.236\, M_f{}^{1/4}$ where H is the plume height (in km) and M_f is the mass flux (in kg/s).

Use of multiple consecutive SO_2 images allows us to constrain the SO_2 loss rate in the drifting volcanic clouds after emission from the lava fountains. In some cases, events were only detected on one image, which does not permit estimation of the decay rate and the corrected SO_2 mass at the onset of the paroxysm. Therefore, in such cases we explored different extrapolations (e.g., average exponential decay rate and plume height; see section 3.4) to estimate the initial SO_2 mass released (italicized values in Tale 4.1 indicate the best estimates). When more than one image was available, we used the

exponential decay rate derived for the specific paroxysm (in this case we report only one number Table 4.1). Since neither OMI nor AIRS gives direct information on the plume altitude, we also looked at CALIPSO data to have more information but none of the plumes were detected. This might be due to the generally small size of Etna's plume and the satellite is therefore missing it. In Table 4.1, the SO_2 mass retrievals for each paroxysm are shown, and the data in italics corresponds to the initial SO2 mass that we used in the next section 4.4 (plume height extrapolation with OMI and average decay with AIRS).

Table 4.1: SO2 mass retrievals from OMI and AIRS instruments for all the 25 paroxysms from Etna's NSEC during the 2011-2012 cycle.

paroxysm number	date paroxysm	Paroxism phase (radar) UTC	Paroxysm duration (min)	repose time (days)	date images	acquisition time	plume height (km)	SO2 cloud mass calculation (tons)	hours since start of paroxysm	corrected SO2 mass **OMI**-exponential (tons)	corrected SO2 mass **OMI**-height (tons)	corrected SO2 mass **AIRS**-exponential (tons)	images (OMI/ AIRS)	corrected SO2 mass **OMI-AIRS** combined (tons)
1	01/12/11	21:50-23:21	91	60	01/13/11	1:29		7000	3.7			9880	AIRS	
					01/13/11	12:29		3900	14.7				AIRS	
					01/14/11	0:29		1300	26.7				AIRS	
2	02/18/11	07:20-10:50	210	36	02/18/11	11:59		600	4.7			750	AIRS	
					02/18/11	12:12	8	3390	4.9	*3390*			OMI	
					02/19/11	11:05		200	23.1				AIRS	
					02/19/11	11:17	3	3340	27.9				OMI	
3	04/10/11	10:48-12:37	109	51	04/10/11	12:35		3000	1.8			*3370*	AIRS	2360
					04/10/11	12:42	4	1970	1.9	2010	*2020*		OMI	
					04/11/11	0:35		3300	13.8				AIRS	
					04/11/11	11:41		3900	24.9				AIRS	
4	05/12/11	01:50-03:20	90	30	05/12/11	12:42	7.5	1150	10.9	1670	*1570*		OMI	
5	07/09/11	14:03-15:14	71	58	07/10/11	1:11		300	11.1			3710	AIRS	
					07/10/11	12:11		30	22.1				AIRS	
					07/10/11	12:26	6.5	2670	22.4	5710	*4370*		OMI	
6	07/19/11	00:00-02:30	150	9.5	07/19/11	12:05		300	12.1			*670*	AIRS	
					07/20/11	11:23	4.5	1650	35.4	5510	*8420*		OMI	
7	07/25/11	04:00-05:30	90	6	07/25/11	11:29		200	7.5			*330*	AIRS	
					07/25/11	11:40	7	2930	7.7	3800	*3440*		OMI	
8	07/30/11	19:35-21:15	100	5	07/31/11	10:53		700	15.3			*1920*	AIRS	
					07/31/11	11:05	6	4970	15.5	*12570*			OMI	
					08/01/11	10:13	4.8	1240	38.6				OMI	
9	08/05/11	21:55-23:10	75	6	08/06/11	0:47		3700	2.9			*4470*	AIRS	*4400*
					08/06/11	11:53		3800	14.0				AIRS	
					08/07/11	11:10	10	2830	37.3	6430			OMI	
					08/08/11	10:16	7.7	2780	60.4				OMI	
					08/09/11	10:59	6.1	1190	85.1				OMI	
10	08/12/11	08:50-10:05	117	7	08/12/11	11:29	2.5	3220	2.7	*3430*			OMI	
					08/13/11	0:59		5600	16.2			29190	AIRS	
					08/13/11	11:59		1600	27.2				AIRS	
					08/13/11	12:11	6.5	2540	27.4				OMI	
					08/14/11	0:05		500	39.3				AIRS	
					08/14/11	11:19	3	1720	50.5				OMI	
11	08/20/11	07:10-07:35	25	8	08/20/11	12:05		6200	4.9			9310	AIRS	
					08/20/11	12:17	10	3560	5.1	*5530*			OMI	
					08/21/11	1:47		6700	18.6				AIRS	

Table 4.1 continued

				08/21/11	12:47		2100	29.6				AIRS	
				08/21/11	13:02	9	420	29.9				OMI	
12	08/29/11 04:10-04:45	35	9	08/29/11	12:00		3200	7.8			4210	AIRS	*4230*
				08/30/11	0:00		2100	19.8				AIRS	
				08/30/11	11:16	4.5	2400	31.1	9950			OMI	
				08/31/11	11:59	4	770	55.8				OMI	
13	09/08/11 07:31-08:17	46	10	09/08/11	12:35		9000	5.1			11940	AIRS	5610
				09/09/11	0:35		2300	17.1				AIRS	
				09/09/11	11:41		1400	28.2				AIRS	
				09/09/11	11:53	6.5	3790	28.4	*7020*			OMI	
				09/10/11	12:35	6.5	2210	53.1				OMI	
14	09/19/11 12:30-12:50	20	11	09/20/11	11:38	9.5	1340	23.1	2930	*9770*		OMI	
15	09/28/11 19:33-19:55	22	9.5	09/29/11	0:11		3500	4.6			*4750*	AIRS	
				09/29/11	11:17		7700	15.7				AIRS	
				09/29/11	11:31	10	3080	16.0	5300	*8700*		OMI	
16	10/08/11 14:45-15:10	25	10	10/09/11				anomaly					
17	10/23/11 18:45-20:15	90	15	10/24/11	11:23	5.5	2270	16.6	4000	*6170*		OMI	
18	11/15/11 11:20-12:25	65	23	11/16/11	0:12		4800	12.9			*11210*	AIRS	21560
				11/16/11	9:50	9	1560	22.5	2490	*1860*		OMI	
19	01/05/12 05:45-06:45	60	50	01/05/12	12:41		19800	6.9			37160	AIRS	30300
				01/06/12	0:47		6600	19.0				AIRS	
				01/06/12	10:20	7.5	4280	28.6	11310	*8030*		OMI	
20	02/09/12 01:00-06:00	300	35	02/09/12	11:35		1000	10.6			*2010*	AIRS	
				09/02/12	11:47	5	2620	10.8	3780	*5010*		OMI	
21	03/04/12 07:30-09:30	120	23	**03/04/12**	**12:23**		**7500**	**4.9**			**5170**	**AIRS**	6650
				03/04/12	**12:37**	**7**	**9920**	**5.1**	***9860***			**OMI**	
				03/05/12	0:23		6900	16.9				AIRS	
				03/05/12	11:29		1400	28.0				AIRS	
				03/05/12	11:42	8.4	4340	28.2				OMI	
				06/03/12	8:53		2600	49.4				AIRS	
				03/06/12	9:07	9.8	3960	49.6				OMI	
				06/03/12	20:53		6300	61.4				AIRS	
22	03/18/12 08:25-09:40	75	14	**03/18/12**	**12:35**		**10300**	**4.2**			**14220**	**AIRS**	10290
				03/18/12	**12:48**	**9.5**	**6830**	**4.4**	***7210***			**OMI**	
				03/19/12	**11:41**		**8800**	**27.3**				**AIRS**	
				03/19/12	**11:54**	**11.2**	**4790**	**27.5**				**OMI**	
				03/19/12	23:41		5100	39.3				AIRS	
				03/20/12	10:47		4700	50.4				AIRS	
				03/20/12	10:58	10.2	2820	50.5				OMI	
				03/20/12	22:47		2700	62.4				AIRS	
				03/21/12	8:11		1800	71.8				AIRS	

Table 4.1 continued

				03/21/12	8:24	10.8	2420	72.0			OMI		
23	04/01/12 02:41-03:35	54	14	04/01/12	11:11		6700	8.5			7130	AIRS	7910
				04/01/12	11:23	10.5	7410	8.7	*12990*			OMI	
				04/02/12	10:11		3000	31.5				AIRS	
				04/02/12	10:29	9	1660	31.8				OMI	
				04/02/12	22:17		3800	43.6				AIRS	
24	04/12/12 14:32-15:10	38	10.5	04/13/12	0:35		200	10.1			*390*	AIRS	
				04/13/12	11:50	8.8	2670	21.3	*5500*	4170		OMI	
25	04/24/12 01:35-02:15	40	11.5	**04/24/12**	**11:17**		**20700**	**9.7**			**28110**	**AIRS**	18580
				04/24/12	**11:30**	**7.3**	**9100**	**9.9**	***12050***			**OMI**	
				04/25/12	10:23		9300	32.8				AIRS	
				04/25/12	10:34	11	4470	33.0				OMI	
				04/25/12	23:59		2800	46.4				AIRS	
				04/26/12	11:20	9	2640	57.7				OMI	
				04/26/12	23:05		2300	69.5				AIRS	
				04/27/12	10:22	10	1150	80.8				OMI	

In Table 4.2, we summarize all the exponential decay coefficients derived from both OMI and AIRS measurements. We note that the exponential decay rate from either instrument does not show an obvious dependence on the season of the year, or on the plume altitude. Furthermore, the coefficient of correlation R^2 is given only when we have more than 2 points.

Table 4.2: Summary of the SO_2 mass exponential decay rate for each paroxysm with 2 or more data points.

Paroxysm number	date	corrected SO2 mass	Exponential decay rate	R^2	
1	01/12/11	9880	-0.073		AIRS
2	02/18/11	3390	-0.0006		OMI
		750	-0.048		AIRS
5	07/09/11	3710	-0.226		AIRS
8	07/30/11	12565	-0.06		OMI
9	08/05/11	6430	-0.018	0.7824	OMI
		3670	0.0024		AIRS
		4400	-0.013	0.8129	combined
10	08/12/11	3430	-0.013	0.9765	OMI
		29190	-0.104	0.9976	AIRS
11	08/20/11	5530	-0.086		OMI
		9310	-0.042	0.6372	AIRS
12	08/29/11	9950	-0.046		OMI
		4210	-0.035		AIRS
		4230	-0.028	0.8826	combined
13	09/08/11	7020	-0.022		OMI
		11940	-0.081	0.9432	AIRS
19	01/05/12	37160	-0.091		AIRS
21	03/04/12	9860	-0.021	0.84	OMI
		5170	-0.007	0.0495	AIRS
22	03/18/12	7210	-0.016	0.9683	OMI
		14220	-0.026	0.9193	AIRS
23	04/01/12	12990	-0.065		OMI
		7130	-0.019	0.6467	AIRS
25	04/24/12	12050	-0.028	0.9909	OMI
		28110	-0.039	0.8994	AIRS

4.3 OMI-AIRS validation

The large number of Etna's SO_2 clouds detected by both OMI and AIRS provide a good opportunity for comparison and validation of the UV and IR SO_2 retrievals. We compared the OMI SO_2 data and the AIRS SO_2 data pixel by pixel (section 3.5) for each case with near-coincident OMI and AIRS measurements in the A-Train. Out of a total of 23 cases used to test the validation of AIRS with OMI, 7 days give a good correlation between the 2 techniques ($R^2 \geq 0.5$) with 4 of these days being in our best paroxysms (i.e. Table 4.1 in bold font).

The first day of the 21st paroxysm (March 3, 2012) shows good agreement between the 2 methods at 0.2° distance from each OMI pixel. Figure 4.14 shows, as expected, that the correlation coefficient increases with distance from OMI pixel from 0.80 at 0.2° to 0.98 at 0.5°, using data points with OMI $SO_2 \geq 5$ DU (see section 3.5). The same trend can be seen when using a threshold of 10 DU instead (Figure 4.15) with R^2 increasing from 0.83 at 0.2° to 0.97 at 0.5°. We observe a difference between the correlation coefficients when we change the number of data points included in the linear regression. On this day, the total SO_2 mass measured by AIRS was lower than OMI, and Figures 4.15 shows that the AIRS SO_2 columns were indeed lower than OMI for the larger SO2 column amounts. It is important to note that the data are color coded according to OMI cross-track scan position, with dark blue corresponding to off-nadir positions; comparisons between AIRS and OMI are expected to be less robust for off-nadir pixels.

For the case of the 22nd paroxysm, it was possible to compare AIRS and OMI on more than one day; March 18 and 19, 2012 respectively. However, it was possible to find good agreement between the 2 methods only when using data points with OMI $SO_2 \geq 1$ DU, the correlation for higher SO_2 column amounts was not good enough. As shown in Figure 4.16, the correlation coefficient for March 18 is 0.66 and for the next day it is higher with 0.87. This can be explain by looking at the OMI pixel position, since we have more points close to nadir on March 19 (light green to yellow) than on March 18, the 2

instruments have more similar measurements. Since AIRS retrievals are more sensitive to SO_2 altitude than OMI, another possible explanation for retrieval differences is the altitude of the plume, which was on March 19 (9.5 km altitude on March 18 and 11.2 km on the following day).

The example of the first day of the last paroxysm of the cycle (April 24, 2012) shows a better correlation between OMI and AIRS considering data points with OMI $SO_2 \geq 5$ DU, as shown in Figures 4.17 and 4.18. Indeed, we don't have a good agreement at 0.4° for 1 DU which is not the case for 5 DU with a $R^2 = 0.68$. As for the 21st paroxysm, the correlation coefficient increases with distance from the OMI pixels. For a 1 DU threshold, at 0.4° distance the correlation is poor ($R^2 < 0.5$) whereas and at 0.5° the correlation coefficient increases to 0.69. For a 5 DU threshold, at 0.4° R^2=0.68 and then at 0.5° it increases to 0.90. The OMI cross-track pixel positions in these cases (Figures 4.17 and 4.18) are off nadir (positions 42 to 54) but we still find a good correlation between OMI and AIRS measurements. This implies a relatively homogenous SO_2 cloud with similar column amounts present over large areas.

We conclude that AIRS SO_2 retrievals can be validated using OMI SO_2 retrievals but that pixel-by-pixel comparisons require particular conditions. SO_2 cloud homogeneity, altitude and meteorological cloud conditions are probably the key factors. We found the best correlation for high altitude SO_2 clouds as suggested by Prata and Bernardo (2007). Therefore, it is good to use AIRS data to better constrain the plume altitude and track the cloud when OMI images are lacking but quantitative estimation of the SO_2 burdens is more reliable using OMI measurements in all cases and especially for low altitude clouds.

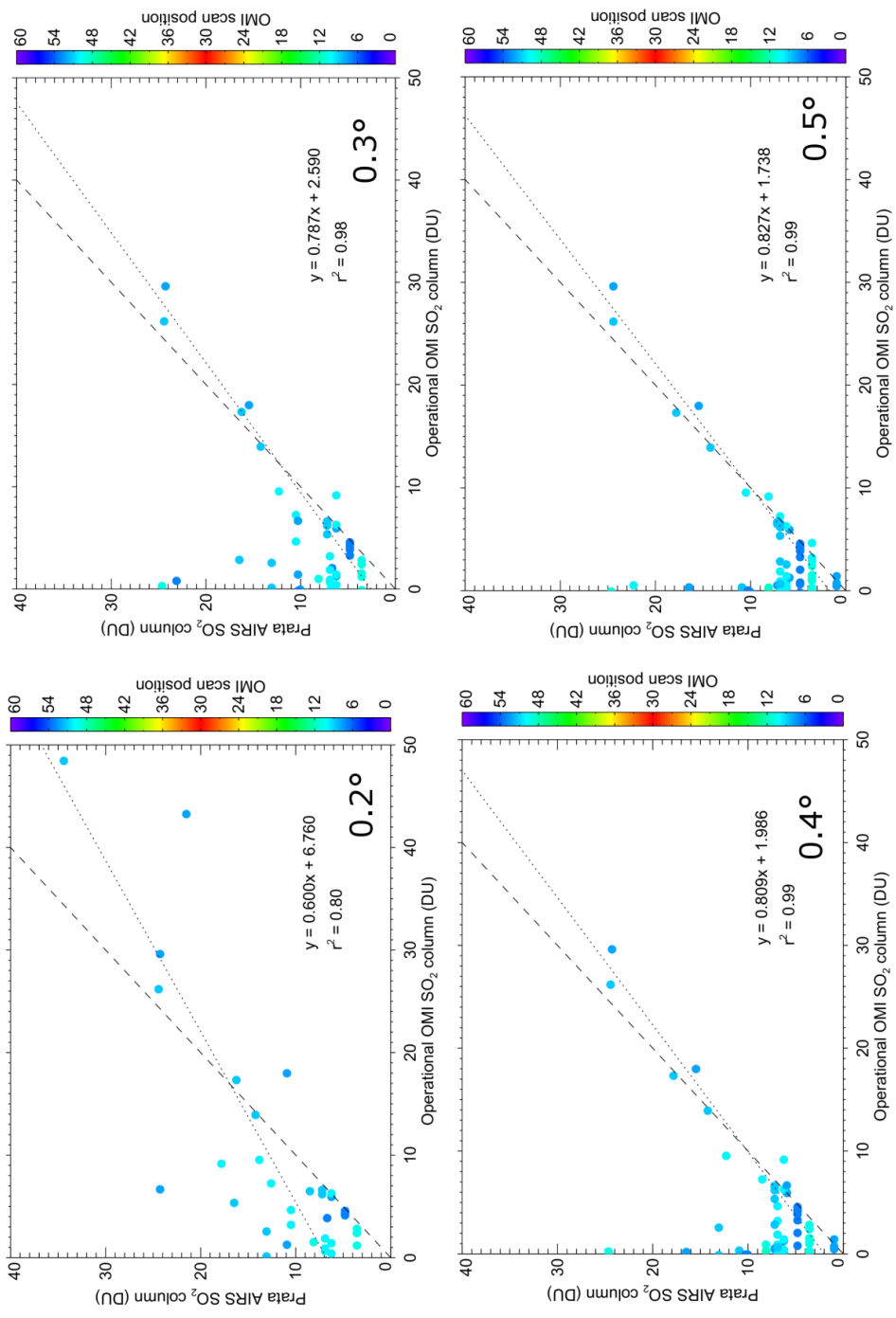

Figure 4.14: Graphs showing the correlation between OMI SO_2 data and AIRS SO_2 data from the 4th of March 2012 for different distances from OMI pixels and data points with OMI $SO_2 \geq 5$ DU. On each plot, the dashed line is the 1:1 line, and the dotted line is the best-fit linear regression line.

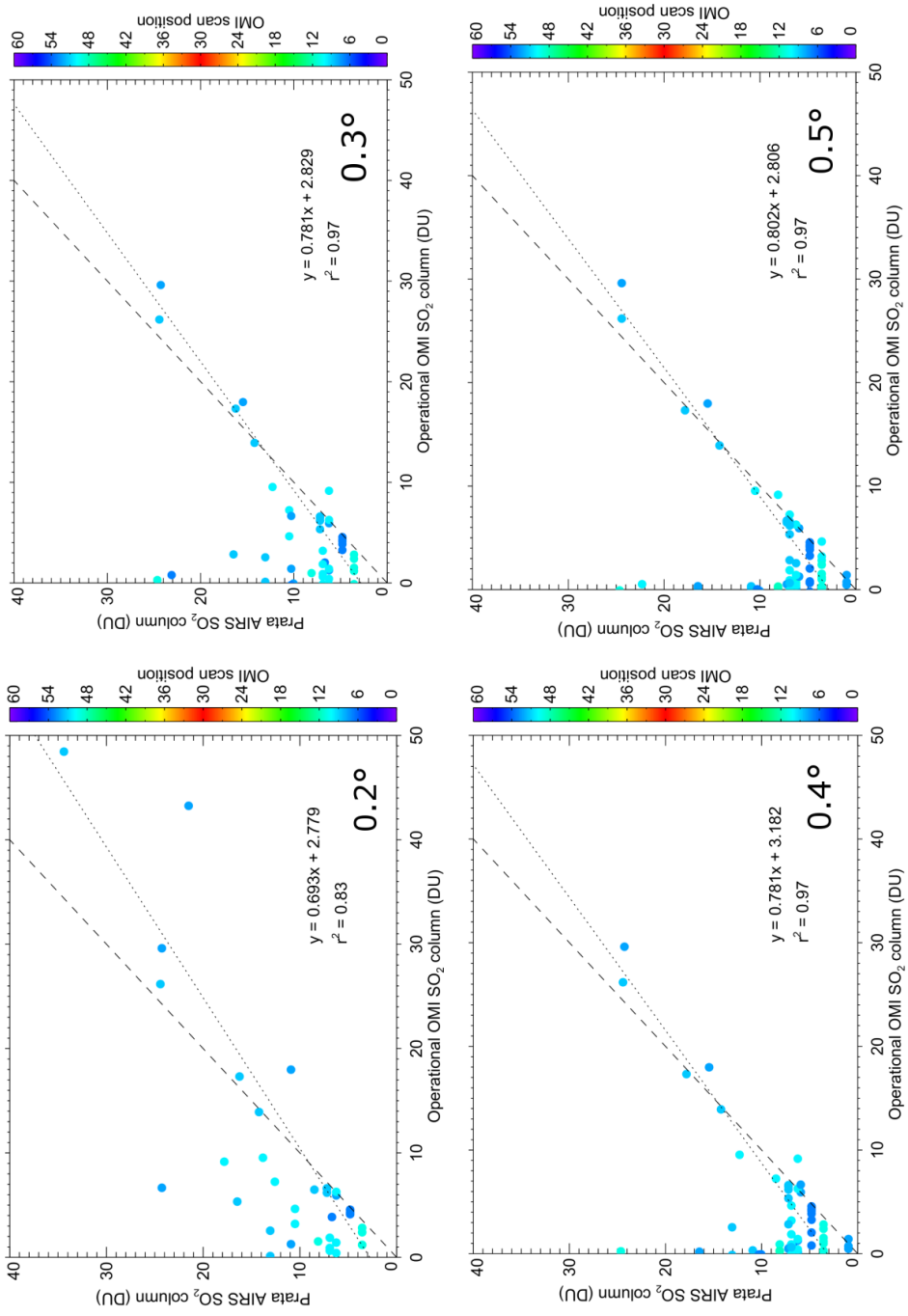

Figure 4.15: Graphs showing the correlation between OMI SO_2 data and AIRS SO_2 data from the 4th of March 2012 for different distances from OMI pixels and data points with OMI $SO_2 \geq 10$ DU. On each plot, the dashed line is the 1:1 line, and the dotted line is the best-fit linear regression line.

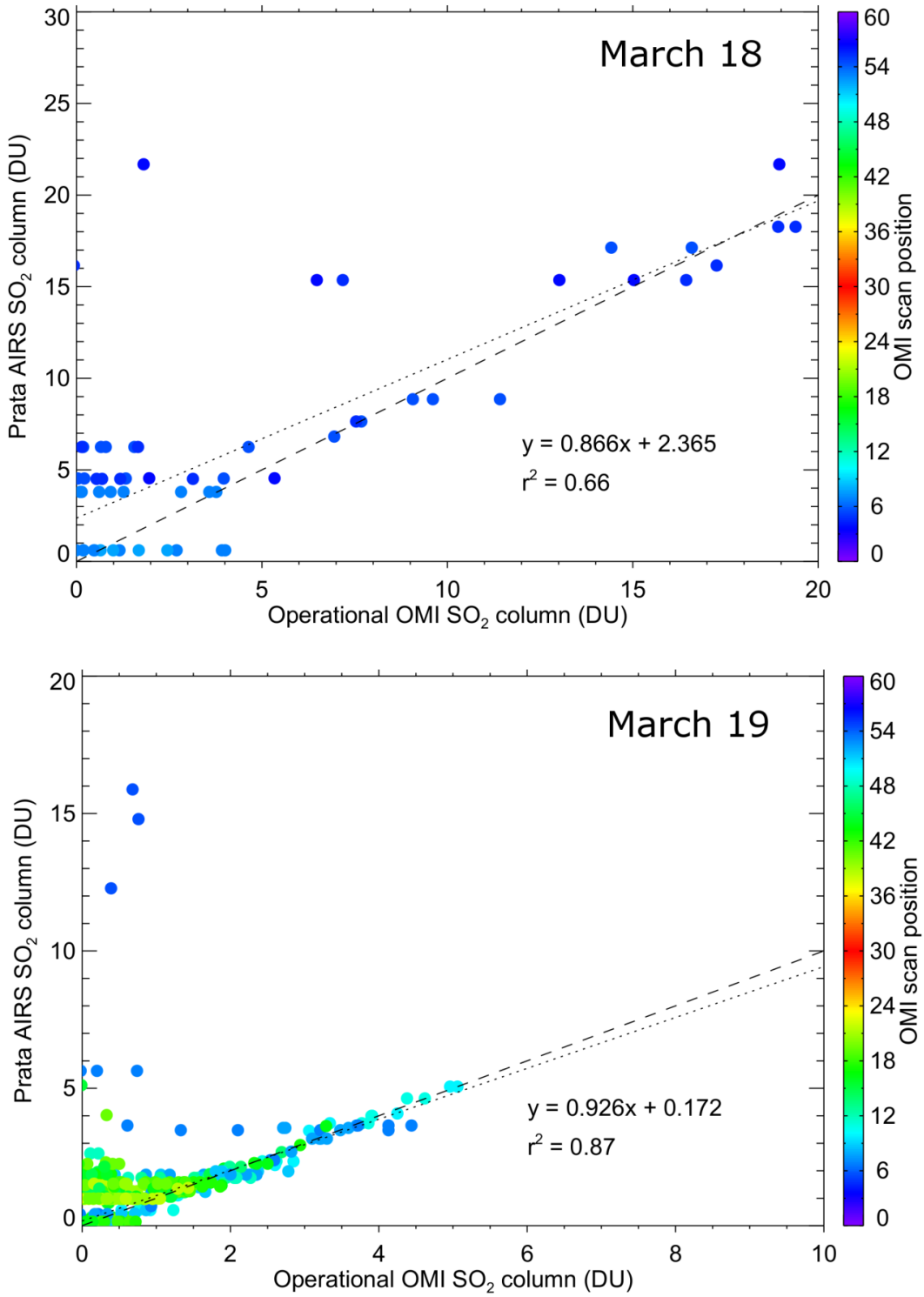

Figure 4.16: OMI AIRS validation for 0.5° with 1 DU threshold from the 22nd paroxysm and the 2 first days of cloud tracking. On each plot, the dashed line is the 1:1 line, and the dotted line is the best-fit linear regression line.

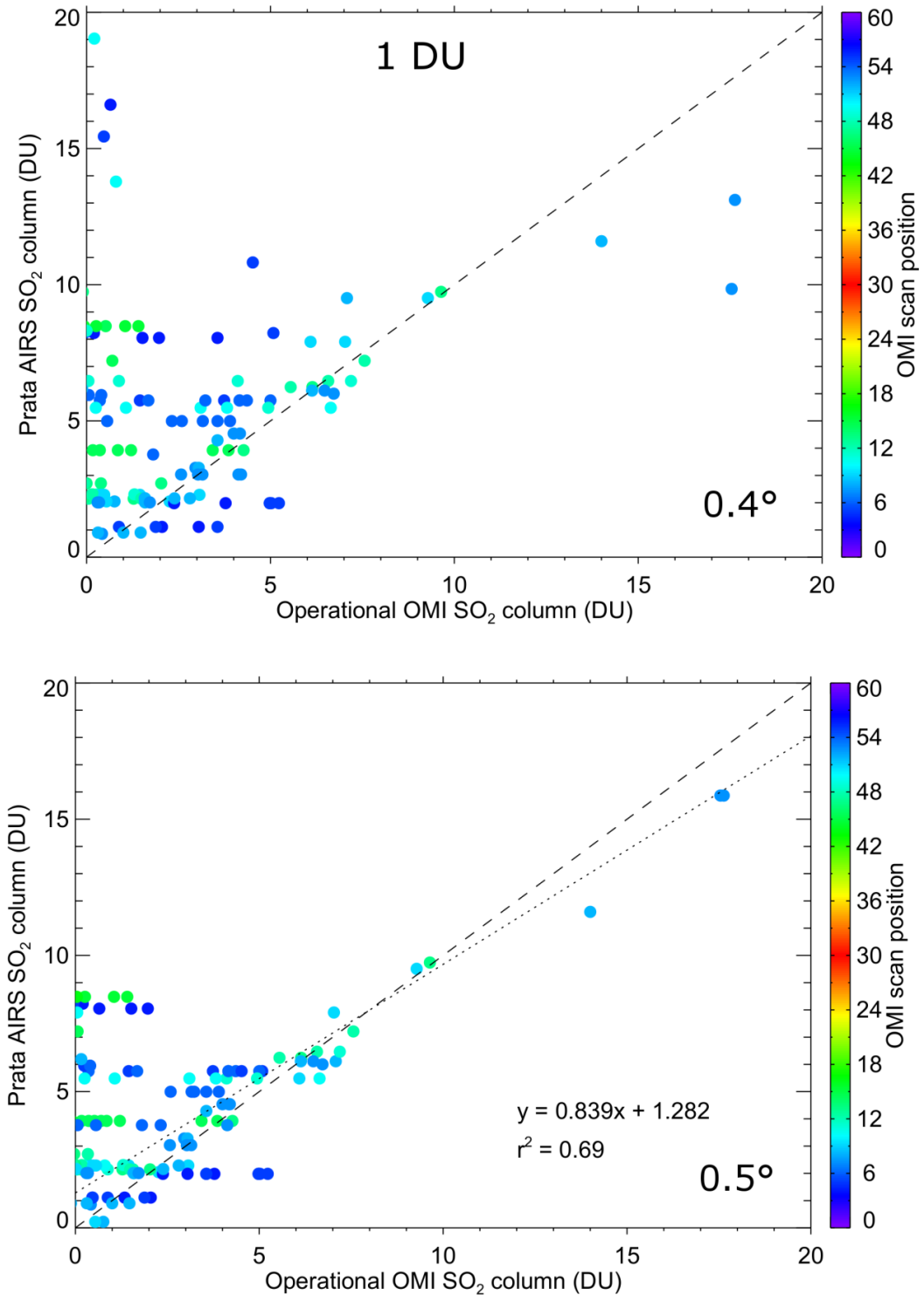

Figure 4.17: OMI AIRS validation for 0.5° and 0.4° with 1 DU limit from the 25th paroxysm (April 24, 2012). On each plot, the dashed line is the 1:1 line, and the dotted line is the best-fit linear regression line.

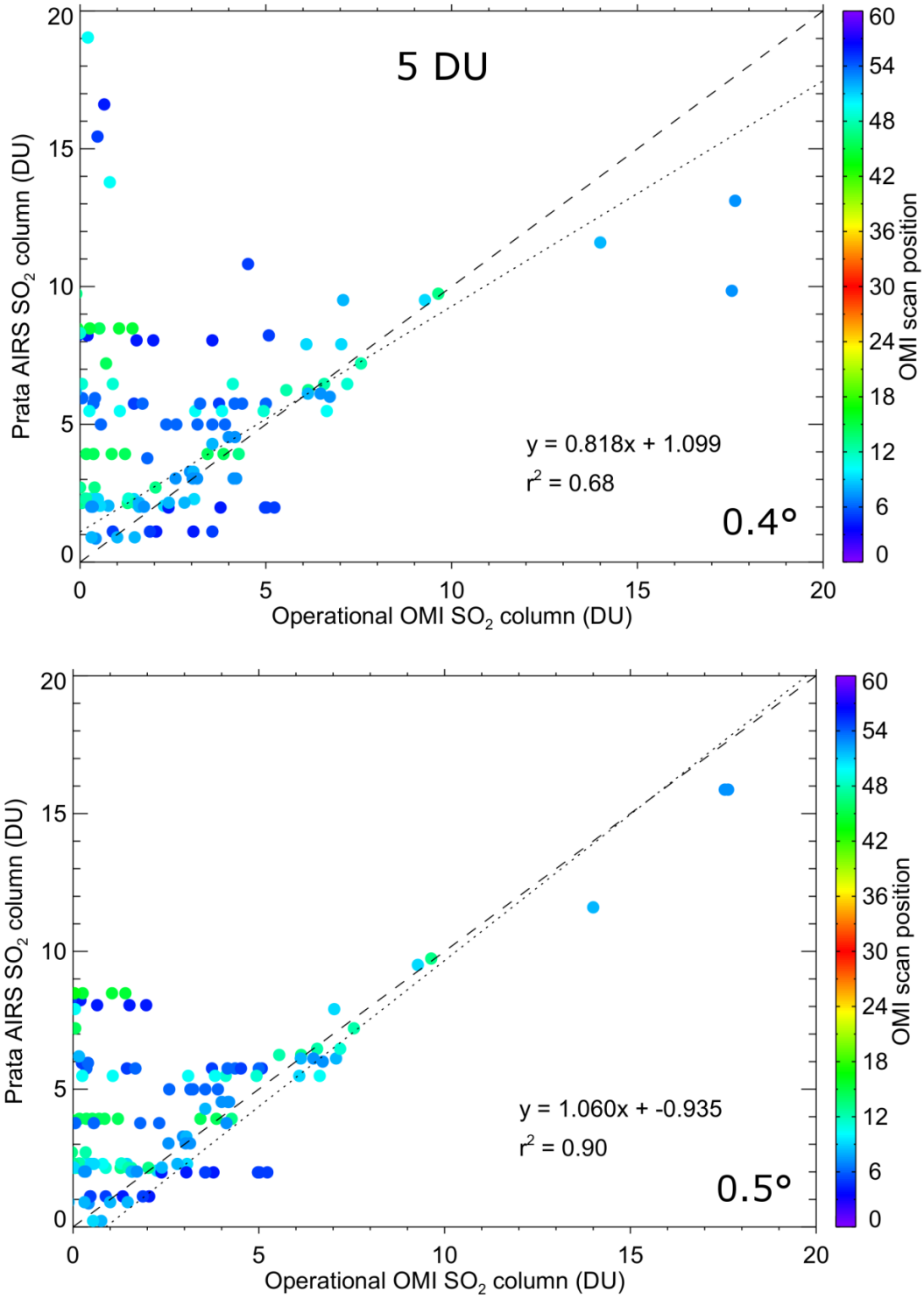

Figure 4.18: OMI AIRS validation for 0.5° and 0.4° with 5 DU limit from the 25th paroxysm (April 24, 2012). On each plot, the dashed line is the 1:1 line, and the dotted line is the best-fit linear regression line.

4.4 Driving mechanism for lava fountains

Two different models have been suggested to explain the mechanism of explosive basaltic eruptions (Parfitt, 2004): the Rise Speed Dependent (RSD) model and the Collapsing Foam (CF) model. The RSD model states that the type of explosive activity depends mainly on the rise speed of the magma ascending to the surface. The magma contains dissolved volatiles (i.e., H_2O, SO_2, and CO_2) at depth, but as it rises, the gases exsolves and creates homogeneous two phase flow. In this model, it is assumed that the rise speed of the magma is sufficiently fast that the bubbles cannot rise far relative to the magma and therefore the bubbles are considered locked in the magma (Parfitt, 2004). The explosive activity results, in this case, from the fragmentation of fast-rising bubbly melt (Bonaccorso et al., 2011) due to decompression and expansion of the gas while accelerating as it rises. The CF model proposes an alternative driving mechanism. This model considers a separate two-phase flow where the magma and bubbles behave differently (Parfitt, 2004). This model was developed by Jaupart and Vergniolle, (1988, 1989) and assumes that the magma is stored at depth, where volatiles exsolve and bubbles rise to the top of the storage area to form a foam layer. When bubbles are closely packed together and the layer reaches a critical thickness, the foam collapses and ascends the conduit to drive a lava fountain (Parfitt, 2004). Strombolian eruptions are also linked with this type of behavior where repeated partial foam collapse forms small gas pockets that ascend the conduit as a slug flow before bursting at the surface (Figure 4.20). However, if the viscosity of the magma is low, then a single gas pocket surrounded by liquid can form, this behavior is called annular flow and is linked with Hawaiian eruptions (Parfitt, 2004).

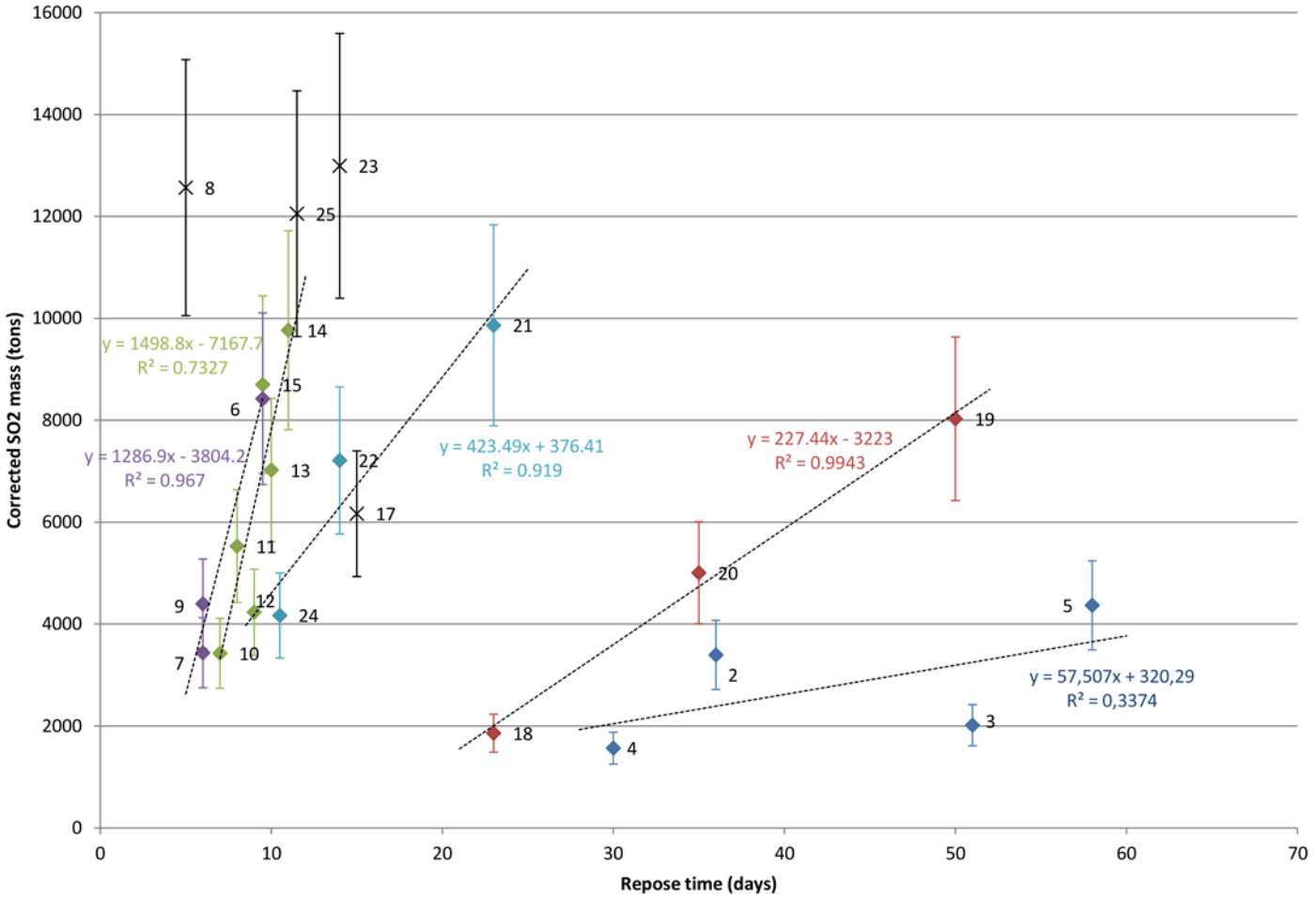

Figure 4.19: Graph of the SO_2 mass against inter-paroxysm repose time using OMI data with extrapolated values (plume height and combined extrapolation). Paroxysm number is indicated next to the data points and 20% error is assumed on the SO_2 mass.

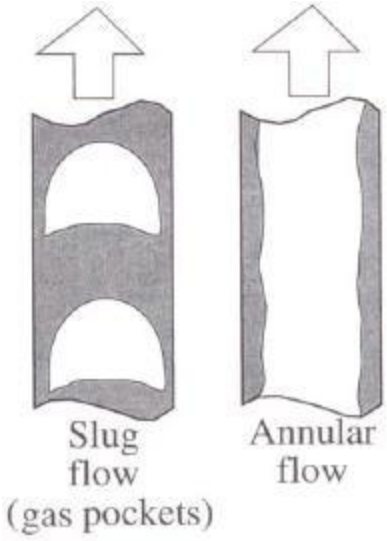

Figure 4.20: Schematic diagram showing two examples of separated, two-phase flow: slug and annular flow, adapted from Vergniolle and Jaupart, 1986.

Etna's frequent paroxysms, particularly since January 2011, provide an opportunity to improve understanding of the driving mechanism of lava fountains. They have therefore been studied by many authors and using many different approaches such as volcanic tremor (Alparone et al., 2003), geochemical analysis (Allard et al., 2005), analysis of erupted products (Andronico and Corsaro, 2011) as well as multidisciplinary studies (Aiuppa et al., 2010; Bonaccorso et al., 2011). Whilst other studies have generally investigated the driving mechanism of Etnean lava fountains for individual eruptive events (e.g., Allard et al., 2005; Bonaccorso et al., 2011; Calvari et al., 2011), our dataset provides information on SO_2 emissions for an entire sequence of paroxysms. Bonaccorso et al. (2011) studied the case of the 10 April 2011 eruption and they suggest that the lava fountains was driven by a separated two-phase flow that accumulated at the top of a shallow magma storage region at about 2 km a.s.l (Vergniolle and Ripepe, 2008; Allard et al., 2005; Bonaccorso et al., 2011b), which supports the CF model.

Using our satellite-derived SO_2 burdens corrected for emission time, the accurate timing of the lava fountains by the OPGC VOLDORAD 2B, as well as the inter-paroxysm repose time, we find a correlation exists between SO_2 emissions and repose time (Fig. 4.19). As shown in Figure 4.19, the SO_2 mass for each paroxysm retrieved from OMI

measurements seems to increase with the repose time, but with distinct trends for different sequences of paroxysms, e.g., 18-20-19 or 10-12-11-13-15-14. These trends could represent different rates of gas accumulation in the magma storage region, influenced by changing plumbing system geometry and/or rates of fresh magma supply. This relationship between the mass of SO_2 emitted and the inter-paroxysm repose time supports the CF model for lava fountains at Etna, since it is consistent with a model of progressive gas accumulation over time, with longer repose times resulting in the release of large amounts of stored gas.

In this study, we also used the corrected SO_2 mass based on AIRS SO_2 data with the inter-paroxysm repose time to see if the same correlation is observed. Figure 4.21 shows the same correlation but since the mass retrieval from AIRS is generally less precise it is less clear than in the OMI data (accuracy of about 6 DU, Prata and Bernardo, 2007). The study of the SO_2 emitted by Etna's NSEC during each lava fountain episodes (paroxysm) was carried out to try to better understand their driving mechanism and identify the right model. We suggest that our data tend to be in agreement with the CF model of Jaupart and Vergniolle (1989).

We also used the corrected SO_2 burdens to check for any correlation with the duration of each paroxysm estimated using VOLDORAD 2B, which might be expected for gas-driven lava fountains. In Figure 4.22, we present data from both techniques (OMI and AIRS). While there is no clear overall relationship between the amount of SO2 emitted and the duration of the paroxysm, clusters of events do appear to show a relationship. OMI SO_2 burdens seem to show a broad correlation with paroxysm duration. However, a drawback of our dataset is that it accounts for only one volatile species (SO_2), whereas CO_2 and H_2O likely also play a role in driving lava fountains. Hence different trends in the data in Figs. 4.19, 4.21, and 4.22 could indicate accumulation and release of stored gas with variable SO_2/CO_2 and SO_2/H_2O. With this data set, it is therefore hard to make a definitive conclusion on the driving mechanism of lava fountains at Etna's NSEC, although in general the CF model appears more appropriate.

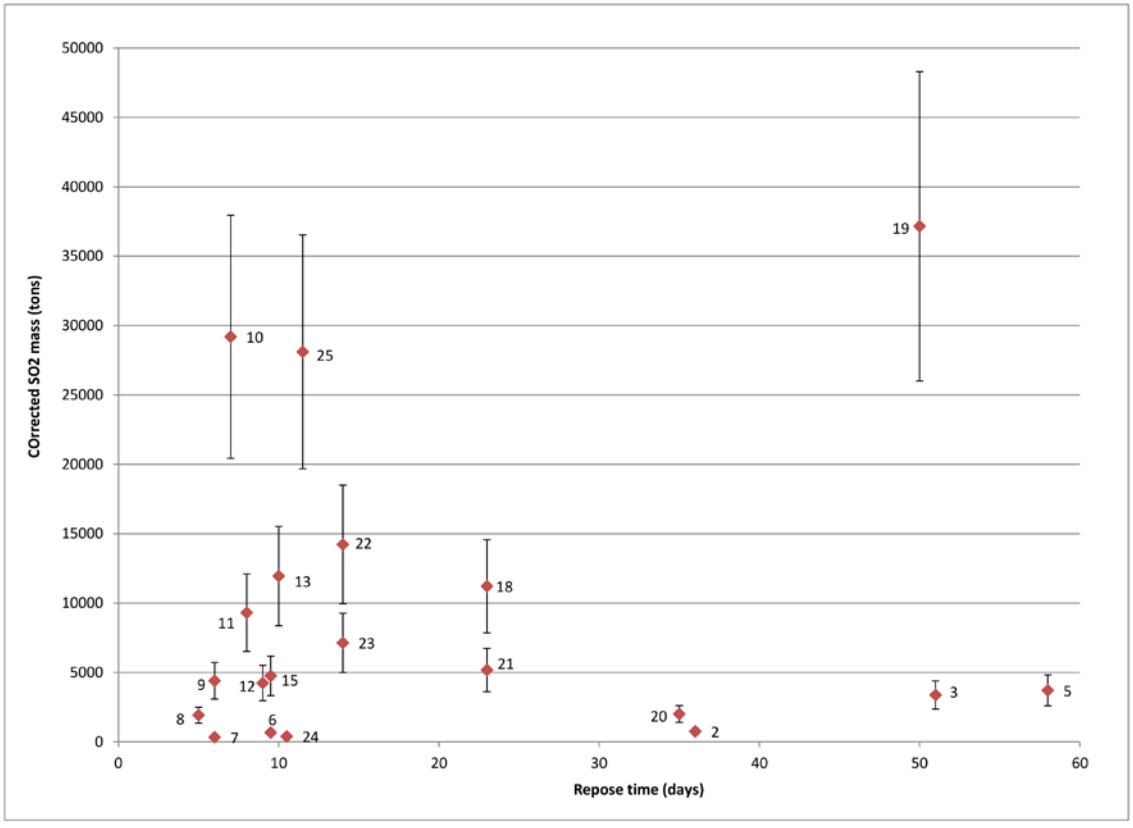

Figure 4.21: Graph of the SO_2 mass against the inter-paroxysm repose time using AIRS data with extrapolated values (average decay and combined extrapolation). Paroxysm number is indicated next to the data points and 30% error is assumed on the SO_2 mass.

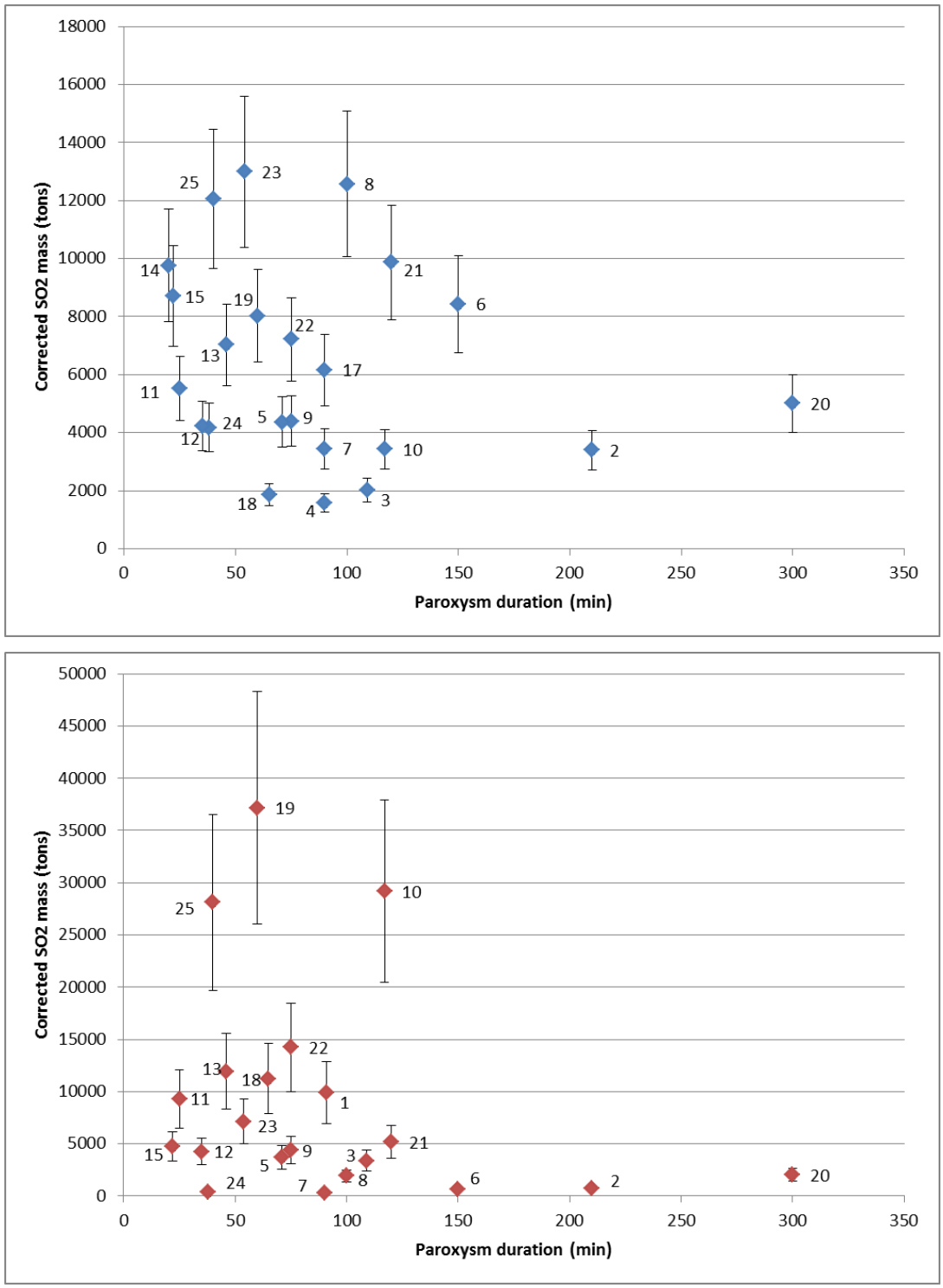

Figure 4.22: Graphs showing the corrected SO_2 mass as a function of paroxysm duration from OMI SO_2 data (in blue) and AIRS SO_2 data (in red) for all paroxysms of the 2011-2012 NSEC cycle. Paroxysm number is indicated next to the data points.

5. Discussion

A unique feature of the Etna paroxysms is the availability of satellite measurements of SO_2 emissions and ground-based Doppler radar (VOLDORAD 2B) measurements of the lava fountain at the vent. We therefore have constraints on the gas (OMI/AIRS) and particle (radar) emissions from each paroxysm, permitting analysis of the mass balance of the gas and solid phases. Using the mean primary sulphur content in Etnean magma given by Bonaccorso et al. (2011) as 0.3 wt%, we can estimate the amount of SO_2 that could be released by the lapilli cloud detected by Doppler radar. We select the 1st paroxysm for comparison owing to better data availability. In my previous study (Bonny, 2012), based on the VOLDORAD 2B data, I estimated a total mass of lapilli ejected of 3.85×10^6 kg, assuming a density of 550 kg/m^3 and monodisperse particle size distribution with a diameter of 11.2 mm (Appendix 8.7). To determine the amount of SO_2, we multiply the sulphur content in typical Etna magma by our total mass of particles emitted and multiply the result by 2 (SO_2 molar mass is twice the one of sulphur); assuming that it would give us a first order estimation, although it is likely that a significant fraction of the plume did not cross the radar beam. This yields an estimated 23 tons of SO_2 that could have been sourced from the lava emitted by the 1st paroxysm, which is much lower than AIRS assessment of 7000 tons. This vast excess of gas emission compared to the radar data provides more support for the hypothesis that a gas-rich foam layer drives the lava fountains (the CF model), and is also consistent with suggestions that Etna releases gas from unerupted magma. In fact, Bonaccorso et al. (2011) estimated that the ratio between degassed and erupted volumes, for Etna's NSEC lava fountains of 10 April 2011, is about 10:1.

All paroxysms (except one) were recorded by VOLDORAD 2B and the radar power time series were processed. Each time-series is specific for the paroxysm and they show different shapes and durations We can classify them based on the outline shape of the gate with the maximum power (mainly the 1st and 2nd gates) in 3 different groups: top-hat shape, and asymmetric triangular with sharp increase or sharp decrease. Most of the

eruptions show a top-hat shape (about 50%) and the rest splits equally between the other two shapes. An example of a radar power time-series from the 1st paroxysm is shown in Figure 5.1 that shows a top-hat shape (this was also studied by Calvari et al., 2011). It is however not possible to find a correlation between the radar power outline and the corrected SO_2 mass that we calculated with OMI and AIRS. Therefore, this suggests i) either that the particle emission and gas emission do not follow the same mechanism – which could be explained by the separation of ash and SO_2 that may occur under conditions of vertical wind shear (Carn et al., 2009; Constantine et al., 2000) –, or (2) other factors that were not taken into account may have a significant influence: a fraction of the plume might have remained undetected (out of beam); the particle size retrieved from the analysis of proximal deposits of the August 29 2011 eruption was not representative of the plume content at beam level, hence errors on mass estimates. However, a problem with this comparison is that the satellite measurements, unlike the radar time-series, do not provide high temporal resolution of SO_2 release (i.e., eruption dynamics) during the paroxysm, only an average SO_2 emission rate.

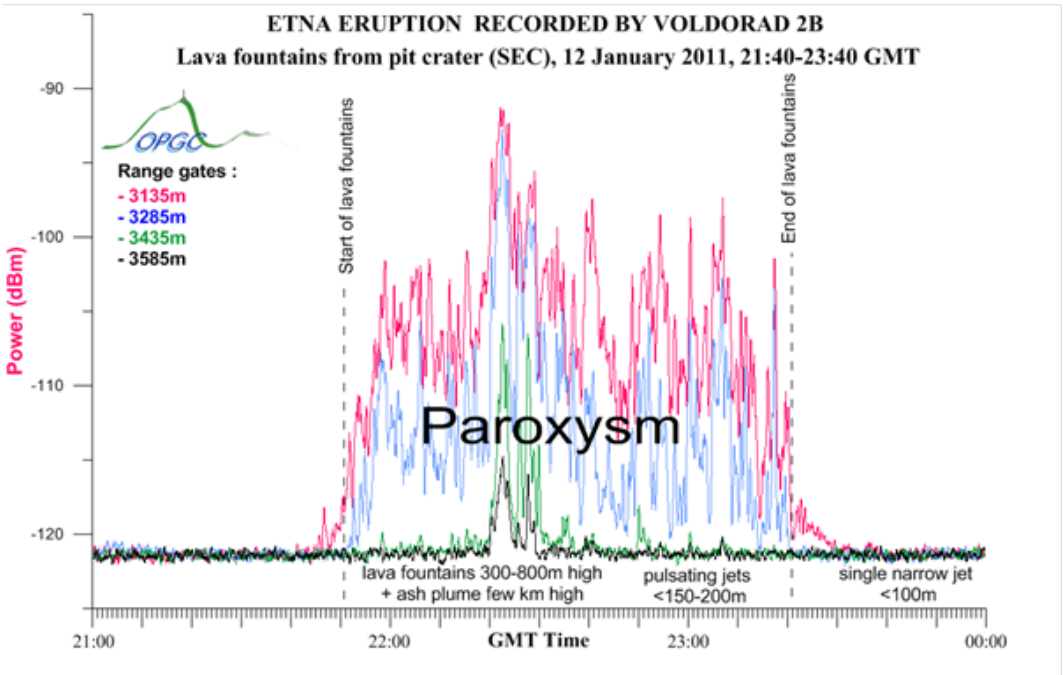

Figure 5.1: Radar power time series of the 1st paroxysm (January 12, 2011) detected by VOLDORAD 2B from the NSEC's at Etna volcano.

VOLDORAD 2B is also able to measure the velocity of particles that cross the radar beam. It is interesting to see if ejection velocity can be linked with the altitude of the volcanic cloud detected by OMI instrument. We used the positive maximum velocity for each paroxysm since it corresponds mainly to particles moving upwards (and away) from the radar, rather than ash fallout. Figure 5.2 shows that there is a global trend linking those 2 parameters: when the velocity of the particle increases the volcanic cloud tends to reach higher altitudes.

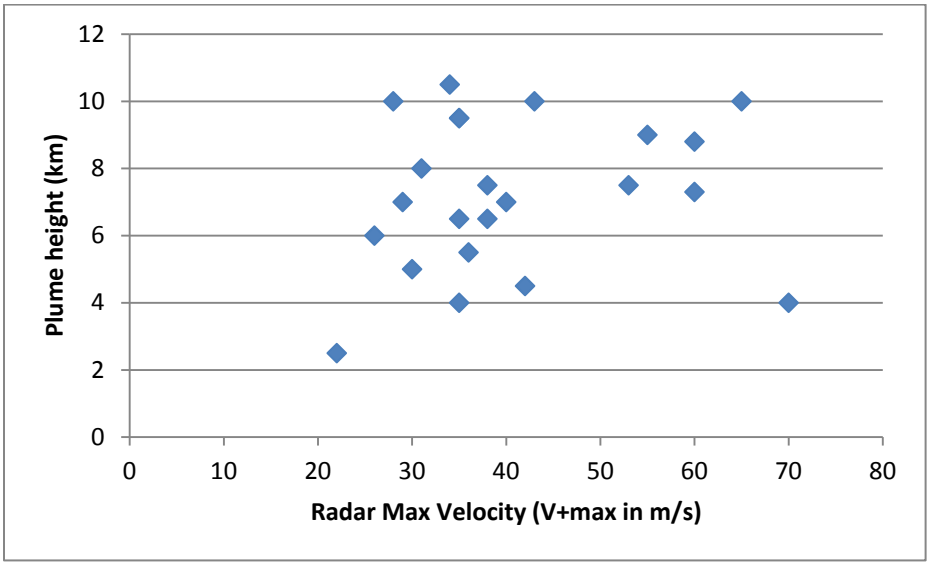

Figure 5.2: Graph showing plume height determined with HYSPLIT against the Maximum Positive Velocity detected by VOLDORAD 2B for the paroxysms of Etna's NSEC.

In this analysis, the plume height determination plays a key role in the retrieval of SO_2 emitted by Etna's NSEC lava fountains. It significantly impacts the calculation of SO_2 mass since we linearize the OMI data for the given altitude. Underestimating the plume altitude will usually give an overestimation of the SO_2 mass and vice versa (Carn et al., 2008). However, estimates of plume altitude are rarely available directly (INGV-reports sometimes report plume altitude, though it can be difficult to determine from the ground) but depend on other indirect techniques such as CALIPSO lidar measurements, HYSPLIT modeling or AIRS images. In our case, CALIPSO couldn't be used since it misses Etna SO_2 clouds probably due to their small sizes. Therefore, we mainly used the

HYSPLIT trajectory model to obtain more precise estimation of altitude, which gives a value for every day after the explosion since the plume height can vary with time. Those estimations were also used to extrapolate the corrected SO_2 mass for the paroxysms that did not have enough OMI data. AIRS data were mainly used to track the volcanic cloud but it also helped to constrain the plume height when used in combination with OMI data (Carn et al., 2009).

Volcanic cloud altitude also determines the effect of eruptions on aviation and climate as well as being a proxy for eruption intensity (Carn et al., 2009b). Explosive magmatic eruptions, such as lava fountains, produce volcanic clouds containing ash and gas (H_2O, CO_2 and SO_2), that can reach aircraft cruising altitudes (9-11 km) and therefore the presence of SO_2 generally indicates that ash is also present. In our cases, the OMI Aerosol Index (AI) did not detect significant ash content in the Etna eruption clouds, and we infer that most ash falls out near the vent and little remains for long-range transport. Hence, whilst some of the Etna plumes appear to have reached cruising altitudes, they may not be a major hazard to aviation except close to the source. The effect of volcanic ash on airplanes is well known, especially after the Eyjafjallajökull crisis in 2010 (Stohl et al. (2011), Thomas and Prata (2011), Langmann et al. (2012)), but the effects of SO_2 are still controversial. Sulfate aerosol could cause airframe damage, overheating and power loss according to Carn et al. (2009). It is therefore important to track SO_2 clouds from volcanic eruptions to prevent any aviation hazard caused by the gas itself or volcanic ash. UV measurements from OMI as well as IR AIRS data are produced in near real-time to be used by Volcanic Ash Advisory Centers (VAACs) for aviation hazard mitigation. For instance, Catania's international airport (about 35 km away from Etna's summit) has suffered repeated temporary closures because of the hazard that gas and ash pose to aviation (Bonaccorso et al., 2011).

Lava fountains have been a recurrent phenomenon at Etna's summit craters in recent decades (Bonaccorso, 2006), including the 2000 cycle, 2001, 2008, 2011-2012 cycles,

and the 2013 sequence that is still ongoing. They produce a jet of hot pyroclasts ejected at high altitude above the vent (hundreds of meters) associated with an ash plume and fall-out that pose a hazard to aviation. Therefore, it is important to study and understand the driving mechanism of this explosive activity, in order to recognize possible precursors. Previous work on Etna's lava fountains includes Allard (1997), Allard et al. (2005), Vergniolle and Ripepe (2008), Bonaccorso et al. (2011), whilst Parfitt (2004) studied Hawaiian lava fountains at Kilauea. Two different driving mechanisms have been proposed (the RSD and CF models) but previous studies have suggested that Etna's paroxysms are driven by a gas phase that accumulated before eruption in a storage zone at about 2 km depth below the summit. The RSD model can explain paroxysms at any open system but the CF model requires a gas accumulation in a deeper storage area, which is apparently the case for Etna. However, it is important to note that there is not one model better than the other and one doesn't have to explain all the Strombolian eruptions (Parfitt, 2004). Another point of view regarding Etna's eruptions states that the eruptive episode starts with strombolian activity, which becomes more and more frequent and transitions to nearly continuous activity generating lava fountains (Bertagnini et al. 1990, the 1989 eruptive sequence) but these are older eruptions. Therefore this might suggest that perhaps the system has changed and produced a change in the volcanic activity. This fast transition in activity has been explained by a rapid variation in the rise speed of the magma, which is the essence of the RSD model. These observations cannot be explained by the CF model since it depends on magma viscosity and gas accumulation that is not a fast process (Parfitt, 2004). In summary, in this project our data set suggests that the CF model is the more likely driving mechanism for the 2011-2012 cycle of lava fountains at Etna. Our data provides the first evidence of gas accumulation (i.e., the CF model) driving an entire sequence of lava fountain events.

A recent paper from Ganci et al. (2012) gives information about erupted volumes and mean output rates during one year of lava fountaining at Mount Etna (January 2011 to January 2012) using high temporal resolution thermal data (SEVIRI). We used their

estimation of total lava volume erupted and the duration of eruptions to compare the intensity and sulphur mass balance of the paroxysms with our datasets. We used the same technique, as with radar data, to estimate how much SO_2 would have been emitted by their calculated total dense rock lava volume of $28x10^6$ m^3 and we found that about 450 ktons of SO_2 would have been released for those 19 paroxysms. For the same episodes, OMI and AIRS detected about 100 ktons of SO_2. However, there are also other factors to consider, like the crystal content of the lava (30% is assumed for Etna lavas). Since only the non-crystallized fraction of the magma can degas, this also affects the calculations. Also, the percentage of sulphur degassing from the lava may not be 100%. Using all these assumptions, we finally estimated that about 200-300 ktons would have been emitted. Therefore, our calculations suggest that the estimated SO_2 emissions from Ganci et al.'s data are maybe a factor of 2-3 higher, so not hugely different. This can easily be explained by passive degassing of the stored magma before each paroxysm since Etna typically emits about 2000 tons of SO_2 per day; therefore a difference of 100 to 200 ktons could be reached in about 50 to 100 days which is reasonable for the time interval of a year for Etna volcano.

We also wanted to compare our data with their mean output rate and the data are shown in Table 5.1. We can see that the intensities calculated with the satellite data are a lot higher than the estimation made by Ganci et al. (2012). This intensity comparison is certainly problematic due to the differences in duration from the radar and thermal IR data. As Ganci et al. point out in their paper, the IR signal can saturate and/or be obscured by the plume at the peak of activity (which is what the radar and gas data are most sensitive to), so their intensities may be underestimates of peak intensities. Furthermore, it is probable that the paroxysm duration that VOLDORAD 2B detected does not correspond to Phase 1 and Phase 2, like they used for their calculations, but only Phase 2

Table 5.1 : Intensity comparison between OMI, AIRS data and SEVIRI data (from Ganci et al., 2011) based on paroxysm duration detected by Doppler radar for 19 paroxysms.

	VOLDORAD 2B		OMI		AIRS		SEVIRI (Ganci et al., 2011)	
Date	Paroxysm duration (min)	paroxysm duration (s)	SO2 mass (tons)	Intensity (kg/s)	SO2 mass (tons)	Intensity (kg/s)	duration phase 1 and 2 (min)	Mean output rate (m3/s)
1/12/2011	91	5460			8500	1556.8	255	101.2
2/18/2011	210	12600	3390	269.0	750	59.5		
4/10/2011	109	6540	2020	308.9	3360	513.8	495	29.5
5/12/2011	90	5400	1570	290.7			570	43.1
7/9/2011	71	4260	4370	1025.8	3710	870.9	243	102.3
7/19/2011	150	9000	8420	935.6	650	72.2	240	148.5
7/25/2011	90	5400	3440	637.0	320	59.3	630	26.1
7/30/2011	100	6000	12570	2095.0	1870	311.7	810	45.7
8/5/2011	75	4500	4400	977.8	4450	988.9	270	98
8/12/2011	117	7020	3430	488.6	29190	4158.1	210	226.7
8/20/2011	25	1500	5530	3686.7	9310	6206.7	330	70.8
8/29/2011	35	2100	4230	2014.3	4210	2004.8	255	113.7
9/8/2011	46	2760	7020	2543.5	11940	4326.1	180	112.6
9/19/2011	20	1200	9770	8141.7				
9/28/2011	22	1320	8700	6590.9	4710	3568.2	228	29.7
10/8/2011	25	1500					465	30.2
10/23/2011	90	5400	6170	1142.6			150	145.7
11/15/2011	65	3900	1860	476.9	10970	2812.8	273	110.4
1/5/2012	60	3600	8030	2230.6	37160	10322.2	318	78.3

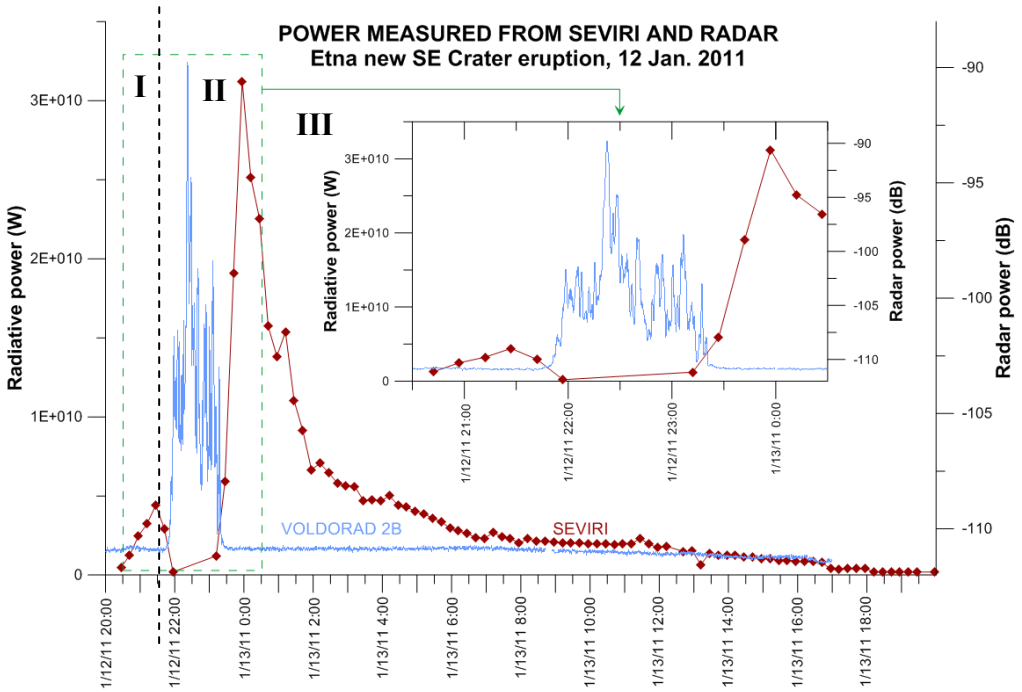

Figure 5.3: Plot showing the radiative power detected from SEVIRI and the radar power detected by VOLDORAD 2B for the 1st paroxysm on January 12, 2011 against time. The 3 different phases defined by Ganci et al. (2012) are shown in bold font, the green box correspond to phase 1 and 2. Modified from S. Valade thesis (2012).

with the higher heat flux. This can be seen in Figure 5.3 with an example from the 1st paroxysm of the cycle with VOLDORAD detection starting at the beginning of phase 2. We can also notice that the radar could help to constrain information about the intensity of the eruption when the thermal measurements cannot give information. This could be studied in further detail as part of a future work.

6. Conclusion

SO_2 retrievals were processed for paroxysmal degassing of Etna's NSEC in 2011-2012 using satellite data from the UV OMI and IR AIRS instruments in NASA's A-Train spacecraft constellation. OMI allows daily global coverage at the highest sensitivity in near real time and was able to track Etna's SO_2 plumes for several days. Back trajectories calculated using the HYSPLIT trajectory model was used to constrain the altitude of the SO_2 clouds. Ground-based data retrieved from VOLDORAD 2B constrain precisely the time of each paroxysm and we find that the radar measurements are in global agreement with the trajectory estimation, indicating that most SO_2 release coincides with peak lava fountain intensity. SO_2 loadings were derived from both OMI and AIRS allow parameterization of the exponential SO_2 decay rate for each paroxysm. In addition to providing additional constraints on SO_2 loadings, use of the IR AIRS data along with OMI allowed us to exploit the synergy between these sensors and constrain the altitude of the emitted SO_2. We also showed that some validation of AIRS SO_2 retrievals is possible using OMI, but it is more robust for high altitude clouds, consistent with previous work. Our observation of a correlation between the corrected SO_2 mass at the onset of each eruption and the inter-paroxysm repose time validates the CF model as driving mechanism for explosive basaltic eruptions at Etna. The observed correlation between ejection velocity and plume altitude also confirms the utility of ground-based Doppler radar data (VOLDORAD 2B) as a tool for aviation hazard mitigation. Hence this study of gas emissions from space, combined with different geophysical techniques, improves our understanding of the driving mechanism of explosive basaltic eruptions.

7. References

[1] Parfitt E.A (2004). A discussion of the mechanisms of explosive basaltic eruptions. *J. Volcanol. Geotherm. Res.* **134**, 77-107.

Aiuppa, A., et al. (2010), Patterns in the recent 2007–2008 activity of Mount Etna volcano investigated by integrated geophysical and geochemical observations, *Geochem. Geophys. Geosyst.,* **11**, Q09008, doi:10.1029/2010GC003168.

Allard P. (1997). Endogenous magma degassing and storage at Mount Etna, *Geophysical Research Letters*, **vol. 24**, NO. 17, PAGES 2219-2222.

Allard, P., M. Burton, and F. Murè (2005). Spectroscopic evidence for lava fountain driven by previously accumulated magmatic gas, *Nature*, **433**, 407–410, doi:10.1038/nature03246.

Alparone, S., D. Andronico, L. Lodato, and T. Sgroi (2003), Relationship between tremor and volcanic activity during the Southeast Crater eruption on Mount Etna in early 2000, *J. Geophys. Res*., **108(B5)**, 2241, doi:10.1029/2002JB001866.

Andronico, D., and R. A. Corsaro (2011). Lava fountains during the episodic eruption South East Crater (Mt. Etna), 2000: Insights into magma gas dynamics within the shallow volcano plumbing system, *Bull. Volcanol.*, **73**, doi:10.1007/s00445-011-0467-y.

Armienti, P., Tonarini, S., D'Orazio, M., and Innocenti, F., (2004). Genesis and evolution of Mt. Etna alkaline lavas: Petrological and Sr-Nd-B isotope constraints: *Periodico di Mineralogia,* **v. 73**, p. 29–52.

Barrie, L. A., et al. (2001), A comparison of large scale atmospheric sulphate aerosol models (COSAM): Overview and highlights, *Tellus*, Ser. B, **53**, 615–645.

Behncke, B., M. Neri, E. Pecora, and V. Zanon (2006). The exceptional activity and growth of the Southeast Crater, Mount Etna (Italy), between 1996 and 2001, *Bull. Volcanol.*, **69**, 149–173, doi:10.1007/s00445-006-0061-x.

Bertagnini, A., Calvari, S., Coltelli, M., Landi, P., Pompilio, M., Scribano, V. (1990). The 1989 eruptive sequence. In: Barberi, F., Bertagnini, A., Landi, P. (Eds.), Mt. Etna: the 1989 eruption, *C.N.R.–Gruppo Nazionale Per La Vulcanologia Italy*, Giardini.

Bluth GJS, Carn SA (2008). Exceptional sulfur degassing from Nyamuragira volcano, 1979–2005. *Int J Remote Sens* , **Vol. 29**, Iss. 22.

Bonaccorso, A. (2006), Explosive activity at Mt. Etna summit craters and source modelling by using high precision continuous tilt, *J. Volcanol. Geotherm. Res.,* **158**, 221–234, doi:10.1016/j.jvolgeores.2006.05.007.

Bonaccorso, A., et al. (2011). Dynamics of a lava fountain revealed by geophysical, geochemical and thermal satellite measurements: The case of the 10 April 2011 Mt Etna eruption, *Geophys. Res. Lett.,* **38**, L24307, doi:10.1029/2011GL049637.

Bonaccorso, A., A. Cannata, R. A. Corsaro, G. Di Grazia, S. Gambino, F. Greco, L. Miraglia, and A. Pistorio (2011b), Multi-disciplinary investigation on a lava fountain preceding a flank eruption: The 10 May 2008 Etna case, *Geochem. Geophys. Geosyst*., **12**, Q07009, doi:10.1029/ 2010GC003480.

Bonny, E. (2012). Study of the ash plumes from Etna volcano: a perspective from Doppler radar and deposits analysis. Master 1 Sciences de la Terre T.E.R. report, Univ. Blaise Pascal, Clermont-Ferrand II, pp. 27.

Bousquet J-C, Lanzafame G. (2001). Nouvelle interpretation des fractures des eruptions laterales de l'Etna; consequences pour son cadre tectonique, *Bulletin de la Societe Geologique de France*, **v. 172**, p. 455-467, doi: 10.2113/172.4.455.

Burton M, Caltabiano T, Salerno GG, Mure F, Condarelli D. (2004). Automatic measurements of SO2 flux on Stromboli and Mt. Etna using a network of scanning UV spectrometers. *Geophysical Research Abstracts*. 6,03970.

Calvari S., Gropelli G., Pasquarè G. (1994a). Preliminary geological data on the south-western wall of the Valle del Bove, Mt. Etna, Sicily. *Acta Vulcanologica*, **vol. 5**, 15-30.

Calvari S., G. G. Salerno, L. Spampinato, M. Gouhier, A. La Spina, E. Pecora, A. J. L. Harris, P. Labazuy, E. Biale, and E. Boschi (2011). An unloading foam model to constrain Etna's 11–13 January 2011 lava fountaining episode. *J. Geophys. R.*, **Vol 116**, B11207, doi: 10.1029/2011JB008407.

Carn SA, Strow LL, de Souza-Machado S, Edmonds Y, Hannon S (2005). Quantifying tropospheric volcanic emissions with AIRS: the 2002 eruption of Mt. Etna (Italy). *Geophys Res Lett,* **32**, L02301, doi:10.1029/2004GL021034.

Carn SA, Krueger AJ, Krotkov NA, Arellano S, Yang K (2008). Daily monitoring of Ecuadorian volcanic degassing from space. *J Volcanol. Geotherm. Res.* **176**, 141-150.

Carn S.A, Krueger AJ, Krotkov NA, Yang K, Evan K (2009). Tracking volcanic sulfur dioxide clouds fo aviation hazard mitigation. *Nat Hazards.* **51**, 325-343.

Carn S. A., J. S. Pallister, L. Lara, J. W. Ewert, S. Watt, A. J. Prata, R. J. Thomas, and G. Villarosa (2009b). *Eos*, **Vol. 90**, No. 24.

Carn S.A. (2011b) "OMIplot", [Internet]: https://vhub.org/resources/682.

Carn, S.A. (2012). OMI data processing at MTU.

Chin, M., R. B. Rood, S.J. Lin, J.F. Müller, and A. M. Thompson (2000). Atmospheric sulfur cycle in the global model GOCART: Model description and global properties, *J. Geophys. Res.*, **105**, 24,671–24,687, doi:10.1029/2000JD900384.

Coltelli M., Del Carlo P., Vezzoli L. (1998). Discovery of a Plinian basaltic eruption of Roman age at Etna volcano, Italy. *Geology*, **v. 26** no. 12 p. 1095-1098, doi: 10.1130/0091-7613.

Constantine EK, Bluth GJS, Rose WI (2000) TOMS and AVHRR observations of drifting volcanic clouds from the August 1991 eruptions of Cerro Hudson. In: Mouginis-Mark PJ, Crisp JA, Fink JH (eds) Remote sensing of active volcanism. Geophysical monograph **116**, *American Geophysical Union*, Washington, DC, pp 45–64

Corsaro RA, Cristofolini R, Patane L. (1996). The 1669 eruption at Mount Etna: chronology, petrology and geochemistry, with inferences on the magma sources and ascent mechanisms. *Bulletin of Volcanology*. 58:348-358.

Cullis, C. F. and Hirschler, M. M. (1980). Atmospheric Sulfur- Natural and Man-made sources, *Atmos. Environ.*, **14**, 1263–1278.

Davies, P . Delmelle, G. E. Norton, A.J.H. Maciejewski, C.M.M. Oppenheimer, J. Stix and I. M. Watson (1998). Monitoring SO_2 emission at the Soufriere Hills volcano: Implications for changes in eruptive conditions, *Geophysical Research Letters*, **Vol. 25**, no. 19, pages 3681-3684.

Donnadieu F., G. Dubosclard, P. Allard, R. Cordesses, C. Hervier, J. Kornprobst and J.F. Lénat (2003). Sondages des jets volcaniques par radar Doppler: applications à l'Etna. Rapport quadriennal, C.N.F.G.G., 1999-2000, pp. 199-124.

Donnadieu F., G. Dubosclard, R. Cordesses, T. Druitt, C. Hervier, J. Kornprobst, J.F. Lénat, P. Allard, and M. Coltelli (2005). Remotely monitoring volcanic activity with ground-based Doppler radar, *Eos Trans. AGU*, **86**, 204, doi:10.1029/2005EO210001.

Donnadieu, F., Hervier, C., Freville, P., Fournet-Fayard, J., Fournol, J.-F., Menny, P., Reymond, C., & Bernard, C. (2009). The VOLDORAD 2B radar: Operational handbook, *Note OPGC 07.09*, Univ. Blaise Pascal Clermont-Ferrand.

Donnadieu, F., Valade, S., & Moune, S. (2011). Three dimensional transport speed of winddrifted ash plumes using ground-based radar. *Geophys. Res. Lett*., **38**, L18310, doi:10.1029/2011GL049001.

Donnadieu F. (2012). Volcanological applications of Doppler radars: a review and examples from transportable pulse radar in L-band. In 'Chapter 17, Doppler radar Observations - Weather Radar, Wind Profiler, Ionospheric Radar, and Other Advanced Applications', Bech J. and Chau J.L. (Eds.), ISBN: 978-953-51-0496-4, InTech, p. 409-446.

Dubosclard G., Donnadieu F., Allard P., Cordesses R., Hervier C., Coltelli M., Privitera E., Kornprobst, J. (2004). Doppler radar sounding of volcanic eruption dynamics at Mount Etna. *Bull. Volcanol*., **66**, 5, p. 443-456. DOI : 10.1007/s00445-003-0324-8.

Ganci, G., A. J. L. Harris, C. Del Negro, Y. Guehenneux, A. Cappello, P. Labazuy, S. Calvari, and M. Gouhier, 2012. A year of lava fountaining at Etna: Volumes from SEVIRI, Geophys. Res. Lett., 39, L06305, doi:10.1029/2012GL051026.

Gouhier M., Donnadieu F., 2006. Numerical modelling of Doppler radar signals of Strombolian eruptions, *Eos Trans. AGU*, **87(52)**, Fall Meet. Suppl., Abstract V43B-1794.

Gouhier M., Donnadieu F. (2008). Mass estimations of ejecta from Strombolian explosions by inversion of Doppler-radar measurements. *J. Geophys. Res*., **VOL. 113**, B10202, doi:10.1029/2007JB005383.

Gouhier M., Donnadieu F. (2010). The geometry of Strombolian explosions: insights from Doppler radar measurements. *Geophys. J. Int.*, **183**, 1376-1391, doi:10.1111/j.1365-

246X.2010.04829.x

Gouhier M., Donnadieu F. (2011). Systematic retrieval of ejecta velocities and gas fluxes at Etna volcano using L-Band Doppler radar. *Bull Volcanol*, **73**:1139-1145. DOI: 10.1007/s00445-011-0500-1.

Guest J.E., D.K. Chester, A.M. Duncan (1984). The valle del bove, Mount Etna: Its origin and relation to the stratigraphy and structure of the volcano, Original Research Article, *JVGR*, **Vol. 21**, Issues 1–2, Pages 1-23.

Gvirtzman Z.and A.Nur (1999). The formation of Mount Etna as the consequence of slab rollback. *Nature* **401**, 782-785, doi:10.1038/44555.

HYSPLIT Trajectory Model [Internet]: http://ready.arl.noaa.gov/HYSPLIT_traj.php

INGV Sezione di Catania – Osservatorio Etneo [Internet]: http://www.ct.ingv.it/index.php?option=com_docman&Itemid=344&lang=en

Jaupart, C., Vergniolle, S., 1988. Laboratory models of Hawaiian and Strombolian eruptions. Nature 331, 58– 60.

Jaupart, C., Vergniolle, S., 1989. The generation and collapse of foam layer at the roof of a basaltic magma chamber. J. Fluid Mech. 203, 347– 380.

Kieffer G, Tanguy J-C (1993). L'Etna: évolution structurale, magmatique et dynamique d'un volcan «polygénique» = The Mount Etna : structural, magmatic and dynamic evolution of a polygenic volcano, *Société Gologique de France.*

Klerkx J. (1970). La caldera de la Valle del Bove: sa signification dans l'évolution de l'Etna (Sicile), *Bulletin Volcanologique*, **Vol. 34**, Issue 3, pp 726-737.

Krotkov, N. A., S. A. Carn, A. J. Krueger, P. K. Bhartia, and K. Yang (2006). Band residual difference algorithm for retrieval of SO2 from the Aura Ozone Monitoring Instrument (OMI), *IEEE Trans. Geosci. Remote Sens.,* **44(5)**, 1259-1266, doi:10.1109/TGRS.2005.861932.

Krotkov N.A., B. McClure, R.R. Dickerson, S.A. Carn, C. Li, P.K. Bhartia, K. Yang, A.J. Krueger, Z. Li, P.F. Levelt, H. Chen, P. Wang, and D. Lu (2008). Validation of SO2 retrievals from the Ozone Monitoring Instrument over NE China, *J. Geophys. Res.,* **113**,

D16S40, doi:10.1029/2007JD008818.

Krotkov, N. A., M. R. Schoeberl, G. A. Morris, S. Carn, and K. Yang (2010), Dispersion and lifetime of the SO2 cloud from the August 2008 Kasatochi eruption, *J. Geophys. Res.*, **115**, D00L20, doi:10.1029/2010JD013984.

Krueger AJ, Walter LS, Bhartia PK, Schnetzler CC, Krotkov NA, Sprod I, Bluth GJS (1995), Volcanic sulfur dioxide measurements from the total ozone mapping spectrometer instruments. J Geophys Res, **100**:14057–14076.

Langmann B., Folch A., Hensch M., Matthias V. (2012). Volcanic ash over Europe during the eruption of Eyjafjallajökull on Iceland, April–May 2010. *Atmospheric Environment* **48**, 1-8, doi:10.1016/j.atmosenv.2011.03.054.

Manning, E. M. (2002), AIRS version 2.6.7.3 sample data interface specification, Rep. JPL D-24641, Jet Propul. Lab. Calif. Inst. of Technol., Pasadena.

Mora, M.M., Lesage, P., Donnadieu, F., Valade, S., Schmidt, A., Soto, G., Taylor, W., & Alvarado, G. (2009). Joint Seismic, Acoustic and Doppler Radar observations at Arenal Volcano, Costa Rica: preliminary results. In: *The VOLUME project*, Bean, C. J., Braiden, A. K., Lokmer, I., Martini, F., & O'Brien, G. S. , pp. (330-340), VOLUME Project Consortium, ISBN 978-1-905254-39-2, Dublin.

McGuire W.J. (1982). Evolution of the etna volcano: Information from the southern wall of the Valle Del Bove Caldera. Original Research Article, *Journal of Volcanology and Geothermal Research*, **Vol. 13**, Issues 3–4, Pages 241-271.

NASA Goddard Space Flight Center, OMSO2 Readme File [Internet]: http://so2.gsfc.nasa.gov/Documentation/OMSO2Readme_V111_0818.htm

Prata, A. J., and C. Bernardo (2007). Retrieval of volcanic SO2 column abundance from Atmospheric Infrared Sounder data, *J. Geophys. Res.*, **112**, D20204, doi:10.1029/2006JD007955.

Sauvageot, H. (1992). Radar Meteorology, 366 pp., Artech House, Boston, Mass.

Schiano et al. (2001). Transition of Mount Etna lavas from a mantle-plume to an island-arc magmatic source. *Nature,* **412**, 900-904.

Sigurdsson H. (1982). Volcanic pollution and climate: The 1783 Laki eruption, *Eos, Transactions American Geophysical Union*, **Volume 63**, Issue 32, pages 601–602.

Smithsonian/USGS – Global Volcanism Program [Internet]: http://www.volcano.si.edu/volcano.cfm?vnum=0101-06=

Stohl A., A. J. Prata, S. Eckhardt, L. Clarisse, A. Durant, S. Henne, N. I. Kristiansen, A. Minikin, U. Schumann, P. Seibert, K. Stebel, H. E. Thomas, T. Thorsteinsson, K. Tørseth, and B.Weinzierl (2011). Determination of time- and height-resolved volcanic ash emissions and their use for quantitative ash dispersion modeling: the 2010 Eyjafjallajökull eruption, *Atmos. Chem. Phys*., **11**, 4333–4351, doi:10.5194/acp-11-4333-2011.

Thomas H. E., A.J. Prata (2011). Sulphur dioxide as a volcanic ash proxy during the April–May 2010 eruption of Eyjafjallajökull Volcano, Iceland. *Atmos. Chem. Phys.,* **11**, 6871–6880, doi:10.5194/acp-11-6871-2011.

Valade, S. & Donnadieu, F. (2011). Ballistics and ash plumes discriminated by Doppler radar. *Geophys. Res. Lett.,* **38**, L22301, doi:10.1029/2011GL049415.

Valade, S., Donnadieu, F., Lesage, P., Mora, M.M., Harris, A. & Alvarado, G.E. (2012). Explosion mechanisms at Arenal volcano, Costa Rica: an interpretation from integration of seismic and Doppler radar data. *J. Geophys. Res*., **117**, B1, doi:10.1029/2011JB008623.

Valade S. (2012). Source mechanisms and emission dynamics of volcanic pyroclastic emissions: a perspective from Doppler radar and other geophysical data. Thesis at Blaise Pascal University.

Vergniolle S, Jaupart C (1986). Separated two-phase flow and basaltic eruptions. *J Geophys Res,* **91**:12842–12860.

Vergniolle S, Mangan M (2000). Hawaiian and Strombolian eruptions. *In: Sigurdsson H et al (eds) Encyclopedia of volcanoes*. pp 447-461.

Vergniolle, S., and M. Ripepe (2008), From Strombolian explosions to fire fountains at Etna Volcano (Italy): What do we learn from acoustic measurements?, in Fluid Motions in Volcanic Conduits: A Source of Seismic and Acoustic Signals, edited by S. J. Lane and J. S. Gilbert, *Geol. Soc. Spec. Publ*., **307**, 103-124.

VOLDORAD, Service d'Observation des radars Doppler Volcanologiques, OPGC [Internet]: http://wwwobs.univ-bpclermont.fr/SO/televolc/voldorad/voldo2bText.php

Wilson L., Sparks R.S.J.. Huang T-C., Watkins N.D, (1978). The control of volcanic column heights by eruption enegetics and dynamics. J. Geophys. Res. 83, 1829-1836).

Yan H., L. Chen, J. Tao, L. Su, J. Huang, D. Han, and C. Yu (2012). Corrections for OMI SO2 BRD retrievals influenced by row anomalies. *Atmos. Meas. Tech.*, **5,** 2635–2646, doi:10.5194/amt-5-2635-2012.

Yang K, Krotkov NA, Krueger AJ, Carn SA, Bhartia PK, Levelt PF (2007) Retrieval of large volcanic SO2 columns from the Aura Ozone Monitoring Instrument: comparison and limitations. *J Geophys Res,* **112**, D24S43, doi:10.1029/2007JD008825.

Young S. R., P. W. Francis, J . Barclay, T. J. Casadevall, C. A. Gardner, B. Darroux, M. A.

8. Appendix

8.1 Hysplit table

Paroxysm number	Date paroxysm	Paroxism phase (radar) UTC	date Omi images	starting point (lat)	starting point (long)	ending time	altitude (m)	plume height above Etna (m)	supposed emission time	time difference radar and hysplit (hours)
1	12/01/11	1:50-23:21	13/01/11				anomaly			
2	18/02/11	7:20-10:50	18/02/11	36,42	13,97	12:12	8000	7000	07:00	-0,333
			19/02/11	32,5	24,5	11:17	3000	1500	18/02/2011 22:00	14,666
3	10/04/11	0:48-12:37	10/04/11	36,7	15,5	12:42	4000	3500	09:00	-1,8
4	12/05/11	1:50-03:20	12/5/11	31	22,5	12:42	7500	8400	03:00	1,166
5	09/07/11	4:03-15:14	10/7/11	30,2	10,5	12:26	6500	6600	12:00	-2,05
6	19/07/11	0:00-02:30	19/07/11				anomaly			
			20/07/11	26,5	22,5	11:23	4500	5800	18/07/2011 21:00	3
7	25/07/11	4:00-05:30	25/07/11	39	20,4	11:40	7000	7000	07:00	3
8	30/07/11	9:35-21:15	31/07/11	42	27	11:05	6000	6500	19:30	-0,083
			01/08/2011	47,8	42	10:13	4800	5800	19:00	-0,583
9	05/08/11	1:55-23:10	6/8/11	35,5	17	12:05				
			7/8/11	38,5	24	11:10	10000	10800	06/08/2011 07:00	9,083
			8/8/11	38,6	31,8	10:16	7700	10500	06/08/2011 00:00	2,083
			09/08/11	38	45	10:59	6100	10500	18:00	3,916
10	12/08/11	8:50-10:05	12/8/11	37	15,5	11:29	2500	2300	06:00	-2,833
			13/8/11	31,5	28	12:11	6500	9000	11:00	2,166
			14/8/11	28	32	11:19	3000	5000	12/08/2011 00:00	-8,833
11	20/08/11	7:10-07:35	20/8/11	36,5	14	12:17	10000	9500	07:00	-0,166
			21/8/11	27	6	13:02				
12	29/08/11	4:10-04:45	29/08/11	34,5	30,5	11:00	6800	9600	07:00	2,833
			30/08/11	28	21	11:16	4500	5100	28/08/2011 18:00	10,166
			31/08/11	24	20	11:59	4000	6000	28/08/2011 18:00	10,166
13	08/09/11	7:31-08:17	8/09/11	35,5	16	12:48	7500	7500	06:00	-1,516
			9/9/11	34,2	19	11:53	6500			
			10/9/11	35,5	22,5	12:35				
14	19/09/11	2:30-12:50	20/09/11	51	16	11:38	9500	9500	15:00	2,5
15	28/09/11	9:33-19:55	29/09/11	38	24	11:31	10000	10500	17:00	-1,55
16	08/10/11	4:45-15:10	9/10/11	35,8	28	12:00				
17	23/10/11	8:45-20:15	24/10/11	35,5	22	11:23	5500	6200	18:00	-0,75
			25/10/11	36,2	27	12:05				
18	15/11/11	1:20-12:25	15/11/11				anomaly			
			16/11/11	37	46	09:50	9000	10500	12:00	0,666
19	05/01/12	5:45-06:45	5/1/12	34,5	14,5	12:54	11300	11500	07:00	1,25
			6/1/12	34	39	10:20	7500	9000	05:00	-0,75
20	09/02/12	1:00-06:00	9/2/12	35	12	11:47	5000	6200	08/02/2012 18:00	-7
21	04/03/12	7:30-09:30	4/3/12	39,3	17,7	12:37	7000	6000	06:00	-1,5
			5/3/12	39,5	40	11:42	8400	8700	10:00	2,5
			6/3/12	38	72	09:07	9800	11500	12:00	4,5
22	18/03/12	8:25-09:40	18/3/12	37,4	16,8	12:48	9500	9400	08:00	-0,416
			19/3/12	34,5	30	11:54	11200	11700	10:00	1,583
			20/3/12	34,5	46	10:58	10200	11600	09:00	0,583
			21/3/12	37,5	65	08:24	10800	11500	09:00	0,583
23	01/04/12	2:41-03:35	1/4/12	34	21	11:23	10500	11000	03:00	0,316
			2/4/12	31,2	42,8	10:29	9000	9800	01:00	-1,683
24	12/04/12	4:32-15:10	13/04/12	28	37	11:50	8800	9300	19:00	4,466
25	24/04/12	1:35-02:15	24/04/12	38	22,5	11:30	7300	7500	01:00	-0,583
			25/04/12	38,5	39	10:34	11000	11500	02:00	0,416
			26/04/12	34	44	11:20	9000	11000	04:30	2,916
			27/04/12	37,8	56	10:22	10000	12000	07:00	5,416

8.2 SO2 mass table OMI background.

Date paroxysm	Paroxism phase (radar) UTC	date Omi images	orbit number	plume height (km)	SO2 cloud (ktons) FOV method	area cloud (km2)	window	SO2 background (ktons) FOV method	area back	SO2 cloud mass	SO2 cloud (ktons) FOV method	area cloud	window	SO2 background (ktons) FOV method	area back	SO2 cloud mass	Calculation		Final SO2 mass (ktons)	tons
12/01/11	:1:50-23:21	13/01/11	34560	anomaly																
18/02/11	07:20-10:50	18/02/11	35084	8	2,71595	40890,9	7,5	-0,737286	38156,8	3,403939	2,6713	34334,4	17	-0,46145	28225,1	3,050642	-26,88957	99,03044	3,385344	3385,344
		19/02/11	35098	3	1,28909	41202,1	2,5	-2,17447	43947,3	3,60844	0,481566	25399,8	7,5	-0,44311	25660,2	0,929219	-1,866214	9,234121	3,340518	3340,518
10/04/11	:0:48-12:37	10/4/11	35827	4	2,63979	6355,86	2,5	0,0742172	8261,74	2,543318	0,661023	5854,04	7,5	0,0314972	7545,74	0,620424	-2,600247	9,113255	1,96645	1966,45
12/05/11	01:50-03:20	05/12/2011	36293	7,5	0,756256	34497,4	7,5	-0,49045	28046,4	1,154992							6,493551		1,154992	1154,992
09/07/11	4:03-15:14	07/10/2011	37152	6,5	3,60483	155484	2,5	-0,675256	163123	4,313262	1,92683	154340	7,5	-0,347744	147409	2,258958	-2,433914	12,99811	2,669819	2669,819
19/07/11	10:00-02:30	19/07/11	37283	Anomaly																
		20/07/11	37297	4,5	1,39432	78587,8	2,5	-0,792893	83814,5	2,239947	0,644173	79512	7,5	-0,181469	57344,7	0,77505	-3,41321	10,14541	1,653988	1653,988
25/07/11	4:00-05:30	25/07/11	37370	7	5,50693	99361,2	2,5	0,130094	100023	5,37597	2,71269	87054,6	7,5	0,0681052	75730,3	2,653444	-1,83653	12,37313	2,925697	2925,697
30/07/11	9:35-21:15	31/07/11	37457	6	6,63451	456060	2,5	-0,838373	536239	7,620276	3,35873	440005	7,5	-0,49273	423883	3,833406	-1,320352	12,56144	4,969467	4969,467
		08/01/2011	37471	4,8	0,775062	384408	2,5	-0,662639	411938	1,485157	0,503329	368242	7,5	-0,453806	372630	0,962543	-9,567284	16,70892	1,244754	1244,754
05/08/11	1:55-23:10	08/06/2011	37545	3,5	anomaly															
		08/07/2011	37559	10	2,86598	82172,9	7,5	-0,140578	89766,9	3,01955	2,18954	72142,5	17	-0,096426	78400,9	2,294331	-13,0995	47,05459	2,828703	2828,703
		08/08/2011	37573	7,7	3,02098	306552	7,5	0,260722	247920	2,810124	1,30592	124331	17	0,0940984	118376	1,216329	-5,960613	24,25006	2,776571	2776,571
		08/09/2011	37588	6,1	2,26627	142858	2,5	0,319959	122307	1,992339	1,04713	104803	7,5	0,167169	107844	0,87511	-4,475359	11,41643	1,187934	1187,934
12/08/11	8:50-10:05	08/12/2011	37632	2,5	3,68817	36251,9	2,5	0,389926	43340,2	3,222002							0,775915		3,222002	3222,002
		13/8/11	37647	6,5	4,68736	319525	2,5	0,198014	250052	4,532399	2,07037	180195	7,5	0,0450948	138312	2,035757	-2,002689	11,57699	2,535085	2535,085
		14/8/11	37661	3	1,76355	88641,5	2,5	-0,0594274	79293,2	1,81671	0,892784	78711,4	7,5	0,0369029	67096,6	0,861327	-5,2335	12,00775	1,721172	1721,172
20/08/11	07:10-07:35	20/8/11	37749	10	3,68968	30229,6	7,5	0,0430214	27434,2	3,650637	3,31783	27588,7	17	0,0239111	33565,9	3,288738	-26,25046	103,3309	3,5554	3555,4
		21/8/11	37764	9	0,373647	12352,6	7,5	-0,0497101	16026,2	0,438141	0,291082	8745,27	17	-0,0266191	10105,9	0,321843	-81,6867	43,29026	0,419778	419,7778
29/08/11	4:10-04:45	29/08/11	37880	6,8	Anomaly															
		30/08/11	37894	4,5	1,88814	882646	2,5	-1,29755	822953	3,097937	0,855025	858784	7,5	-0,546741	768870	1,344523	-2,851579	11,33401	2,396571	2396,571
		31/08/11	37909	4	0,889675	573414,8	2,5	-0,0353536	59460,9	0,893341	0,472293	60377,8	7,5	-0,0212114	58983	0,493014	-12,4898	13,65765	0,773243	773,243
08/09/11	07:31-08:17	8/09/2011	38026	7,5	anomaly															
		09/09/2011	38040	6,5	6,26519	159614	2,5	0,1731	166348	6,084787	3,32987	157160	7,5	0,113515	162409	3,212564	-1,740812	13,09247	3,787008	3787,008
		09/10/2011	38055	6,5	5,26287	318998	2,5	0,0520262	197242	5,230701	1,30303	96995,1	7,5	-0,146951	101286	1,456482	-1,324777	9,429514	2,211326	2211,326
19/09/11	2:30-12:50	20/09/11	38200	9,5	0,727819	143059	7,5	-0,810479	145754	1,553566	0,47137	56722,1	17	-0,0539454	50172,2	0,519086	-9,183358	21,76695	1,335781	1335,781
28/09/11	9:33-19:55	29/09/11	38331	10	2,77538	172470	7,5	-0,605033	177899	3,399458	1,93929	124096	17	-0,294476	107204	2,193682	-7,878741	34,28345	3,082149	3082,149
08/10/11	4:45-15:10	10/09/2011	38477	Anomaly																
23/10/11	8:45-20:15	24/10/11	38695	5,5	2,56759	117310	2,5	-0,97511	120670	3,570629	1,26242	85164,6	7,5	-0,139944	88581,6	1,407979	-2,311978	10,75522	2,273039	2273,039
		25/10/11	38710	anomaly																
15/11/11	1:20-12:25	15/11/11	39016	anomaly																
		16/11/11	39029	9	1,29934	463440	7,5	-0,443209	287312	1,57411	1,20608	424627	17	-0,39288	292894	1,477076	-97,90409	161,6118	1,558789	1558,789
05/01/12	5:45-06:45	01/05/2012	39759	11,3	Anomaly															
		01/06/2012	39772	7,5	4,31899	363856	7,5	0,0648509	210263	4,281514							1,751717		4,281514	4281,514
09/02/12	1:00-06:00	9/2/12	40268	5	-1,99332	226395	2,5	-5,32935	231558	3,457567	-0,937795	215421	7,5	-2,52645	232233	1,785826	-2,990893	12,84121	2,621696	2621,696
04/03/12	07:30-09:30	04/03/12	40618	7	20,8891	48187,4	2,5	0,0278895	43579,9	20,86388	8,71372	48398,5	7,5	0,0096466	45709,2	8,704609	-0,411209	11,07941	9,920536	9920,536
		05/03/12	40632	8,4	3,81982	279215	7,5	-0,804706	224548	4,466974	2,56033	187466	17	-0,733862	147045	3,135958	-7,137406	39,38261	4,340878	4340,878
		06/03/12	40645	9,8	3,17121	144830	7,5	-1,00771	131803	4,08828	2,68635	102497	17	-0,850314	106119	3,566712	-18,21432	81,96524	3,962005	3962,005
18/03/12	8:25-09:40	18/3/12	40822	9,5	7,3295	62439	7,5	-0,075591	65748,2	7,409097	4,60794	63050	17	-0,038432	70655	4,651008	-3,444413	33,01999	6,828447	6828,447
		19/3/12	40836	11,2	5,08013	230673	7,5	-0,399287	199049	5,424677	3,771135	180874	17	-0,0260203	166893	3,795144	-5,829891	39,12528	4,790017	4790,017
		20/3/12	40850	10,2	3,02563	309189	7,5	-0,1065	243823	3,109615	2,07452	211274	17	-0,0478696	36105,1	2,082701	-9,251017	36,2671	2,817755	2817,755
		21/3/12	40863	10,8	2,99966	302051	7,5	0,324798	296533	2,680796	2,16642	305255	17	0,23609	296760	1,9369	-12,77061	41,7354	2,42239	2422,39
01/04/12	2:41-03:35	01/04/12	41025	10,5	7,98165	162915	7,5	-0,143036	136834	8,101787	5,80968	143296	17	-0,0995438	127808	5,898465	-4,31167	42,43223	7,406001	7406,001
		02/04/12	41039	9	1,88529	343633	7,5	0,201972	321066	1,696582	1,64601	312233	17	0,148176	316277	1,495915	-47,34211	87,81976	1,664898	1664,898
12/04/12	4:32-15:10	13/04/12	41200	8,8	2,24142	806375	7,5	-0,99689	490771	2,848141	1,45184	800390	17	-0,171759	303796	1,517033	-7,13691	27,82693	2,665989	2665,989
24/04/12	01:35-02:15	24/04/12	41360	7,3	25,3633	176687	2,5	-3,1976	165744	28,36286	7,1154	158964	7,5	-1,24095	152075	8,302571	-0,249249	9,569405	9,104983	9104,983
		25/04/12	41374	11	4,20945	612513	7,5	-1,65396	271684	4,943074	3,13713	582297	17	-1,08583	274951	3,649841	-7,345928	43,81147	4,46662	4466,62
		26/04/12	41389	9	2,62302	237570	7,5	-0,212842	208002	2,809372	1,58444	207643	17	-0,126422	201208	1,706944	-8,617346	31,70933	2,635304	2635,304
		27/04/12	41403	10	1,70922	210612	7,5	0,448599	198952	1,285457	0,867992	112872	17	0,10987	107827	0,763033	-18,18447	30,87535	1,147977	1147,977

8.3 Plume track from the first day of the 11th paroxysms (August 20, 2011): AIRS and OMI overpass at 12:05 and 12:13 UT respectively showing how AIRS can help to see the cloud when OMI has an anomaly.

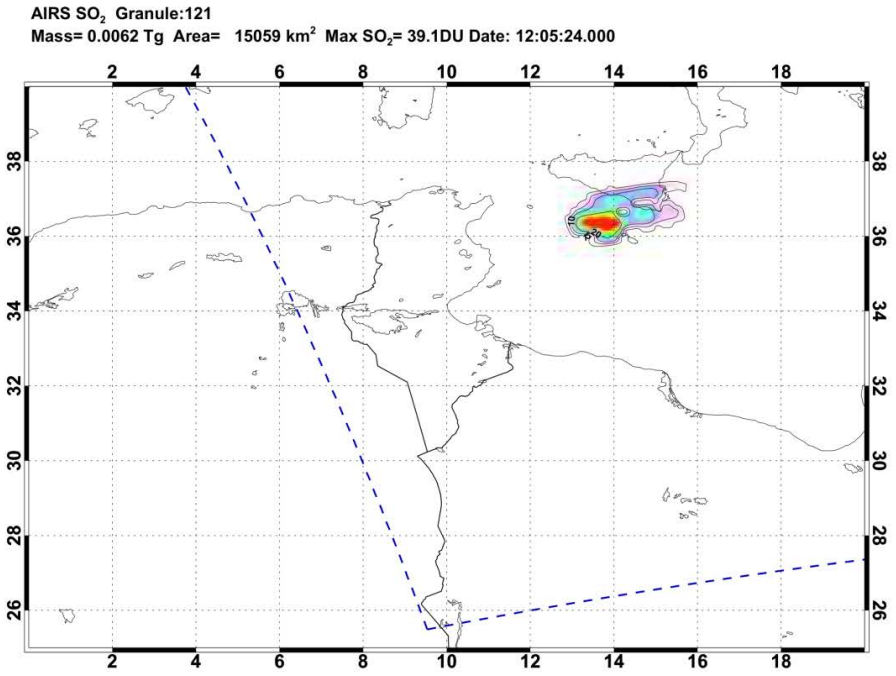

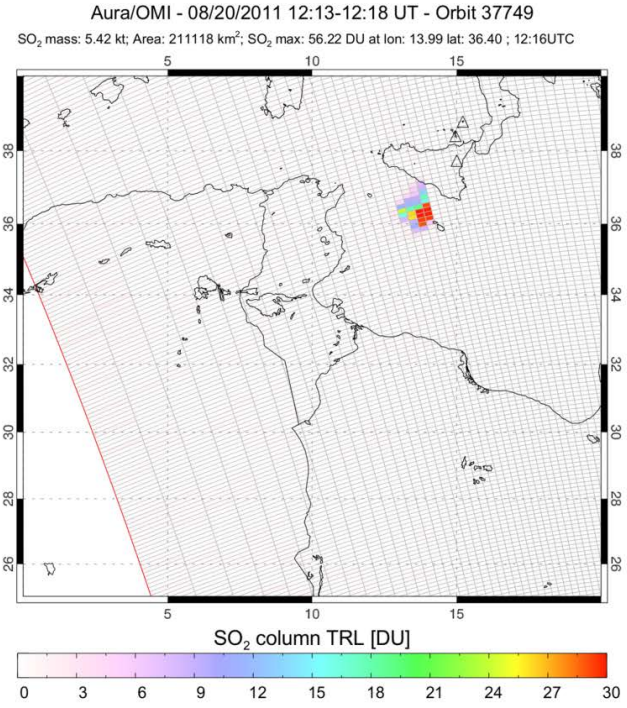

8.4 Plume track from the second day of the 11th paroxysms (August 21, 2011): AIRS and OMI overpass at 12:47 and 12:56 UT respectively showing how AIRS can help to see the cloud when OMI has an anomaly.

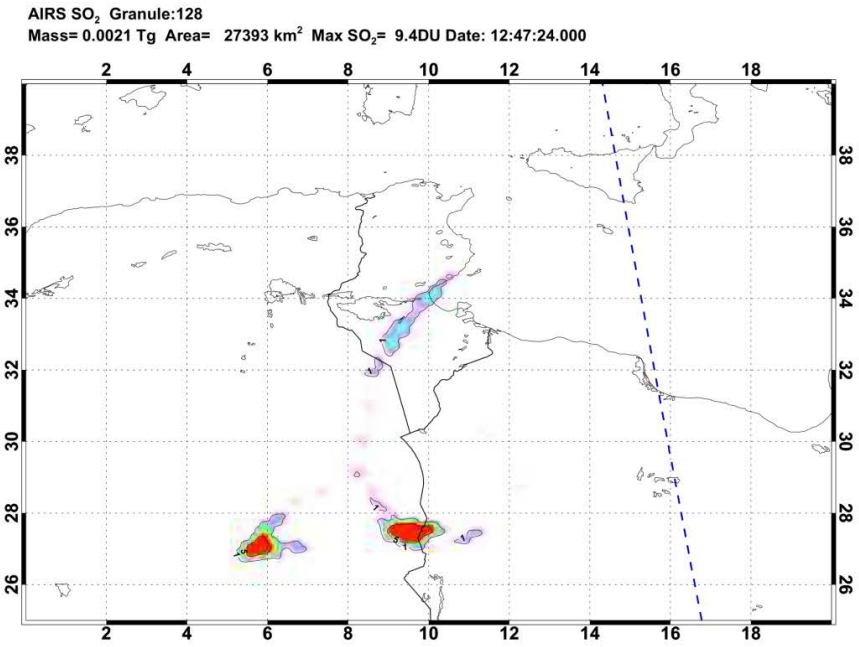

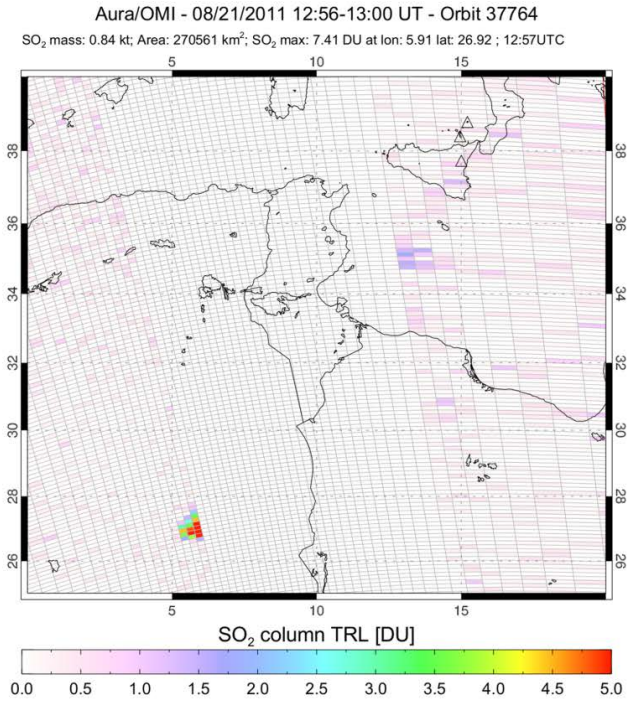

8.5 Plume track from September 8, 2011 (13th paroxysm): AIRS and OMI overpass at 12: 35 and 12: 45 UT respectively. OMI shows an anomaly that AIRS completes.

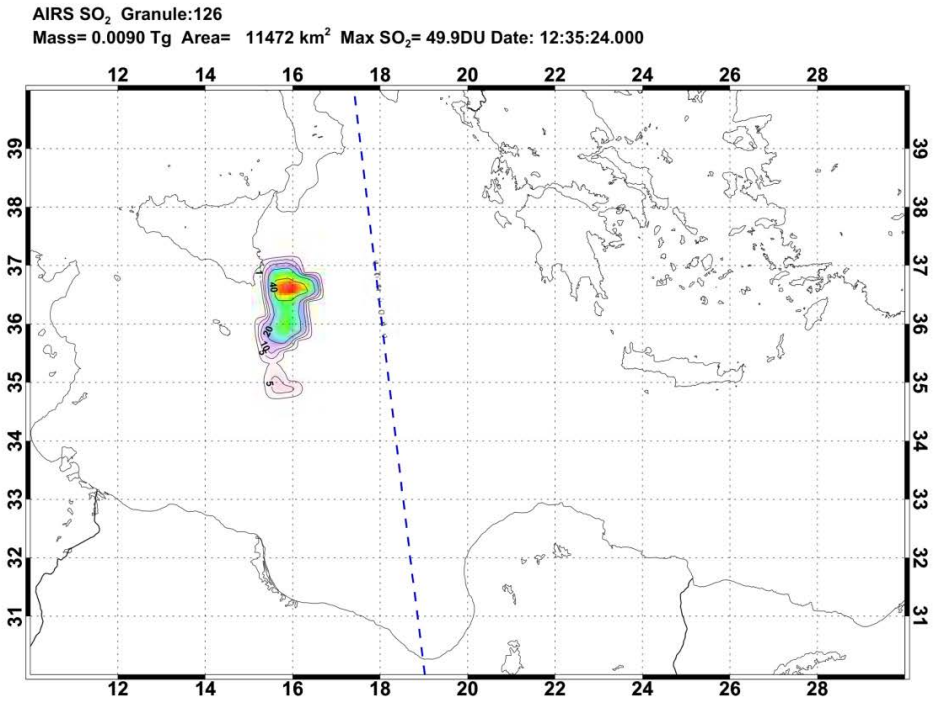

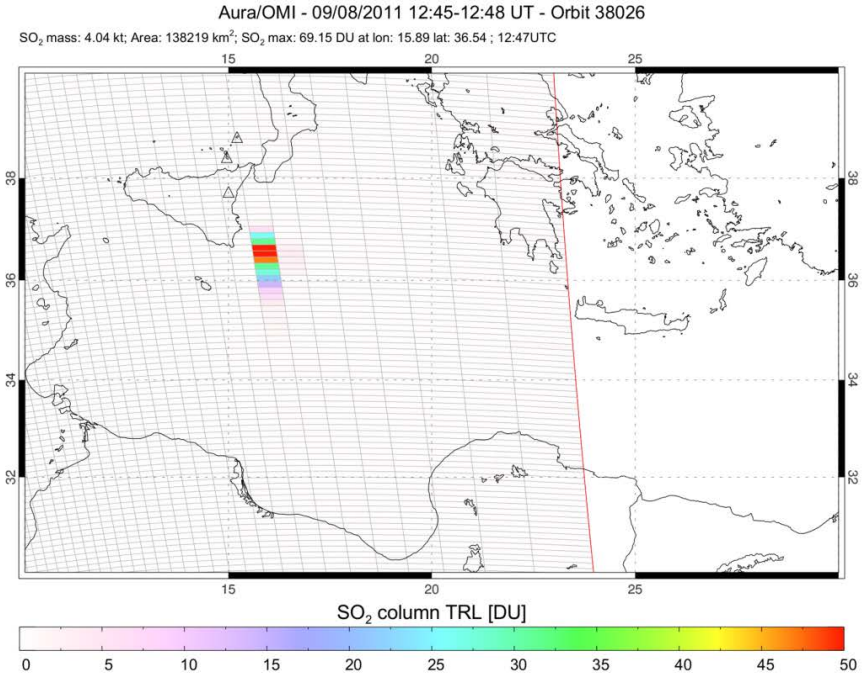

8.6 Plume track from September 9, 2011 (13th paroxysm): AIRS and OMI overpass at 11: 41 and 11: 49 UT respectively. OMI SO2 detection is more sensitive than AIRS.

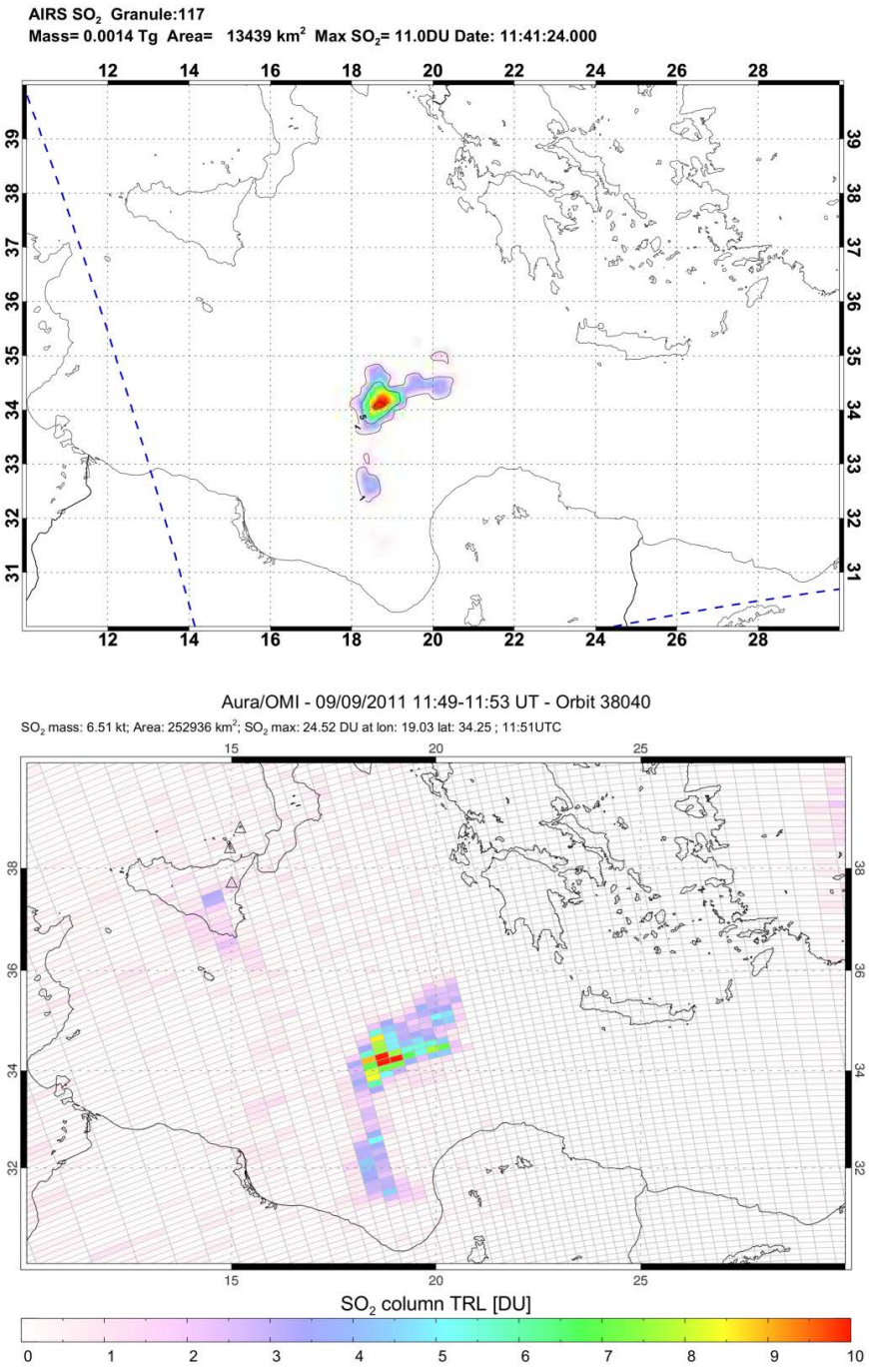

8.7 Radar mass calculation 1st paroxysm

11,2 mm 1/12/2011

			P3135			P3285					
		mean	mW	max	mW	mean	max		sum 2 gates		
jet	21:40-22:20	-107.9	1.62E-11	-96	2.55E-10	3.66E-12	7.87E-11				
Rayleigh	Nb part		8.66E+05		1.36E+07	1.96E+05	4.21E+06	Mtot jet mean	463.0		
	Vtot (m3)		0.637		10.0338	0.1442	3.0955	Mtot jet max	9.52E+03		
	Mtot (kg)		350.3751		5.52E+03	79.2997	1.70E+03				
	Concentration (kg/m3)		1.23E-05		1.93E-04	2.53E-06	5.43E-05				
								Masse panache lapilli (11,2mm)			
	22:30-23:40	-107.3	1.86E-11	-94	4.20E-10	4.33E-12	1.26E-10	MTOTAL mean	1.87E+05	Mass flux mean	1.56E+04
	Nb part		9.95E+05		2.25E+07	2.32E+05	6.74E+06	MTOTAL max	3.85E+06	max	3.21E+05
	Vtot		0.7319		16.522	0.1703	4.9581	405			
	Mtot		402.5673		9.09E+03	93.6626	2.73E+03	dt (s)	12		
	Concentration		1.41E-05		3.18E-04	2.99E-06	8.69E-05				
		P3135				P3285		P3435		P3585	
fontaine	22:20-22:30	-98	1.67E-10	-89	1.23E-09	6.32E-11	1.13E-09	4.80E-12	1.09E-10	2.09E-12	1.11E-11
Mie (0,1m)	Nb part		23		171	11	189	1	22	1	3
	Vtot		0.012		0.0895	0.0058	0.099	5.24E-04	0.0115	5.24E-04	0.0016
	Mtot		6.6235		49.2445	3.1678	54.4281	0.288	6.3355	0.288	0.8639
	Concentration (kg/m3)		2.32E-07		1.72E-06					Mtot mean	10.3673
										Mtot max	110.872
Vgate (m3)	3135	2.86E+07				dt	5.96733	Fountain			
	3285	3.14E+07					86.6667	MTOTAL mean	898.50	mass flux (kg/s)	150.57
								MTOTAL max	9608.91	max	1610.25

8.8 Copyright for Figure 3.4

Dear Ms. Estelle Bonny,

Thank you for placing your order through Copyright Clearance Center's RightsLink service. John Wiley and Sons has partnered with RightsLink to license its content. This notice is a confirmation that your order was successful.

Your order details and publisher terms and conditions are available by clicking the link below:
http://s100.copyright.com/CustomerAdmin/PLF.jsp?ref=c0a5273f-1666-48a6-9667-61228f65d507

Order Details
Licensee: Estelle Bonny
License Date: Jun 18, 2013
License Number: 3172070288205
Publication: Journal of Geophysical Research: Solid Earth
Title: Mass estimations of ejecta from Strombolian explosions by inversion of Doppler radar measurements
Type Of Use: Dissertation/Thesis
Total: 0.00 USD

To access your account, please visit https://myaccount.copyright.com.

Please note: Online payments are charged immediately after order confirmation; invoices are issued daily and are payable immediately upon receipt.

To ensure we are continuously improving our services, please take a moment to complete our customer satisfaction survey.

B.1:v4.2

8.9 Copyright for Figure 3.1

https://www.copyright.com/dispatcher?type=order&target=histdetid&id=11100878

Confirmation Number: 11100878
Order Date: 06/19/2013

Customer Information

Customer: Estelle Bonny
Account Number: 3000668272
Organization: Estelle Bonny
Email: estellebonny83@gmail.com
Phone: +1 (906)2314330

Order Details

IEEE transactions on geoscience and remote sensing : a publication of the IEEE Geoscience and Remote Sensing Society

Billing Status:

N/A

Order detail ID: 63784281
ISSN: 1558-0644
Publication Type: e-Journal
Volume:
Issue:
Start page:
Publisher: Institute of Electrical and Electronics Engineers
Author/Editor: Institute of Electrical and Electronics Engineers ; IEEE Geoscience and Remote Sensing Society

Permission Status: **Granted**

Permission type: Republish or display content

Type of use: Republish in a thesis/dissertation

Order License Id: 3172651250576